2012

Investigations into the degassing and eruption mechanisms of Nyamuragira volcano, Democratic Republic of the Congo (Africa)

Elisabet Marie Head
Michigan Technological University

INVESTIGATIONS INTO THE DEGASSING AND ERUPTION MECHANISMS OF NYAMURAGIRA VOLCANO, DEMOCRATIC REPUBLIC OF THE CONGO (AFRICA)

By

Elisabet Marie Head

A DISSERTATION

Submitted in partial fulfillment of the requirements for the degree of

DOCTOR OF PHILOSOPHY

(Geology)

MICHIGAN TECHNOLOGICAL UNIVERSITY

2012

This dissertation, "Investigations into the Degassing and Eruption Mechanisms of Nyamuragira Volcano, Democratic Republic of the Congo (Africa)," is hereby approved in partial fulfillment of the requirements for the Degree of DOCTOR OF PHILOSOPHY IN GEOLOGY.

Department of Geological and Mining Engineering and Sciences

Signatures:

Dissertation Advisor _____
Dr. Simon Carn

Department Chair _____
Dr. Wayne Pennington

Date _____

For my dad, Phillip D. Head, Jr.

TABLE OF CONTENTS

LIST OF FIGURES

LIST OF TABLES

PREFACE

Chapter 2, "Lava flow mapping of Nyamuragira volcano (1967-2011) using satellite data and automated methods," was authored by E.M. Head, A.L. Maclean, and S.A. Carn. My contributions to the paper were the analyses of all Landsat, Hyperion, and ALI images for Nyamuragira lava flow mapping, as well as the interpretation of our quantitative (e.g., statistical) and qualitative (e.g., lava flow boundaries) results.

Chapter 3, "Insight into volatile behavior at Nyamuragira volcano (D.R. Congo, Africa) through olivine-hosted melt inclusions," was authored by E.M. Head, A.M. Shaw, P.J. Wallace, K.W.W. Sims, and S.A. Carn. My contributions to the paper were the preparation and analyses of all melt inclusions in the study, as well as the interpretation of the results.

The contents of Chapter 4, written solely by E.M. Head, have not been submitted for publication prior to the submission of this dissertation.

ACKNOWLEDGEMENTS

Without generous funding from numerous sources, this work would not have been possible. I would like to thank the National Science Foundation (grant EAR 0910795 to Simon Carn) for funding the majority of my research; the Michigan Technological University Geological and Mining Engineering and Sciences (GMES) Department for providing travel funds for countless conferences and workshops, as well as teaching assistant opportunities; the Michigan Technological University Earth, Planetary, and Space Sciences Institute (EPSSI) and the Michigan Technological University Graduate Student Government (GSG) for contributing travel funds to several conferences and workshops; and the Michigan Space Grant Consortium and the Michigan Technological University Seaman Mineral Fellowship for partially supporting my remote sensing and petrology research.

I am deeply thankful for the invaluable guidance I received from many mentors throughout my graduate studies, both at Michigan Technological University and beyond. From Michigan Technological University, I would like to thank my PhD advisor, Simon Carn, as well as my former PhD advisor, Gregg Bluth, for their patience, kindness, and sound advice. My committee members, Ann Maclean, Alison Shaw (Woods Hole Oceanographic Institution), William Rose, and Gregory Waite were always willing to provide counsel and encouragement. The help of Kelly McLean and Amie Ledgerwood with logistics and departmental advice was crucial for the success of my work. I greatly appreciate the countless helpful discussions with Jeremy Shannon, Mari Dalton, Alex Guth, Rudi Escobar, John Lyons, Miriam Rios, Kari Anderson, Erika Vye, and Mark Klawiter.

At the University of Oregon, I would like to thank Paul Wallace for taking me under his wing and providing guidance in petrology. Many thanks to John Donovan, Dana Johnston, and Kathy Cashman for assistance with analyses and experiments, and for insightful discussions regarding petrology and physical volcanology. Shari Douglas helped with departmental logistics and made my stay at the University of Oregon comfortable.

At Woods Hole Oceanographic Institution, I would like to extend my gratitude to Ken Sims for his kind guidance and advice. I would also like to thank Nobu Shimizu and Andrey Gurenko for assistance during long-hours of EMPA and SIMS analyses. At Massachusetts Institute of Technology, I would like to thank Nilanjan Chatterjee for his help with EMPA work.

I cannot express enough the thankfulness I have for my family and friends. Their love, kindness, generosity, and sense of humor allowed me to ride the ups and downs of PhD life with confidence and sanity. I am especially grateful that my dad was here to see me follow my passion for volcanology and complete this degree. My family's support has been profound and always reminds me that a healthy balance between work, family, and friends is the best formula for happiness and success.

ABSTRACT

One of two active volcanoes in the western branch of the East African Rift, Nyamuragira (*1.408ºS, 29.20ºE; 3058 m*) is located in the D.R. Congo. Nyamuragira emits large amounts of SO_2 (up to ~1 Mt/day) and erupts low-silica, alkalic lavas, which achieve flow rates of up to ~20 km/hr. The source of the large SO_2 emissions and pre-eruptive magma conditions were unknown prior to this study, and 1994-2010 lava volumes were only recently mapped via satellite imagery, mainly due to the region's political instability. In this study, new olivine-hosted melt inclusion volatile (H_2O, CO_2, S, Cl, F) and major element data from five historic Nyamuragira eruptions (1912, 1938, 1948, 1986, 2006) are presented. Melt compositions derived from the 1986 and 2006 tephra samples best represent pre-eruptive volatile compositions because these samples contain naturally glassy inclusions that underwent less post-entrapment modification than crystallized inclusions. The total amount of SO_2 released from the 1986 (0.04 Mt) and 2006 (0.06 Mt) eruptions are derived using the petrologic method, whereby S contents in melt inclusions are scaled to erupted lava volumes. These amounts are significantly less than satellite-based SO_2 emissions for the same eruptions (1986 = ~1 Mt; 2006 = ~2 Mt). Potential explanations for this observation are: 1) accumulation of a vapor phase within the magmatic system that is only released during eruptions, and/or 2) syn-eruptive gas release from unerupted magma. Post-1994 Nyamuragira lava volumes were not available at the beginning of this study. These flows (along with others since 1967) are mapped with Landsat MSS, TM, and ETM+, Hyperion, and ALI satellite data and combined with published flow thicknesses to derive volumes. Satellite remote sensing data was also used to evaluate Nyamuragira SO_2 emissions. These results show that the most recent Nyamuragira eruptions injected SO_2 into the atmosphere between 15 km (2006 eruption) and 5 km (2010 eruption). This suggests that past effusive basaltic eruptions (e.g., Laki 1783) are capable of similar plume heights that reached the upper troposphere or tropopause, allowing SO_2 and resultant aerosols to remain longer in the atmosphere, travel farther around the globe, and affect global climates.

CHAPTER 1: INTRODUCTION

1.1 The East African Rift

The East African Rift system (EARS) is a distinct feature of the African continent (Figure 1.1). It spans the Afar region, into Kenya, and splits around the robust Tanzanian craton into two branches: the Eastern Branch, which can be further broken up into the Main Ethiopian and Kenyan Rifts and the Western Branch, which extends through Uganda and the Democratic Republic of Congo (D.R. Congo) to Malawi (Kampunzu and Mohr, 1991; Furman, 2007). Within the Eastern Branch there are two areas of uplift, the Ethiopian and Kenyan Domes, separated by the Turkana Depression (Furman, 2007). Based on geochemical and geophysical evidence, the two domes are shown to be manifestations of the South African Superplume, which is considered the source of EARS volcanism (Nyblade and Robinson, 1994; Ebinger and Sleep, 1998; Nyblade *et al.*, 2000; Weeraratne *et al.*, 2003). This plume may be homogeneous (Ebinger and Sleep, 1998) or complexly heterogeneous (Furman *et al.*, 2004), or there may even be two separate plumes with different geochemistries (George *et al.*, 1998; Rogers *et al.*, 2000). While the plume(s) rises, it interacts with the sub-lithosphere and the resultant melts may also interact with the crust. Studies of major and trace elements and isotopes of a wide variety of volcanic products extruded from the entire rift have shown that the mantle composition beneath the EARS is heterogeneous with a resolution as small as <1 km (Furman and Graham, 1999; Furman, 2007). This heterogeneity is caused by several stages of ancient mantle metasomatism as evidenced by the geochemistry of mantle xenoliths and silica-undersaturated lavas, which are thought to represent melts from the sub-lithospheric mantle due to either a hot plume rising or continental rifting (Furman and Graham, 1999).

1.2 The Eastern Branch

Based on $^{40}Ar/^{39}Ar$ dating, volcanism began 43 Ma in the Turkana Depression of southern Ethiopia and propagated south to Kenya and north to Yemen between 33-30 Ma (Ebinger

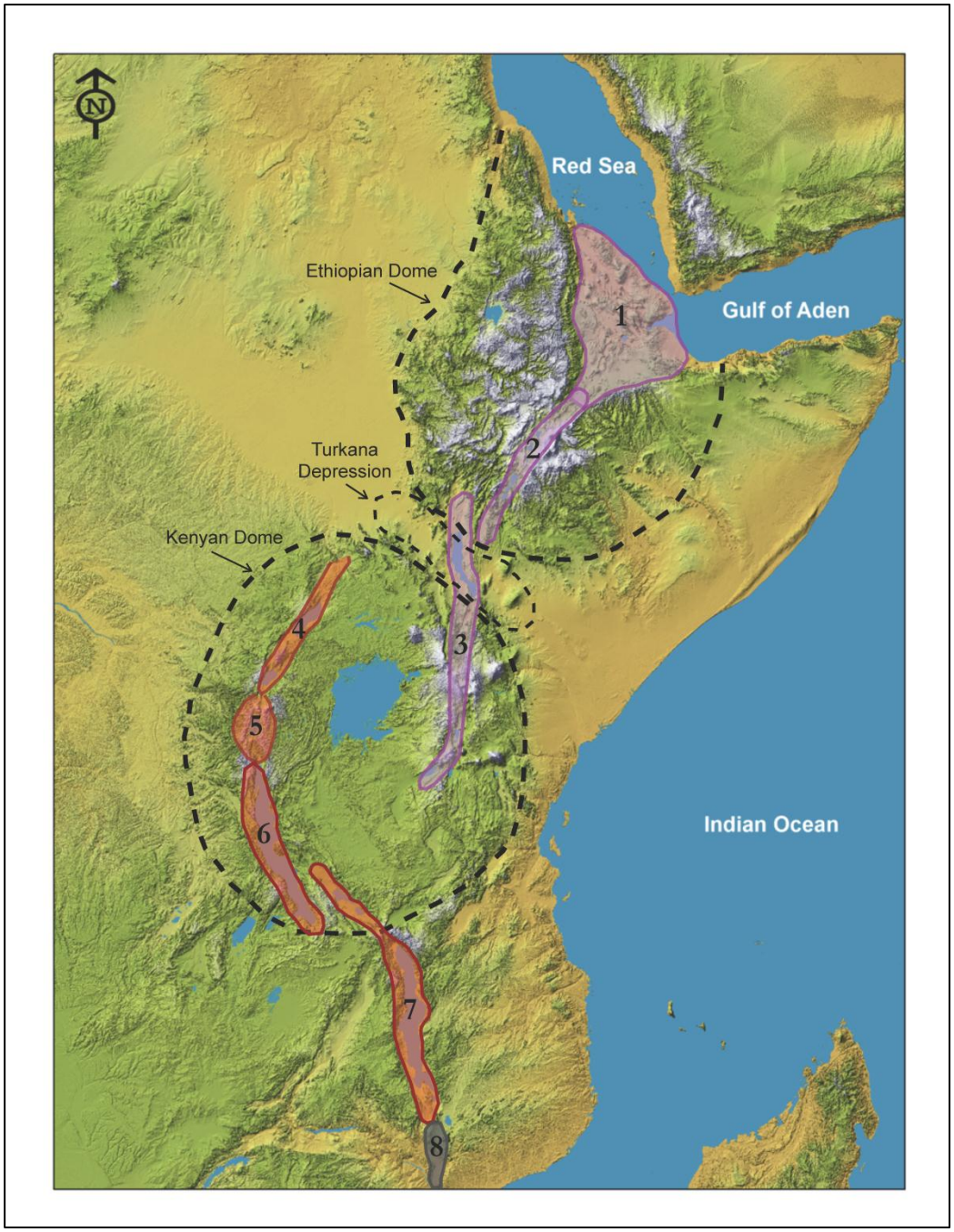

Figure 1.1 An SRTM base map of eastern Africa (http://photojournal.jpl.nasa.gov/tiff/PIA04965.tif) displays the topographic features that define the East African Rift. The eastern (purple) and western (red) branches are color coded separately. Lake Victoria sits almost in the middle of the robust Tanzanian craton where the two branches split. Currently, researchers are investigating the southern-most section of the rift (grey area- labeled 8) to determine if and how fast the rift is propagating there.

and Furman, 2002). Eruptive products in this first stage of rifting consisted mostly of fissure-fed flood basalts, which were interwoven with eruptions of rhyolite. In the south and west, flood basalts transitioned to nephelinites, basanites, and phonolites 25-19 Ma (Kampunzu and Mohr, 1991). Afar (1 in Figure 1.1) is at the northern-most position of the Main Ethiopian Rift and volcanism there began ~30 Ma. At this point in time, Africa and the Arabian peninsula were still connected. The Afar marks the intersection of a triple junction between the EARS, the Red Sea (~28 Ma), and the Gulf of Aden (~35 Ma), a result of the Afro-Arabian shield breakup (Wolfenden *et al.*, 2004). Only at 11 Ma was it clear that the current location of Afar was the focal point from which the Red Sea, Gulf of Aden, and East African Rifts progress (Watchorn *et al.*, 1998; Wolfenden *et al.*, 2004). Renewed activity in the Afar 13 Ma produced large quantities of flood basalt. Magmatism in this region changed style 1 Ma to axial ranges analogous to lines of seafloor spreading, although the composition of the erupted lavas are transitional instead of the oceanic tholeiites found in the Red Sea and Gulf of Aden (Kampunzu and Mohr, 1991).

In both the Main Ethiopian Rift and the northern Kenya Rift (1-2 and 3, respectively, in Figure 1.1) basalts are mainly transitional-tholeiitic in composition with trachyte and rhyolite (Ethiopian Rift only) derivatives (Furman, 2007). The on-axis volcanoes within the central and southern Kenyan Rift produce little transitional-tholeiitic basalt and have erupted more trachytic to pantelleritic compositions. Products from the off-rift volcanic field, Chyulu Hills, are silica-undersaturated (Furman, 2007). Crustal thicknesses are ~170-200 km beneath the uplifted domes, ~ 60 km in the Afar, and ~35 km beneath the Kivu area of the Western Branch (Nolet and Mueller, 1982; Nyblade *et al.*, 2002).

1.3 The Western Branch

The Western Branch (4-7 in Figure 1.1) is an arcuate structure of en echelon rift-related depressions in which most of the western volcanic provinces are found. From north to south, Lakes Albert, Edward, Kivu, Tanganyika, Rukwa, and Malawi also occupy the troughs and define the rift. A smaller volume of volcanic material has been erupted from

the Western Branch compared to the Eastern Branch and compositions tend to be more potassic, although a variety of lava compositions have been erupted from the former (Pouclet, 1975; Katabarwa, 1983; Lloyd *et al.*, 1991; Kampunzu and Mohr, 1991; Demant *et al.*, 1994; Kampunzu *et al.*, 1998; Furman and Graham, 1999; Furman *et al.*, 2004; Furman, 2007). The Western Branch also exhibits a lower degree of extension (<15%; Ebinger, 1989) than the Eastern Branch. Sr-Nd isotope data indicate melting of the thick continental lithosphere beneath, particularly, the Virunga, Toro-Ankole, and Rungwe provinces (Furman, 1995; Rogers *et al.*, 1998). Additional isotopic data suggest that the source of the ultrapotassic volcanics of the Western Branch is a phlogopite-bearing lherzolite, at depths between 90-100 km (Chakrabarti *et al.*, 2009a) and productivity in the Virunga in particular has been greatest the past 100 ky (Rogers *et al.*, 1998).

The first rift-related activity in the Western Branch began 16-13 Ma with the development of a rift basin in the northern-most volcanic province, Toro-Ankole (Kampunzu *et al.*, 1998). However, volcanism did not occur in the Toro-Ankole region until the Upper Pleistocene to Recent times. Eruptive products from this area are unique for the fact that, unlike most other provinces in the EAR, no tholeiitic lavas were extruded. Instead, strongly alkaline, silica-undersaturated products such as olivine melilitites, feldspar free and olivine-perovskite bearing basanites, clinopyroxene-kalsilite-olivine rich lavas, and extrusive carbonatites were erupted. These compositions indicate a highly metasomatised mantle which cannot produce tholeiitic melts by partial melting (Kampunzu *et al.*, 1998).

The first volcanic activity in the Western Branch began 11 Ma in the Virunga province, south of Toro-Ankole (Kampunzu *et al.*, 1998). The initial burst of volcanism produced fissure-fed tholeiites, which were then overlain by sodium (Na) alkaline lavas including basanites, hawaiites, mugearites, and benmoreites. The last of the Na alkaline lavas erupted 9 Ma. Although volcanism occurred 11 Ma, the tholeiitic products were technically pre-rift, while the latest erupted alkaline compositions marked the actual rift stage. A quiescent period from 9-<3 Ma in the Virunga was followed by Pliocene-Pleistocene volcanic activity from eight major volcanic centers: Muhavura, Gahinga, Sabinyo, Visoke,

Mikeno, Karisimbi, Nyiragongo, and Nyamuragira (Figure 3.1). All eruptive products were potassic, but the most silica-undersaturated compositions (nephelinites, melilitites, and leucitites) came from Nyiragongo and Visoke and resembled the Toro-Ankole compositions (Kampunzu *et al.*, 1998). The less silica-undersaturated compositions, erupted from the other centers, were potassic basanites, hawaiites, mugearites, benmorite, and trachytes. Presently, the only active volcanoes in the Western Branch are Nyiragongo and Nyamuragira.

Further south in the Bukavu and Mwenga-Kamituga provinces, a similar pattern to initial Virunga volcanism occurred: tholeiitic flood basalts transitioning to Na alkaline lavas. In the Bukavu, the transition occurred between 8-6 Ma, while volcanism began in Mwenga-Kamituga around 6 Ma. Following the Na alkaline lavas, transitional lavas erupted.

1.4 Gaps in Our Knowledge of Nyamuragira Volcanic Activity

Petrology

Focusing on Nyamuragira volcano, many studies have been carried out to characterize its magma (lava) through geochemistry, petrography, and mineralogy data, as well as to unravel the evolution history and source of these magmas (Holmes and Harwood, 1937; Denaeyer, 1965, 1972; Bell and Powell, 1969; Vollmer and Norry, 1983; Aoki and Kurasawa, 1984; Fujimaki *et al.*, 1984, Aoki *et al.*, 1985; Hayashi *et al.*, 1992). The most recent of these studies focused on lava and tephra samples from Nyamuragira eruptions in 1976, 1971, 1976-77, 1980, and 1981-82 (Aoki *et al.*, 1985) and 1976, 1980, 1981-82, 1984, 1986, 1987-88, and 1989 (Hayashi *et al.*, 1992). The former was an in-depth geochemical, petrographical, and mineralogical study that characterized Nyamuragira extrusives as a high-K suite of olivine basanite-tephritic phonolite. Aoki *et al.* (1985) suggest a metasomatized source for Nyamuragira magma and they found that variations in Nyamuragira chemistry can be explained by fractional crystallization of olivine, followed by clinopyroxene with plagioclase and titanomagnetite. Hayashi *et al.* (1992), on the other hand, posit that Nyamuragira magmas (1976-1989) erupted from a reversely zoned magma

chamber. They suggest that, because the 1989 magma had a more felsic composition and previously erupted magmas were increasingly more primitive, the former were erupted from a more evolved upper part of the magma chamber. The next publication regarding Nyamuragira geochemistry was not produced until 2009. Chakrabarti *et al.* (2009a) evaluated the source of Nyamuragira magma using isotope data (Nd-Sr-Pb and ^{238}U-^{230}Th-^{226}Ra-^{120}Pb) and found that Nyamuragira magma was generated from partial melting of a metasomatised mantle (carbonate-rich, high-F phlogopite with residual garnet). However, Nyamuragira's magmatic source is less carbonated and appears to be the result of higher degrees of partial melting from a shallower source than its neighboring volcano, Nyiragongo (~15 km to the east), which suggests that the degree of metasomatism beneath these volcanoes can vary greatly within a small area. Aside from these studies, geochemical work on Nyamuragira eruptive products from recent eruptions (1990-present) is lacking. In addition, prior to our study, there were no published data regarding the pre-eruptive magma volatile content of Nyamuragira volcano and, in fact, only one American Geophysical Union abstract exists (Waters *et al.*, 2004), reporting the pre-eruptive volatile content of melt inclusions from the Turkana region. Our contribution to EARS knowledge, therefore, includes the first detailed description of magma volatile contents from Nyamuragira volcano in the Western Branch and, to some degree, of the entire East African Rift.

Lava Flow Mapping

For several decades, the only compiled map of Nyamuragira lava flows was one produced by Thonnard *et al.* (1965), which detailed Nyamuragira lava flows erupted until 1958. Due to the dangerous civil conditions in the D.R. Congo, field studies have been hampered since 1994 and satellite imagery has become a crucial tool for monitoring and evaluating Nyamuragira volcanic activity. At the beginning of this PhD research, no updated map existed for Nyamuragira and, therefore, one of my goals was to map the lava flows and derive lava volumes for each flow. An abstract on this was produced in 2007 for the ECGS Workshop, "Active Volcanism and Continental Rifting with special focus on the

Virunga (North Kivu, DRC)," in Luxembourg, November 19-21. Although several publications regarding individual Nyamuragira lava flows have been produced since 1958 (a detailed synopsis of these studies can be found in Chapter 2), no full flow field map (1938-2010) was published until Smets *et al.* (2010). The most recent mapping efforts utilized either radar imagery alone (Colclough 2005) or a combination of radar and optical satellite data (Smets *et al.* 2010). However, both studies stress that radar could not be used alone and optical imagery was necessary to delineate the lava flow boundaries. Smets *et al.* (2010) digitized each lava flow with optical satellite imagery and radar data, although we offer an alternative way to map these flows, in some cases greatly reducing the time it would take to digitize the entire flow. Therefore, we provide a map of 1967-2011 Nyamuragira lava flows, created with automated classification methods and occasional digitization and provide a comparison of our results with the most recent publications.

Volcanic Emissions

Ground-based gas studies have been conducted in the Kenyan Rift at Oldoinyo Lengai (Fischer *et al.*, 2009) and in the Western Rift at Nyamuragira (Verhoogen *et al.*, 1939) and Nyiragongo (Tedesco *et al.*, 2007; Sawyer *et al.*, 2008). However, since Verhoogen *et al.* (1939), ground-based gas data for Nyamuragira are absent in the literature. The long-term adverse political situation in eastern D.R. Congo may partly be responsible for this lack of data. Only since the launch of satellite platforms capable of quantifying volcanic gases (see Chapter 4) has gas data collection continued for Nyamuragira. These data offer a safe and synoptic view of dangerous and remote locations. Satellite-based gas measurements for EARS volcanoes have been reported on the Smithsonian's Global Volcanism web site (Smithsonian Institution, 1971-2011), but few have been published in journals. Sulfur dioxide (SO_2) emissions from Nyamuragira (1980-2004) were quantified and tracked in detail by Carn and Bluth (2003) and Bluth and Carn (2008). Here, we focus on the most recent eruptions of Nyamuragira (2006 and 2010) and not only quantify these SO_2 emissions, but we also attempt to determine the altitudes of these volcanic emissions to better constrain Nyamuragira's output and atmospheric impact.

The main goal of this dissertation is to investigate the large SO_2 emissions emitted from Nyamuragira. I addressed this goal by 1) estimating erupted lava volumes through lava flow mapping (Chapter 2; Figure 1.2); 2) determining the volatile content of Nyamuragira magmas through olivine-hosted melt inclusions (Chapter 3; Figure 1.2); and 3) quantifying the SO_2 emissions from the latest Nyamuragira eruptions (2006 and 2010; Chapter 4; Figure 1.2). The research presented in Chapter 3 and Chapter 4 also contributes to the broad knowledge of basaltic and alkalic effusive volcanic eruptions. In the past, researchers have relied on estimates from melt inclusions to determine the volcanic gas (particularly SO_2) yields to the atmosphere (e.g., Grimsvotn and Katla; Thordarson *et al.*, 2003). Accurate SO_2 emissions estimates are important to further understanding of past health and climatological connections with large effusive eruptions. However, if degassing in the magma reservoir prior to inclusion entrapment occurs, these SO_2 emissions estimates based on melt inclusion data could be severely underestimating the SO_2 release. Chapter 3 investigates whether melt inclusions from the effusive alkalic system of Nyamuragira are accurately representing SO_2 release. These results could shed light on more evolved alkalic compositions erupted from historical effusive eruptions, such as Laki 1783 (Stothers *et al.*, 1986). In addition to SO_2 abundance, the maximum height volcanic gases can be injected into the atmosphere was poorly known for effusive basaltic eruptions (Stothers *et al.*, 1986). In Chapter 4, cloud heights from the effusive Nyamuragira eruptions are investigated to address this issue.

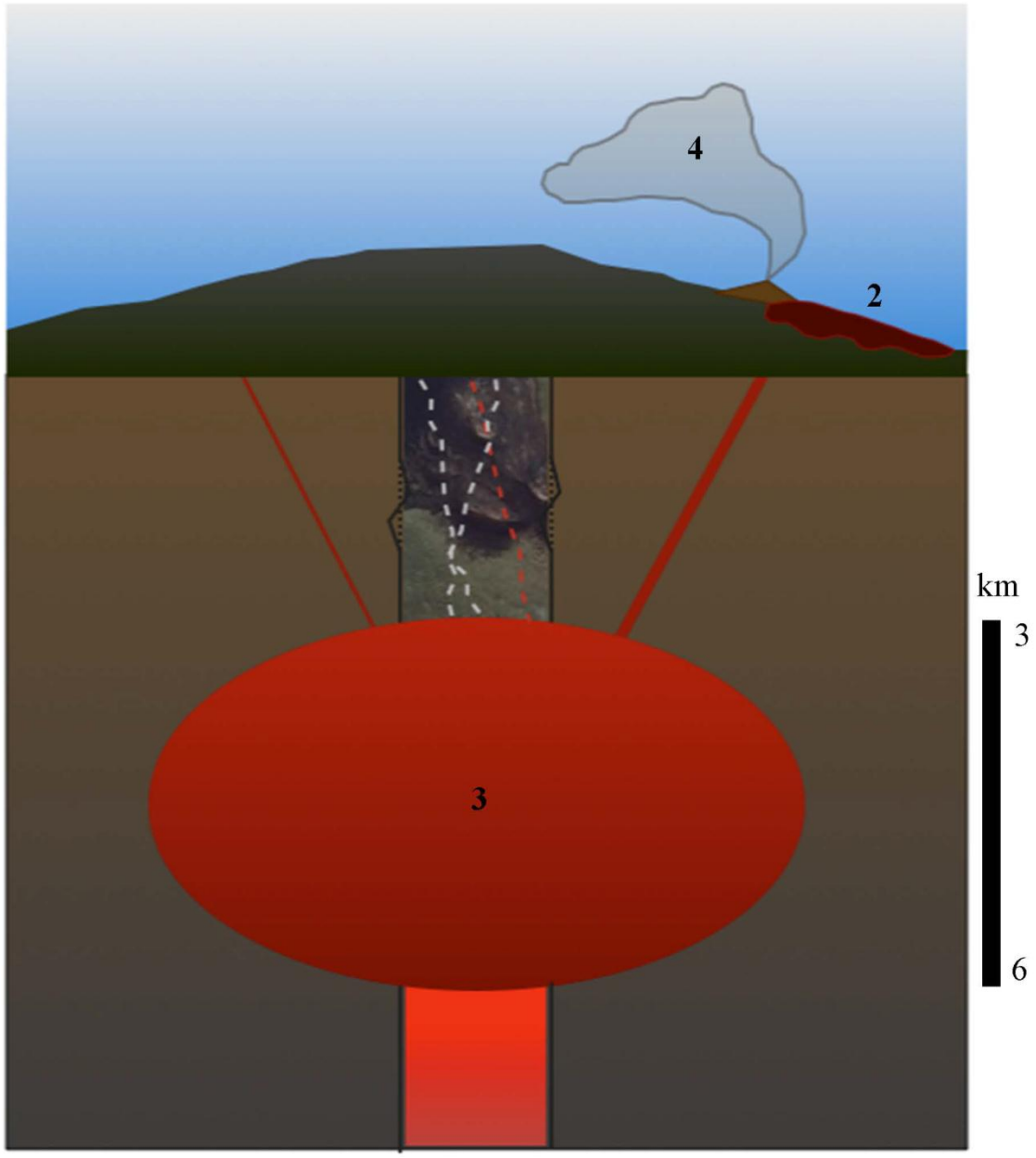

Figure 1.2 This schematic diagram (not drawn to scale) illustrates the three areas of research addressed in this dissertation. Chapter 2=Lava flow mapping and volume estimates; Chapter 3= Nyamuragira magma volatile abundance and evolution; and Chapter 4=SO_2 emissions. Magma volatile abundance and evolution has not been evaluated until this work. Lava flow mapping/volume estimates and SO_2 quantification/tracking are updated through the research presented in this dissertation.

CHAPTER 2: MAPPING LAVA FLOWS FROM NYAMURAGIRA VOLCANO (1967-2011) USING SATELLITE DATA AND AUTOMATED METHODS[1]

ABSTRACT

The volume, location, and extent of historical lava flows are important when assessing volcanic hazards, as well as the productivity or longevity of a volcanic system. We use a Landsat/Hyperion/ALI dataset and automated classification methods to map lava flows at Nyamuragira volcano (1967-2011) in the Democratic Republic of the Congo. The humid tropical climate of Nyamuragira is advantageous because its lava flows are emplaced onto heavily forested flanks, resulting in strong contrast between lava and vegetation, which contributes to efficient flow mapping. With increasing age, there is an increase in Landsat band-4 reflectance, suggesting lava flow revegetation with time. This results in a distinct spectral contrast to delineate overlapping flows emplaced ~5 years apart. Areal extents of the flows are combined with published lava flow thicknesses to derive volumes. The Landsat/Hyperion/ALI dataset is advantageous for mapping future flows quickly and inexpensively, particularly for volcano observatories where resources are limited.

2.1 Introduction

2.1.1 Lava flow mapping

Mapping lava flows from volcanic eruptions serves many purposes, such as the determination of vent locations, the areal extents of flows (widths and lengths), and flow volumes. Knowledge of the geographical position and direction of flows is used in hazard

[1] This is an unformatted version of an article in press with *Geomatics, Natural Hazards and Risk*, doi:10.1080/19475705.2012.680503. *Geomatics, Natural Hazards and Risk* is available online at: www.tandfonline.com.

prediction (Trusdell 1995). Lava volumes can be estimated through either a combination of lava flow area with field-based lava flow thickness measurements (Shaw and Swanson 1970; Self *et al.,* 1997; Crown and Baloga 1999) or subtraction of pre- and post-eruptive digital elevation models (DEMs) (Rowland *et al.,* 2003; Lu *et al.,* 2004). These volumes can be used in magma supply models and time-series analyses of volcanic activity to further the understanding of eruption mechanisms (Burt *et al.,* 1994). At volcanoes situated in remote or politically unstable locations where ground-based monitoring and fieldwork are hazardous or impossible, airborne and spaceborne remote sensing techniques are particularly useful (Abrams *et al.,* 1991; Harris *et al.,* 1999; Carn *et al.,* 2003; Carn and Oppenheimer 2000; Patrick *et al.,* 2003). For Nyamuragira volcano in the Democratic Republic of the Congo (D.R. Congo) this is certainly the case. Not only is Nyamuragira's lava flow field remote, it is also extensive (Figure 2.1), and persistent insecurity in the region continues to preclude detailed field surveys of the entire flow field. Therefore, remote sensing has proven to be a crucial tool to investigate Nyamuragira's eruptive behavior (Carn and Bluth 2003; Colclough 2005; Bluth and Carn 2008; Smets *et al.,* 2010).

2.1.2 Volcanic activity at Nyamuragira

The western branch of the East African Rift can be divided into four volcanic provinces from north to south: 1) Toro-Ankole in western Uganda, 2) Virunga and 3) Kivu spanning the D.R. Congo, Rwanda, Burundi, and southern Uganda, and 4) the Rungwe in southern Tanzania (Kampunzu *et al.,* 1998; Ebinger and Furman 2002). Nyamuragira (also known as Nyamulagira; 1.41°S, 29.20°E) and its neighboring volcano, Nyiragongo, are part of the Virunga volcanic chain and are the only active volcanoes in the western branch (Figure 2.1). The currently inactive Virunga volcanoes are Muhavara, Sabinyo, Visoke, Mikeno, and Karisimbi.

Nyamuragira erupted sixteen times between 1980 and 2011, making it one of the world's most active and productive volcanoes (Smithsonian, Institution, monthly reports, 1971-2011, http://www.volcano.si.edu/world/volcano.cfm?vnum=0203-02=&vol page=var,

hereinafter referred to as Smithsonian Institution, monthly reports, 1971-2011 (e.g., Smithsonian Institution 1971-2011)). A shield volcano with a near-circular summit caldera measuring 2 x 2.3 km at an elevation of ~3 km, Nyamuragira produces low-silica, high alkali lava compositions (SiO_2 ranging from 43-56 wt%; $NaO + K_2O$ up to 7 wt%), which have reached flow rates of up to ~20 km/hr (Aoki *et al.,* 1985; Hayashi *et al.,* 1992; Smithsonian Institution 1971-2011). Based on reports from the Smithsonian's Global Volcanism Network (GVN; Smithsonian Institution 1971-2011), most of Nyamuragira's eruptive history has consisted of summit (intra-caldera) and effusive flank eruptions. Nyamuragira eruptions typically begin with ~200 m high fire fountains and contemporaneous lava flows. Tephra fall is commonly reported during Nyamuragira eruptions, and ash from several eruptions has been associated with destruction of crops and health problems in the surrounding area (Smithsonian Institution 1971-2011).

2.1.3 History of Nyamuragira lava flow mapping

Thonnard *et al.,* (1965) produced a map showing Nyamuragira lava flows erupted until 1958. Kasahara *et al.,* (1991) compiled published volumes from several sources for individual eruptions between 1900-1991, although no lava flow map was created. Since 1994, political unrest in the D.R. Congo has prohibited not only ground-based mapping efforts, but also most ground-based volcano monitoring of Nyamuragira (e.g., volcanic gas measurements, leveling surveys) from the Goma Volcano Observatory. Therefore, satellite observations have been essential for post-1994 studies of volcanic activity in the Virunga. Satellite-based radar mapping efforts were carried out for individual flows and cones from Nyamuragira (Mackay and Mouginis-Mark 1997; Colclough 2005), Nyiragongo (Mackay and Mouginis-Mark 1997; Colclough 2005), and Karisimbi (Mackay and Mouginis-Mark 1997). A more recent study by Smets *et al.,* (2010) utilized radar data and optical imagery, and the Thonnard *et al.,* (1965) map, to manually trace lava flow boundaries and map Nyamuragira lava flows erupted between 1938 and 2010. Herein, we apply automated classification methods to Landsat data, with the addition of Hyperion and ALI data when cloud-free Landsat scenes were unavailable, to map lava flows erupted from Nyamuragira

between 1967 and 2011. We describe the image processing techniques used to delineate the lava flows, and compare our results with prior Nyamuragira mapping efforts (Colclough 2005; Smets *et al.,* 2010).

As cloud cover can hinder satellite-based lava flow mapping using optical datasets, it is best to utilize satellite data from a variety of sources, collected on a range of days. Combining high spatial resolution aerial photography with medium-to-high spatial resolution optical, thermal (temperature), and radar (textural) satellite data would be optimal, as it would allow a more complete characterization of the lava flows, although high spatial resolution data can be prohibitively expensive for resource-limited volcano observatories. For our mapping efforts, we assessed the use of aerial photographs, which have been used in the past to aid lava flow mapping (Ray 1960; Abrams *et al.,* 1996; Legeley-Pandovani *et al.,* 1997). However, historical photography has been poorly preserved for Nyamuragira. Aerial photography of the Nyamuragira lava flow field with little or no metadata only exists up to the 1950's (B. Smets pers. comm.), while new orthographic aerial photography is difficult to obtain due to the current political climate. In contrast, remotely sensed satellite imagery is readily available.

Since radar can penetrate cloud cover, it is a useful tool in tropical regions such as Nyamuragira where cloud cover is significant (e.g., Carn 1999). Satellite-based radar imagery has been used to map Nyamuragira's lava flows (Colclough 2005; Smets *et al.,* 2010), although Colclough (2005), who attempted mapping of the 1998 and 2001 Nyamuragira flows, points out that radar prohibited the mapping of all downslope flow sections. Colclough (2005) used eleven ERS 1/ERS 2 Synthetic Aperture Radar (SAR) images acquired between 1997 and 2003, and compared the backscattered energy between SAR pairs to assess changes over time, such as the emplacement of new lava flows. The 1998 and 2001 flows were emplaced on top of older flows downslope, all of which produced a similar backscattering signal in the 5.66 cm (C-band) wavelength, preventing the separation (delineation of boundaries) between the fresh and older flows. Colclough

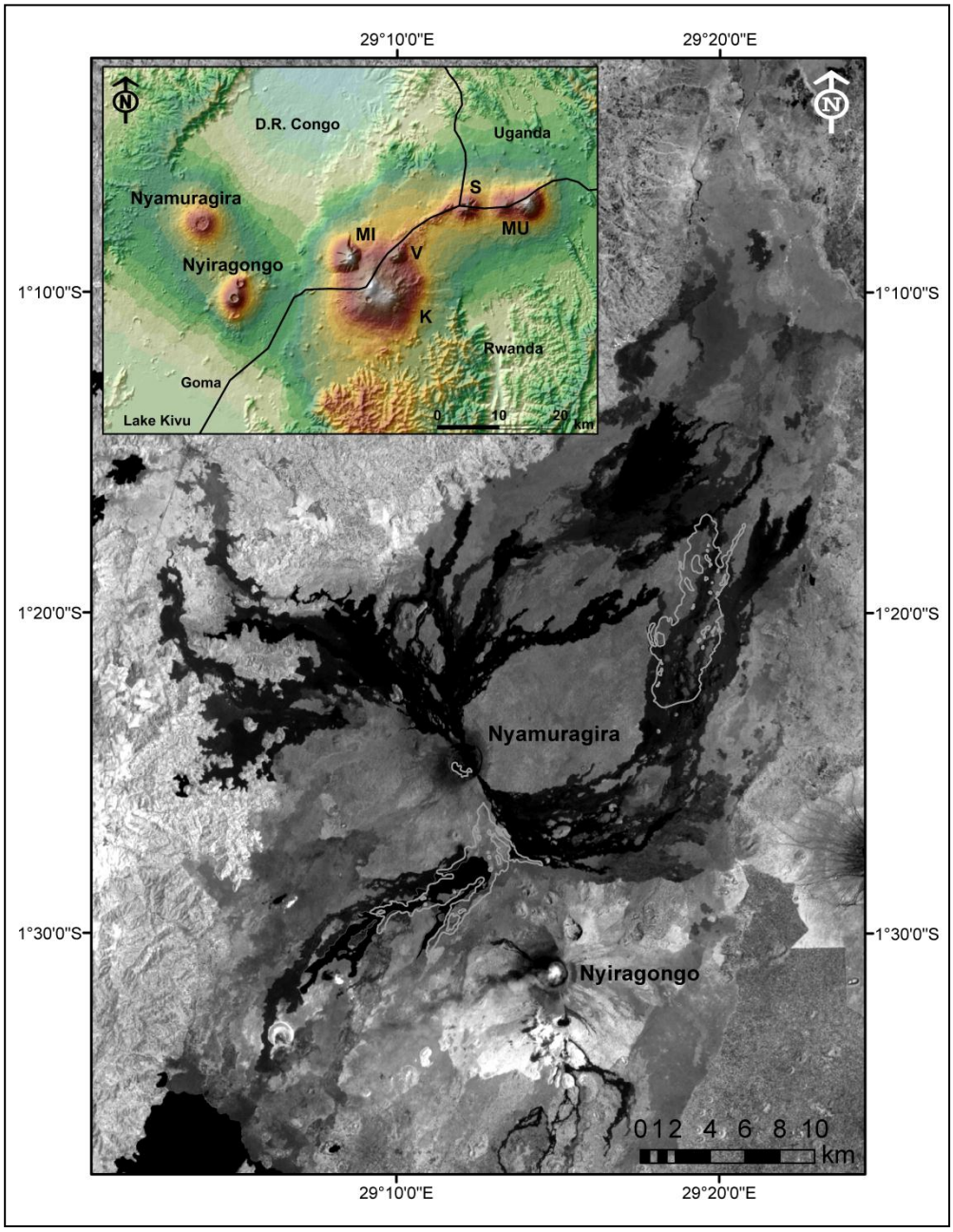

Figure 2.1 The inset map, an ASTER GDEM (http://asterweb. jpl.nasa.gov/gdem.asp), shows the location of Nyamuragira (D.R. Congo) within the western branch of the East African Rift near the Rwandan border. Inactive Virunga volcanoes are shown: K- Karisimbi; Mi- Mikeno; S- Sabinyo; V- Visoke; Mu- Muhavara. The larger Landsat image (http://glovis.usgs.gov/), acquired 21 February 2005 (band 4), reveals Nyamuragira's prolific lava flows including outlines of the 2006, 2010, and 2011 flows we mapped using automated classification.

(2005) used optical satellite data to supplement and/or verify the ambiguous flow boundaries resulting from the radar imagery. Smets *et al.,* (2010) used individual SAR images and SAR pairs from ERS 1/ERS 2 (C-band), ENVISAT (C-band), and JERS (L-band: 23.5 cm) satellites for the purpose of delineating overlapping lava flows near the summit through textural differences between flows. However, they make it clear that a combination of radar and optical imagery was necessary. In this study, we focus on an optical satellite dataset, since these data are more readily available than radar for routine mapping efforts.

Optical satellite data are often free and have been used to map lava flows utilizing various approaches (Abrams *et al.,* 1991; Kahle *et al.,* 1995; Abrams *et al.,* 1996; Lu *et al.,* 2004), including on-screen digitizing (tracing) of lava flow boundaries and automated classification using supervised and unsupervised algorithms. Automated classification, performed via image processing software, evaluates every pixel in a scene and then groups the pixels with similar values (e.g., digital number, reflectance, radiance) into a specified number of classes. Image processing software can be costly, although freeware exists (e.g., MultiSpec: https://engineering.purdue.edu/~biehl/MultiSpec/; GRASS GIS: http://grass.fbk.eu/), which would allow a volcano observatory with limited funds to carry out unsupervised classification and digitization on optical satellite data. Here, we use automated classification methods with Landsat Multi-spectral Scanner (MSS), Thematic Mapper (TM), and Enhanced Thematic Mapper (ETM+) and Earth Observing-1 (EO-1) Hyperion and Advanced Land Imager (ALI) imagery to delineate lava flows from Nyamuragira volcano.

One of the advantages of Nyamuragira's humid tropical location is that its lava flows are usually emplaced onto heavily forested flanks, resulting in strong contrast between lava and vegetation, typically allowing rapid and automated mapping. Visible to short-wave infrared (VSWIR) satellite imagery, therefore, proved optimal for mapping the Nyamuragira lava flow field. This was our main motivation for choosing the Landsat-Hyperion-ALI dataset. These data have a low cost (most data are now free) and the Landsat data in particular

provide a longer-term archive (beginning in 1972) relative to other VSWIR sensors such as the Advanced Spaceborne Thermal Emission and Reflection Radiometer (ASTER), the Indian Remote Sensing Satellites, and Système Pour l'Observation de la Terre (SPOT). An additional advantage is that the free dataset and processing software would allow researchers or observatories in developing countries with limited resources to efficiently update the map when new lava flows occur. Due to the lack of a cloud-free Landsat scene for mapping the 2010 and 2011 flows, we used Hyperion and ALI images, respectively. We show that our area and volume estimates agree well with the estimates of Smets *et al.,* (2010), which suggests that the methods we used with free satellite imagery are promising and cost-effective for Nyamuragira, as well as for similar lava flows on other volcanoes.

2.2 Data acquisition and mapping methodologies

2.2.1 Data preparation

The specifications and characteristics of the Landsat MSS, TM, and ETM+, Hyperion, and ALI scenes obtained for mapping are located in Table 2.1 and Table 2.2, respectively. For consistency, our original intent was to use only Landsat data, but the clearest Landsat image of the 2010 flow available to date (18 January 2010) was acquired while the volcano was still erupting. An eruption cloud obstructed part of the flow and the northern-most vent was issuing hot lava, which saturated the SWIR bands. The application of automated processing techniques was not possible due to these effects. In place of Landsat, we used a Hyperion scene acquired on 28 May 2010 to complete the 2010 mapping. For the 2011 flow, we had similar problems. The eruption began on 6 November 2011 and it is still continuing at the time of writing. Current activity includes lava flows and occasional Strombolian eruptions, although at a lower level of intensity than previously observed. A cloud-free Landsat scene (acquired on 9 February 2012) does exist, but it captured the erupting lava flows, which saturated the SWIR bands and prevented automated processing. In place of this Landsat scene, we used an ALI image acquired on 3 January 2012. Since Nyamuragira was degassing during the ALI acquisition, eruption clouds did obstruct a small southern portion

of the flow in this image. However, we were able to use the Landsat scene from February 9th to make minor modifications to the flow once the automated classification was performed on the ALI image.

The Hyperion image was acquired ~3 months after the 2010 flow emplacement, and the ALI image was acquired ~1 month after the 2011 eruption began, which preserved a good contrast between the fresh 2010/2011 lava flows and the surrounding older lava flows and vegetation. For the Landsat dataset, images acquired closest to the date of flow emplacement were used to map that particular flow. This ensured the largest contrast between fresh lava flow and surrounding vegetation and/or older, weathered lava flows. For example, the 1986 Landsat image captured the 1986 Nyamuragira flow as it was being emplaced, saturating the SWIR bands, and preventing the application of automated classification methods. The next best (cloud-free) Landsat image was acquired in 1987 and provided a clear image on which to apply the automated techniques, resulting in a robust classification. By choosing Landsat scenes as close to the eruption date as possible, we also increased the possibility of mapping lava flows prior to the emplacement of subsequent, overlapping flows.

All of the scenes were reprojected to the 15 June 2000 image using a UTM zone 35 south projection and the WGS 84 datum. Only bands 1-5 and 7 from the Landsat TM and ETM+ scenes were used, whereas bands 41-76 with 0.76-0.90 μm wavelengths from the hyperspectral Hyperion scene were used. These Hyperion wavelengths correspond to a single Landsat band (band 4), providing much higher spectral resolution than the single Landsat band. This band (4) was found to be most responsive to lava flow weathering and vegetation with age (Abrams *et al.,* 1991). ALI and Landsat VSWIR bands cover a similar spectral range, although ALI data include three additional bands, providing a better spectral resolution than Landsat (Table 2.1). All nine ALI VSWIR bands (1′-7), therefore, were used to map the 2011 flow. The thermal infrared (TIR) band did not prove to be crucial for our mapping; thus, excluding this band from the Landsat datasets provided a fixed spatial

resolution for all bands. The Landsat MSS scene was resampled to 30 m in order to allow a direct comparison with the TM/ETM+ imagery.

2.2.2 Principal components analysis

Principal components analysis (PCA) on both TIR and VSWIR satellite data has been successfully used to map lava flows and volcanic tephra units for individual and multiple flows (e.g., Abrams *et al.,* 1991, 1996; Legeley-Padovani *et al.,* 1997; Wiart *et al.,* 2000). A PCA was performed on the Landsat and ALI datasets, but not on the Hyperion image as the latter included only 0.76-0.90 μm wavelengths. The Landsat and ALI images were subset around the lava flow field to permit a faster analysis because fewer pixels were input into the PCA.

For each multi-spectral satellite image, several bands may contain similar information. The purpose of a PCA is to reduce this redundancy by comparing the spectral information in each band with that in every other band via an orthogonal transformation, so that the first principal component (PC) represents the greatest variance of the data, the second PC represents the second greatest variance of the data, and so on. The number of PCs generated is equivalent to the number of input bands; for example, 6 PCs were generated from the Landsat TM and ETM+ data. Since the PCA technique compresses the useful spectral information into fewer, uncorrelated components, the scene can be represented by ~3 components rather than 6 bands and overall noise is reduced.

2.2.3 PCA evaluation

Prior to attempting a classification of the flows, three PCs were chosen that best highlighted the flow of interest (Figure 2.2). For roughly half of the lava flows, the first three PCs provided the best contrast between the lava flow and the surroundings and were, therefore, combined for subsequent unsupervised classification. We only deviated from

Table 2.1
Specifications of Landsat, Hyperion, and ALI sensors.

	Landsat MSS	**Landsat TM**	**Landsat ETM+**	**Hyperion**	**ALI**
Dates of Operation; Sensor	1972-1983; 1-3	July 1982-Nov 2011; 4-5	April 1999-present; 7	Nov 2000-present	Nov 2000-present
Spectral Bands	Band 4/1 (0.5–0.6 µm) Band 5/2 (0.6–0.7 µm) Band 6/3 (0.7–0.8 µm) Band 7/4 (0.8–1.1 µm)	Band 1 (0.45–0.52 µm) Band 2 (0.52–0.60 µm) Band 3 (0.63–0.69 µm) Band 4 (0.76–0.90 µm) Band 5 (1.55–1.75 µm) Band 7 (2.08–2.35 µm)	Band 1 (0.45–0.52 µm) Band 2 (0.52–0.60 µm) Band 3 (0.63–0.69 µm) Band 4 (0.77–0.90 µm) Band 5 (1.55–1.75 µm) Band 7 (2.09–2.35 µm)	Band 41-76 (0.76-0.90 µm)	Band 1' (0.43–0.45 µm) Band 1 (0.45–0.52 µm) Band 2 (0.53–0.61 µm) Band 3 (0.63–0.69 µm) Band 4 (0.78–0.81 µm) Band 4' (0.85–0.89 µm) Band 5' (1.2–1.3 µm) Band 5 (1.55–1.75 µm) Band 7 (2.08–2.35 µm)
Spatial Resolution	80 m (all bands)	30 m (band 1-5 & 7: visible, near infrared, and short wave infrared)	30 m (band 1-5 & 7: visible, near infrared, and short wave infrared)	30 m (all bands)	30 m (bands 1'-7; visible, near infrared, and short wave infrared)
Temporal Resolution	16-18 days	16 days	16 days	16 days	16 days

Table 2.2

Landsat, Hyperion, and ALI scenes used to map Nyamuragira lava flows. GloVis is a USGS web site from which optical satellite imagery can be downloaded (http://glovis.usgs.gov/).

Scene	Date of Acquisition	Image ID (Path: 173, Row: 61)	Source
Landsat MSS 2	March 12, 1975	LM21860611975071AAA03	GloVis
Landsat TM	December 4, 1984	LM51730611984339AAA03	GloVis
	July 19, 1986	LT51730611986200XXX01	GloVis
	August 7, 1987	LT51730611987219XXX05	GloVis
	August 4, 1989	LT41730611989216XXX06	GloVis
	January 17, 1995	LT51730611995001AAA01	GloVis
	February 2, 1995	LT5173061009503310	GloVis
Landsat ETM+	December 6, 1999	LE71730611999340SGS00	GloVis
	June 15, 2000	LE71730612000167EDC00	GloVis
	September 3, 2000	LE71730612000247EDC00	GloVis
	December 11, 2001	LE71730612001345SGS00	GloVis
	January 31, 2003	LE71730612003207EDC01	GloVis
	February 21, 2005	LE71730612005052ASN00	GloVis
	January 15, 2009	LE71730612009015ASN00	GloVis
	September 28, 2009	LE71730612009271ASN00	GloVis
	January 18, 2010	LE71730612010018ASN00	GloVis
Hyperion	May 28, 2010	EO1H1730612010148110KF	GloVis
ALI	January 3, 2012	EO1A1730612012003110PF	GloVis

using PCs 1-3 when other PCs more clearly highlighted the flow of interest (e.g., 1981, 1984, and 2001, as well as parts of the 1996 and 2000 flows). To investigate why deviations from PCs 1-3 were necessary, we examined our factor loading calculations (Appendix A) for each of the Landsat scenes we used. The factor loadings are coefficients of the PCA transformation and determine which bands of the original imagery contributed most to each PC.

Regardless of whether we used PC 1-3 or deviated from this combination, the most dominate contributions to the PCs used were from bands 1, 2, 3, and, less extensively, band

4 of the original data. This appears to correlate with the large amount of vegetation in each Landsat scene. Band 1 is responsive to waterbodies and blue chlorophyll absorption in vegetation, band 2 is responsive to blue and red chlorophyll absorption and green reflectance of healthy vegetation, band 3 is responsive to red chlorophyll absorption of healthy vegetation, and band 4 is sensitive to the amount of vegetation biomass in the scene. In only two instances did band 5 contribute to a PC used (Appendix A)- for the 1996 and 2000 flows we used PCs 1, 2, and 4. PCs 1 and 2 comprised reflectance from bands 1, 2, 3, and 4, while PC 4 comprised reflectance from bands 1, 3, and 5. Band 5 is sensitive to turgidity (water) in plants. This Landsat scene was acquired in September, which is within one of the two annual rainy seasons in the Virunga (http://www.eoearth.org/article/Virunga_National_Park,_Democratic_Republic_of_Congo#gen7); therefore the response in band 5 probably results from moisture-rich vegetation. As most of the reflectance in each scene results from the abundant vegetation in the area, the flows of interest were easily identifiable due to the stark contrast between vegetation and barren lava.

The user determines the number of classes to be generated within the classification program. Since our input into the classification program are three PCs, and PCA is an orthogonal transformation of the original data, the classification program creates each class based on the distribution of the data along the entire length of the first PC axis. Because the first PC contains the greatest variance of data, there is an increased separation of reflectance between, for example, bare rock/soil and vegetation along this axis compared to the raw data (see Jensen (2007) for more detail). This separation appears to result from the contrast between recent lava flows, which have lower reflectance, and older lava flows and forest, which have greater reflectance due to weathering and (re)vegetation. A qualitative assessment of this separation is shown in Figure 2.2. The 1986 lava flow is noticeably darker than its surroundings in PC1 and PC4, indicating a clear spectral separation. Color-composites of the original Landsat image (2.3a) and the combined 3-PC image (2.3b) are deviations from PCs 1-3 were shown to illustrate that the PCA allows a more clear

separation of lava flow and surrounding vegetation. This may not always be apparent in the original imagery and, therefore, transformations of this kind are valuable.

2.2.4 Unsupervised classification

The three PCA images chosen were cropped to include the area just around the flow being mapped, which again permitted a faster, more accurate classification because fewer pixels had to be evaluated and grouped into classes. Since a PCA was not performed on the Hyperion scene, the original image was cropped to include the areas just around the 2010 flow and an unsupervised classification was carried out on the original data. Relative locations and extents of the flows were determined based on the Smithsonian's GVN reports (Smithsonian Institution 1971-2011) and verified by observing two scenes bracketing the flow's emplacement. As discussed above, an unsupervised classification (also known as ISODATA; see Jensen (2007) for more detail) is carried out using digital image processing software such as ERDAS Imagine (Appendix B). The unsupervised classification program compares the reflectance of each pixel to every other pixel in the scene and groups similar reflectances into classes.

A supervised classification was also attempted to determine if this might produce a more accurate lava flow map. In this type of classification, training sets are acquired for each land feature (lava flow, vegetation, water, cities) and then input into the classification program. Compared to our unsupervised classification results, the supervised classification method did not produce a more accurate lava flow map. Acquisition of training sets is time-consuming and, although the results of this method are similar to the unsupervised classification, we found the latter to be the most efficient method.

We choose the 1986 and the 2004 Nyamuragira lava flows to demonstrate our methodology, as the former was one of the more apparent flows to map and the latter

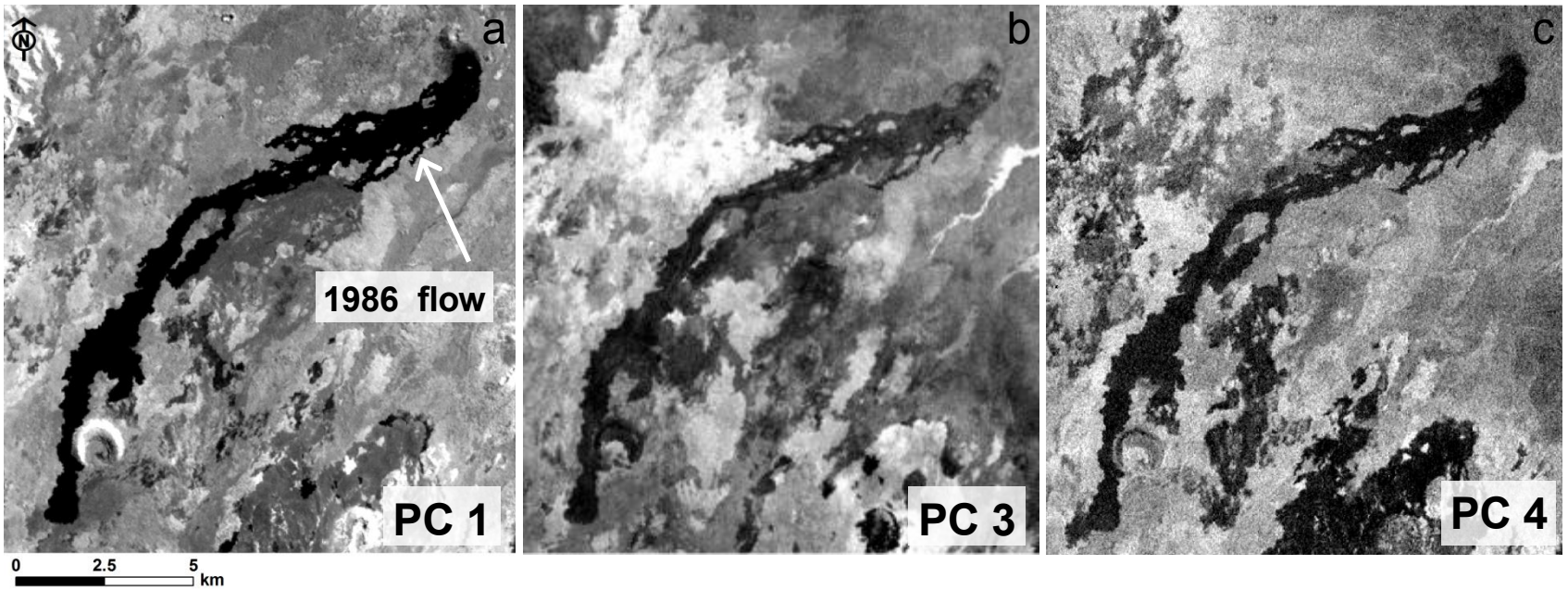

Figure 2.2 Images showing the three principal components (PCs; 1(a), 3(b), 4(c)) input into the unsupervised classification module (ISODATA) to map the 1986 Nyamuragira lava flow. These three PCs best discriminated the flow from the rest of the scene.

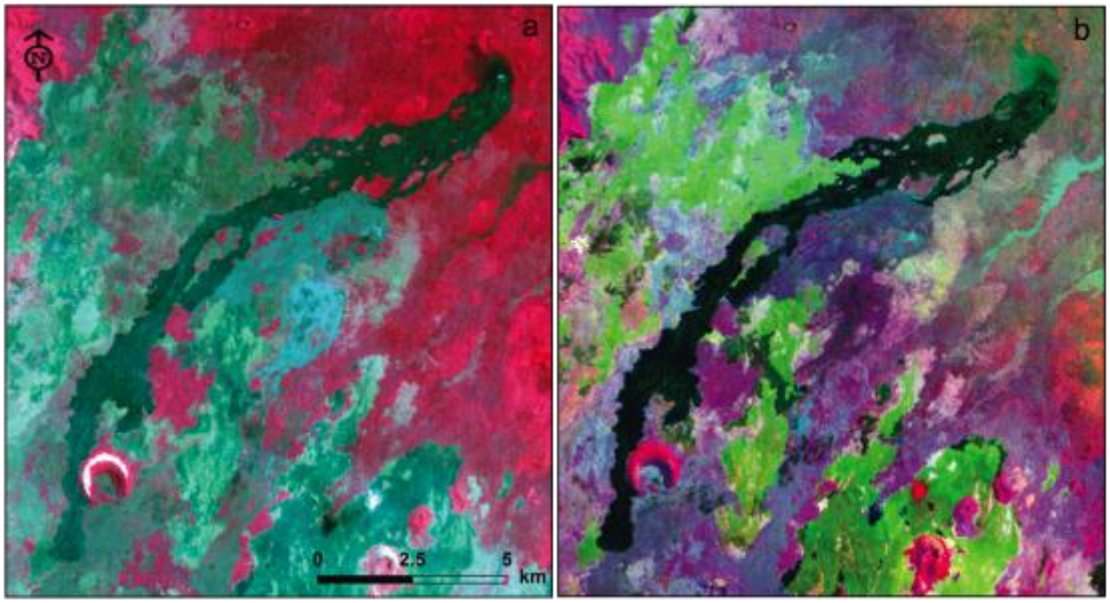

Figure 2.3 Color-composite images of (a) the original Landsat data (acquired 7 August 1987) with bands 4, 3, and 2 displayed in red, green, and blue, and (b) the three PCs (1, 3, 4) displayed in red, green, and blue. The 1986 Nyamuragira lava flow is more easily distinguished, both visually and spectrally, in the PC image compared to the original image.

illustrates the limitations of the methods we used. The entire 1986 flow was erupted onto considerably older and more weathered flows (1938-1940, 1948, and 1976-77), providing ample spectral contrast with its surroundings (Figure 2.3; Figure 2.4a). The 2004 lava flow, on the other hand, was more difficult to map using this method. Near the summit area, spectral contrast between the 1998, 2001, 2002, and 2004 lava flows was very low (Figure 2.4d). This inhibited both visual separation of the 2001, 2002, and 2004 flow boundaries and the ability of the unsupervised classification to classify the separate flows. Further down the flanks, the spectral contrast increases, allowing a clearer visual separation, as well as automated classification.

2.2.5 Mapping the delineated lava flows

After the unsupervised classification, we found that some of the lava flows were defined by one class (1971, 1984, 1986, and 1991), while the remaining flows were defined by more

than one class. The latter was due to spectral variation within the flow, potentially caused by early revegetation of parts of the flow (if the imagery used to map the flow was acquired over ~5 years after flow emplacement) or by intra-flow features such as varied lava textures (e.g., Spinetti *et al.,* 2009) resulting from slope changes. We also found that, in some instances, the lava flow and parts of the surroundings were included in the same class (e.g., Figure 2.4a- yellow spots surrounding the 1986 flow, which is also displayed in yellow).

Using a module in ERDAS Imagine ("clump"), we were able to reassign the surrounding spots to a different class number and separate these from the main flow (Figure 2.4b). At this point, the class or classes that were identified as the flow were reassigned a value of one and the remaining classes were assigned a value of zero (Figure 2.4c). Creating this binary image was necessary to clearly delineate the flow from the surrounding non-flow features. The area of each flow was determined by multiplying the pixel count of the flow by the pixel area (Table 2.1).

In the absence of recent field-based lava flow thickness measurements, we used a previously reported value to determine a volume for each lava flow. Kasahara *et al.,* (1991) determined that an average thickness of 3 m was most appropriate based on compiled research of past Nyamuragira eruptions and, therefore, we also adopt this value. We considered DEM subtraction to better constrain this value, but the vertical resolution of available DEMs is too coarse to improve upon the thickness estimate of Kasahara *et al.,* (1991) via DEM subtraction. The 3-m thickness of Nyamuragira's flows is significantly less than the average 5 -16 m vertical accuracy of DEMs created from satellite imagery such as ASTER (7-15 m; Hirano *et al.,* 2003), SPOT (~5 m; Endreny *et al.,* 2000), or SRTM (~16; Rodriguez *et al.,* 2005) data. IKONOS-derived digital surface models (DSMs) have a vertical accuracy of 2-5 m, although the lower estimate was a result of flat terrain, and for vegetated surfaces, like Nyamuragira, this value increases (Poon and Fraser 2005). DEMs derived from Light Detection and Ranging (LiDAR) data are more accurate (0.5 m; Liu *et al.,* 2007), although LiDAR topographic data of the Virunga region are unavailable.

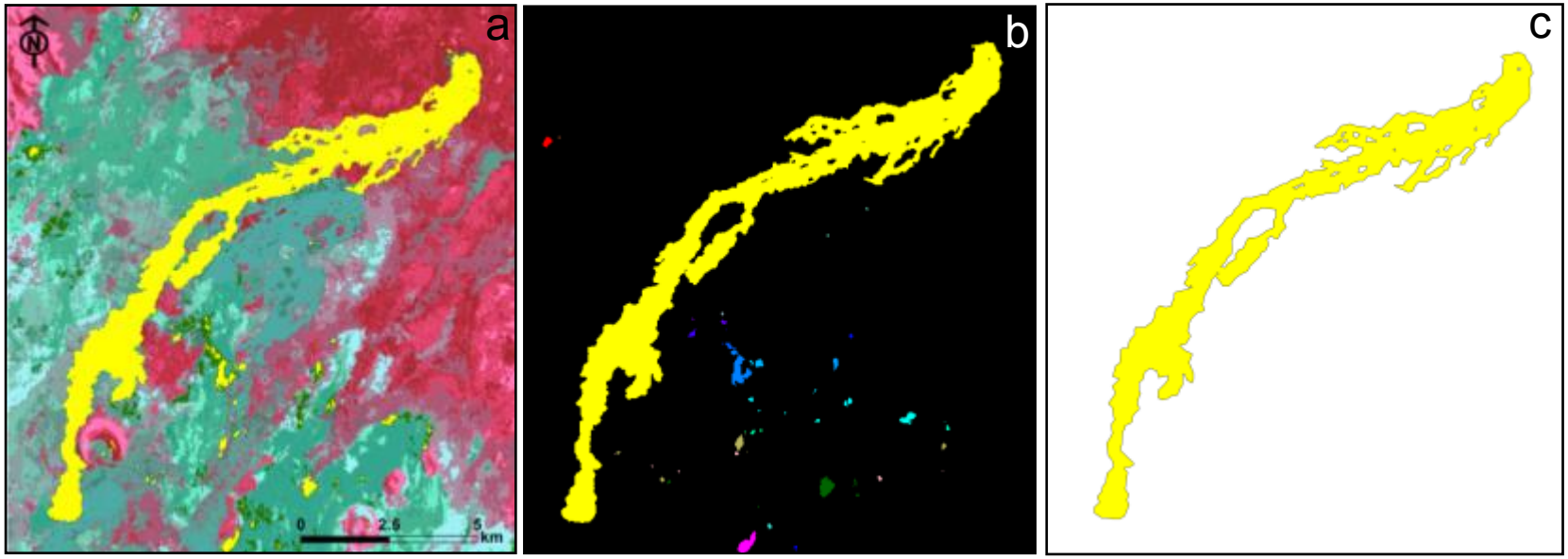

Figure 2.4 (a) Results of the unsupervised classification of the 7 August 1987 Landsat scene, showing the 1986 flow highlighted in yellow. Yellow patches around the 1986 flow were falsely classified; (b) The false pixels were easily reassigned as "non-flow" using a module in ERDAS Imagine (clump); (c) The final result, a binary image, is produced by reassigning the background classes as "0" and the lava flow as "1", which allowed a clear separation of the 1986 flow; (d, below) Results of an unsupervised classification of the 21 February 2005 Landsat scene. The 2004 was more difficult to map as the overlapping flows emplaced with ~1 year of each other had very similar spectral signatures (see black box). However, note how the flows become easier to separate (spectral signatures are different from surroundings) down the volcano flanks.

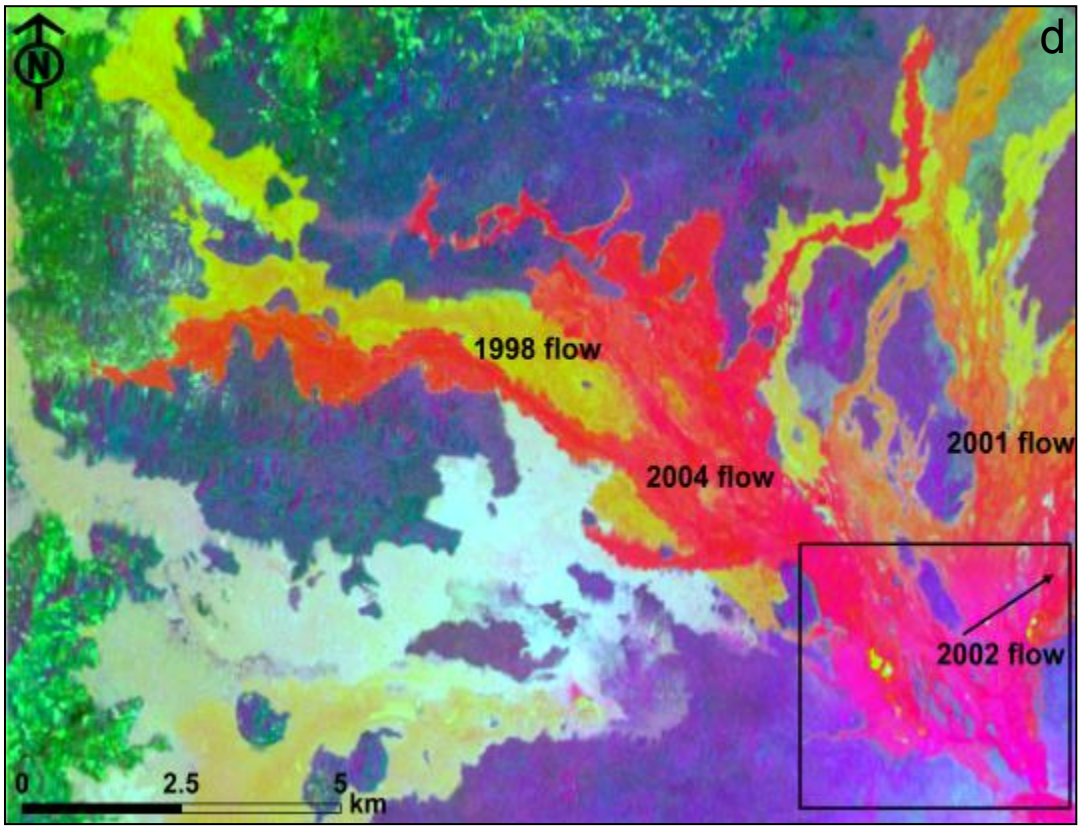

Even if the political situation improves, acquisition of this type of data would be very costly due to the large spatial extent of the flows.

2.2.6 Special case: MSS imagery

Landsat MSS has fewer spectral bands than the TM and ETM+, requiring a different processing scheme for the 1975 MSS image prior to the unsupervised classification. The 1971 lava flow abutted a body of water. The available Landsat MSS bands detected similar spectral signatures for both water and lava, rendering them indistinguishable through the unsupervised classification. Masking the water from the stacked PC image remedied the effect and an unsupervised classification was successfully performed on the 1975 image.

2.3 Lava flow map and derived volumes

2.3.1 Comparison of our lava volumes with previous studies

The map of Nyamuragira lava flows produced from the Landsat, Hyperion, and ALI image analysis is shown in Figure 2.5. Table 2.3 shows lava flow volumes calculated using the technique described above, and a comparison of our results with previously reported lava volumes (Kasahara *et al.,* 1991; Colclough 2005; Smets *et al.,* 2010). Nyamuragira eruptions from 1967-2011 produced between 0.005 and 0.136 km^3 of lava per eruption. While our data generally agree with the volumes reported by Kasahara *et al.,* (1991) for the 8 eruptions between 1967 and 1991, there are some differences (Table 2.3). Colclough (2005) estimated minimum lava flow volumes for the 1998 (71 x 10^6 m^3) and 2001 (133 x 10^6 m^3) Nyamuragira eruptions; our estimates agree well with their results for the 2001 flow and are within 20% of their results for the 1998 flow. In a comparison with Smets *et al.,* (2010), our estimates agree to within 10% of theirs, except for the 1998 flow (17% difference).

On 31 May 2003, Landsat ETM+ lost its scan line corrector (SLC) and, as a result, stripes of missing data appear in the image. The imagery used to map the 2006 flow was affected by this condition. We were able to map the 2006 flow with the same methods used to map the older flows, although this scene did require some digitization in ArcGIS after the binary image from the classification was complete, particularly in the area covered by clouds. The flow was delineated with the aid of a Landsat ETM+ scene acquired on 28 September 2009, as well as an ASTER image acquired on 31 August 2007. Eight out of the nineteen flows (1976, 1980, 1991, 1989, 2000, 2001, 2003, and 2004) required small amounts of digitization after the classification to remove falsely classified flow surroundings, which were not possible to separate using the digital image processing software. Four out of these eight instances were associated with the overlapping flows near the summit area. Due to either atmospheric or eruption clouds obstructing parts of the 1967, 1996, 2000, 2006,

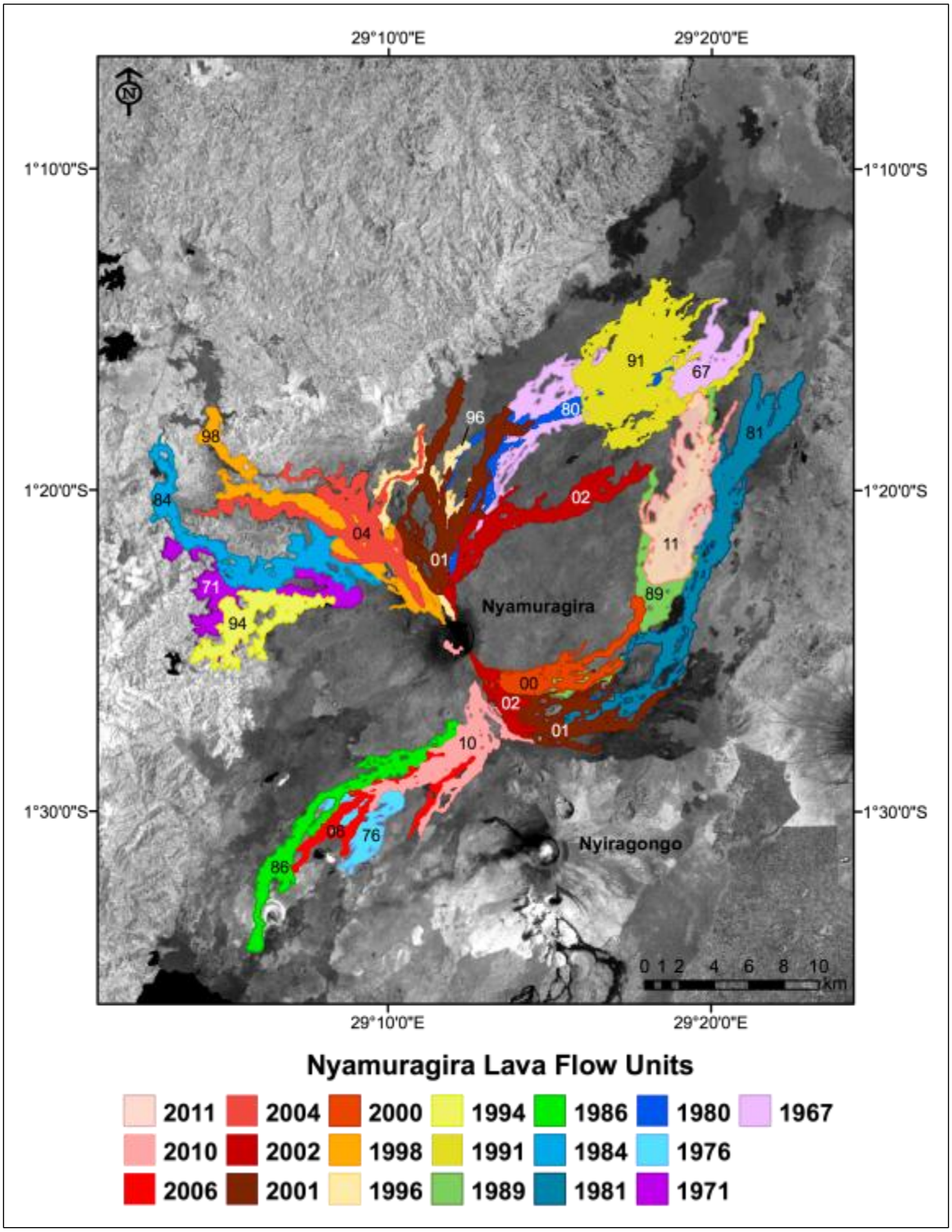

Figure 2.5 Map of Nyamuragira lava flows erupted from 1967-2011. The base map is a Landsat ETM+ scene (http://glovis.usgs.gov/) acquired on 21 February 2005 (band 4).

2010, and 2011 flows, these also required small amounts of digitization. The remaining five flows (1971, 1981, 1984, 1986, and 1994) were mapped with no post-processing.

2.4 Discussion

2.4.1 Temporal changes in lava flow spectral signature

From our PC analyses, we conclude that most of the spectral variation within the Landsat and ALI scenes is due to vegetation and water reflectance, and that the comparatively low reflectance of the lava flows (bare rock) provides high contrast with the surrounding vegetation that allows the flows to be easily mapped with unsupervised classification methods. If a new lava flow is emplaced on older but relatively recent lava, the efficacy of the technique depends on the vegetation and weathering rate of the flows. Ground, aerial, and satellite studies of basaltic flow fields have shown that changes in VSWIR (0.4-2.4 μm) spectral signatures result from electronic transitions in iron in various oxidation states, as well as the increasing extent of vegetation, as weathering progresses (Bonneville *et al.,* 1988; Abrams *et al.,* 1991; Kahle *et al.,* 1995; Spinetti *et al.,* 2009). In order to assess how individual flows change through time with respect to vegetation and weathering, we must look at the reflectance of each lava flow, instead of the reflectance from the entire scene. To do this, we used statistics from one of the Landsat scenes, which provided quantitative information about the weathering and vegetation processes that occur on these flows over time. The purpose of this exercise is to determine how quickly Nyamuragira flows vegetate and to investigate if a new flow, erupted over an older flow, can be distinguished spectrally from the older flow.

To determine quantitatively how lava flow spectral reflectance changes over time, we used the Landsat ETM+ scene acquired on 21 February 2005 as this scene provides a cloud-free view of all but the 2006, 2010, and 2011 flows. We corrected this image for atmospheric

and radiometric effects using the COST model (Chavez 1996) but performed no PCA or unsupervised classification on the image in order to conserve the characteristics of the original data. The advantages of using a single image are that vegetation, sun angle, and atmospheric conditions are constant. Otherwise, if two images acquired on different days are compared, parameters such as seasonal differences in vegetation may affect the spectral signatures and not allow a direct evaluation. We measured the reflectance spectrum of each Nyamuragira lava flow at several locations along the flow and averaged the values. This allowed us to compare reflectance spectra and determine how the reflectance changes with age. A terminal lobe of the 1958 Nyamuragira lava flow was also transected to obtain an older end member. Only the terminus of the 1958 flow was exposed in the 2005 image and, therefore, a near-vent sample could not be acquired. In fact, several flows within this image were overlapped by more recent flows and did not provide a full vent-to-terminus sampling. In these situations, as many measurements as possible were taken within the exposed area. We obtained an average band-4 reflectance of the 2010 flow (0.05) from the Hyperion scene and a spectral profile of the 2011 flow (band 4 = 0.01) from the ALI scene. These values are lower than 1967-2005 band-4 reflectances shown in Figure 2.6. Spectral profiles were also sampled for vegetated areas around the flows and these reflectances were the highest of all sampled (~0.7).

Spectral variations in the visible portion of the spectrum (bands 1-3) are typically associated with changes in the oxidation state of iron in lava flows as the flows age (Abrams *et al.,* 1991). We do not see any systematic change in the reflectivity of bands 1-3 with age. Instead, we found the largest variation in spectral reflectance in ETM+ band 4 and so we focus on the interpretation of this band (Figure 2.6). Reflectance in band 4 clearly increases with flow age, which we assume is in part due to vegetation growth (biomass) and the spectral 'red-edge'; the rapid increase in the reflectance of vegetation at near-IR wavelengths (Abrams *et al.,* 1991; Filella and Penuelas 1994; Seager *et al.,* 2005). A general increase in band-4 reflectivity with lava flow age was also found in a multi-parameter study of nine alkaline Etnean lavas (1607-2003), in which field data and lava

flow spectral signatures from a ground-based spectroradiometer and hyperspectral satellite data were compared (Spinetti *et al.,* 2009). They found that vegetation growth and weathering with time were responsible for the increase, while tephra cover (differences in grain size) decreased a lava flow's reflectivity. During a field campaign in 2006, we noted that tephra was mainly found only near-vent at the 1986 and 2006 Nyamuragira eruption vents. If this is true for the rest of the vents, this suggests that tephra does not have a strong influence on the spectral signatures along the length of the flow.

Using SAR, Rodriguez *et al.,* (2001) found that Nyamuragira lava flows vegetate completely within ~30 years. In lava flows under 30 years old, they found a positive correlation between the SAR signal and soil formation (weathering)/vegetation of Nyamuragira flows. We investigated how vegetation changes over time at Nyamuragira by utilizing the Normalized Difference Vegetation Index (NDVI: band 4-band 3/band 4+band 3), which determines the amount of green vegetation in a scene. The result is an image in which pure black represents no healthy vegetation and pure white represents complete healthy vegetation cover (Figure 2.7). We find that the NDVI values increase with increasing lava flow age and indicate revegetation within ~5 years of lava flow emplacement. Vegetation, and to some degree weathering, therefore, provides the best explanation for our results. Exceptions include the 1998 flow (on the western flank), which has a higher reflectance than expected for its age and the 1991 flow (on the northern flank), which has a lower reflectance than expected. The flows that deviate from the overall band-4 increase could have weathered and/or vegetated differently than surrounding flows. Future ground-based investigations would be helpful to resolve these differences. Based on the spectral profiles and NDVI results, it appears that most flows will start to revegetate and weather sufficiently within ~5 years in order for band-4 reflectances and NDVI values to differ markedly from a fresh flow. This contrast greatly facilitates the mapping of lava flows emplaced through heavily vegetated areas (forest) and on top of previously erupted flows (older flows which are in the process of revegetating) in the Virunga region.

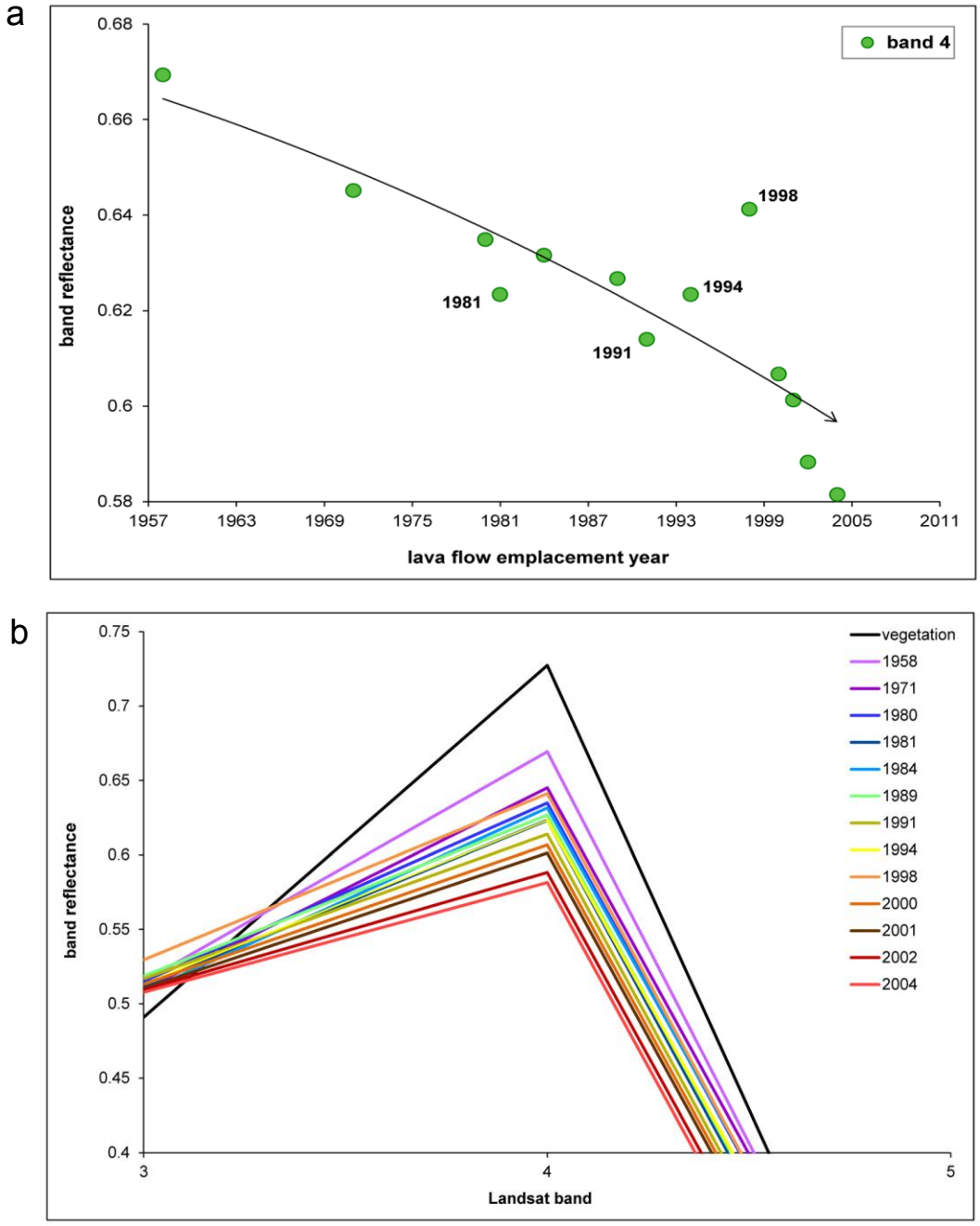

Figure 2.6 Spectral profiles from transects of Nyamuragira lava flows (1958-2005) from vent to terminus (when possible) are averaged as single points for each flow year. A clear increase in band 4 reflectance indicates revegetation of the flows as they age. The Landsat ETM+ scene used for these transects was acquired on 21 February 2005, hence the lack of the 2006, 2010, and 2011 data points. Band-4 reflectances of the 2010 and 2011 lava flows from Hyperion and ALI imagery, respectively, are lower than 1958-2005 values. (b) A graphical presentation of the above points illustrates the flows that deviate from the progression.

2.4.2 Lava flow volume errors

We identify three sources of potential error within our volume estimates using Landsat, Hyperion, and ALI data: 1) inaccurate lava flow boundaries due to the flow edge occupying only part of a Landsat/Hyperion/ALI pixel; 2) erroneous inclusion of surrounding substrate as lava flow; and 3) the average lava flow thickness used. Even in the most extreme case (an off-set of one pixel for the entire perimeter of the largest lava flow, 2001), the perimeter of the flow only accounts for ~16% of the total flow area. In reality, these errors would be negligible as some perimeter pixels will be within and others outside of the chosen boundary. The second error was greatest when overlapping flows near the summit were difficult to delineate (e.g., it would be a ~20% difference if we assumed that the 2004 flow in Figure 2.4d extended to the summit, compared to its actual extent, seen in Figure 2.5). However, the largest source of error, as Smets *et al.,* (2010) also points out, was the flow thickness. Calculating volumes with a 1 and 5 m thickness (3±2 m) results in a 200-400% difference in the largest flow volume (2001) compared to the volume calculated with the average 3 m thickness. Since Colclough (2005) and Smets *et al.,* (2010) also use the 3 m average lava thickness suggested by Kasahara *et al.* (1991), our volume estimate comparisons are actually comparisons of lava flow areas. The good agreement between our data and these prior estimates suggest that we have similarly detected flow boundaries.

2.5 Conclusions

Mapping Nyamuragira's lava flows using PCA and automated unsupervised classification techniques has proven successful for most eruptions of the volcano since 1967. Unsupervised classification resulted in well-separated classes, which allowed easy discrimination of lava flows from surrounding features. The spectral contrast between flows that permits accurate mapping reflects (re)vegetation and weathering of the flows with time; revegetation progresses enough within ~5 years that the reflectance and NDVI values are significantly different than those of younger flows.

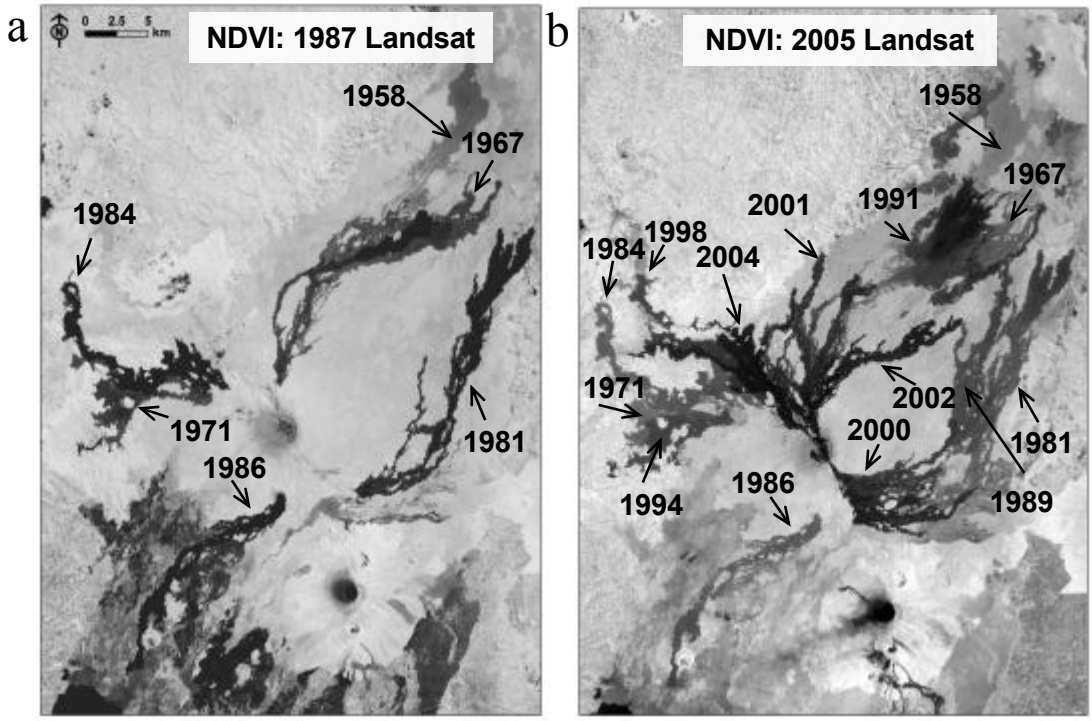

Figure 2.7 Normalized Difference Vegetation Index (NDVI) results for the Landsat TM scene (http://glovis.usgs.gov/) acquired on (a) 7 August 1987 and the (b) Landsat ETM+ scene acquired on 21 February 2005. The scale is 0-1; 0 is displayed as pure black and indicates no vegetation, where 1 is displayed as pure white and indicates complete vegetation. Revegetation of Nyamuragira lava flows results in significant NDVI increases, where lava flows ~5 years apart can be distinguished spectrally (and/or visually) from one another.

Overlapping lava flows emplaced within small time spans (e.g., the 2000 and 2001 flows to the SE or the 1998, 2002, and 2004 flows to the NW) required post-processing to delineate boundaries nearest the summit. This was accomplished through examination of images acquired prior to and after the emplacement of the flow in question to discern some of the overlapping boundaries. Experimenting with band combinations during the process allowed overlapping flows to be more easily separated. During this post-processing, more difficulty occurred when delineating flows closer to the summit crater, possibly due to the larger extent of overlapping flows, slope effects (e.g., thinner flows being more easily weathered), or satellite geometry.

We found that the use of automated classification methods with VSWIR satellite imagery for mapping lava flows is useful and cost-effective in regions such as Virunga, particularly for lava flows erupted through vegetation or emplaced on top of older, revegetating lava flows (>5 years). In these situations, where cloud-free satellite imagery is available, this method is faster than manually digitizing flow perimeter, especially for flows with intricate flow paths around elevated areas called kipukas. Even in situations where some digitization is needed after the automated classification routine due to cloud cover or spectral ambiguity, the automated methods can serve as an aid to mapping by performing the initial work more quickly. In the case of digitization alone (no automated methods), the time required to map a flow varies greatly and depends on the size of the flow, the dataset being used (e.g., resolution), and the level of flow complexity the user wants to display. With automated methods, on the other hand, the size of the flow does not significantly increase the processing time. Furthermore, the automated techniques and PCA provide insights into the underlying subtle spectral differences between the lava flows, whereas manual techniques do not.

In situations where overlapping flows are present, the automated method could be used with radar, which has proven useful for separating the flows based on roughness differences. In addition, the ability of radar to penetrate clouds is advantageous in this equatorial area due to the cloud cover that often obscures optical satellite imagery. However, VSWIR imagery is still often needed in conjunction with radar to delineate boundaries (e.g., Colclough 2005; Smets *et al.,* 2010). Our derived lava flow volumes for Nyamuragira eruptions from 1967-2010 are similar to those previously reported lava volumes (Kasahara *et al.,* 1991; Colclough 2005; Smets *et al.,* 2010). At the time of writing, this is the first estimated lava volume for the 2011 flow. Although lava flow overlap occurred more in flows emplaced between 1994-2010 due to a concentration of activity in a NW-SE rift zone since 1996, the percentage of overlap was small compared to the entire area of the flow.

ACKNOWLEDGEMENTS

Funding for this work was provided by the US National Science Foundation (grant EAR 0910795 to SAC). We would like to thank Scott Rowland for his thorough review of an earlier version of the manuscript, and two anonymous reviewers for their constructive comments, all of which greatly improved the manuscript.

CHAPTER 3: INSIGHT INTO VOLATILE BEHAVIOR AT NYAMURAGIRA VOLCANO (D.R. CONGO, AFRICA) THROUGH OLIVINE-HOSTED MELT INCLUSIONS[2]

ABSTRACT

We present new olivine-hosted melt inclusion volatile (H_2O, CO_2, S, Cl, F) and major element data from five historic eruptions of Nyamuragira volcano (1912, 1938, 1948, 1986, 2006). Host-olivine Mg#'s range from 71-84, with the exception of the 1912 sample (Mg# = 90). Inclusion compositions extend from alkali basalts to basanite-tephrites. Our results indicate inclusion entrapment over depths ranging from 0.1 to 5 km, which agree with independent estimates of magma storage depths (3-7 km) based on geophysical methods. Melt compositions derived from the 1986 and 2006 Nyamuragira tephra samples best represent pre-eruptive volatile compositions because these samples contain naturally glassy inclusions that underwent less post-entrapment modification than crystallized inclusions. Volatile concentrations of the 1986 and 2006 samples are as follows: H_2O ranged from 0.6-1.4 wt %, CO_2 from 350-1900 ppm, S from 1300-2400 ppm, Cl from 720-990 ppm, and F from 1500-2200 ppm. Based on FeO_T and S data, we suggest that Nyamuragira magmas have higher fO_2 (>NNO) than MORB. We estimate the total amount of sulfur dioxide (SO_2) released from the 1986 (0.04 Mt) and 2006 (0.06 Mt) Nyamuragira eruptions using the petrologic method, whereby S contents in melt inclusions are scaled to erupted lava volumes. These amounts are significantly less than satellite-based SO_2 emissions for the same eruptions (1986 = ~1 Mt; 2006 = ~2 Mt). Potential explanations for this observation are: 1) accumulation of a vapor phase within

[2] An edited version of this paper was published by AGU in *Geochemistry, Geophysics, Geosystems,* doi:10.1029/2011GC003699.

the magmatic system that is only released during eruptions, and/or 2) syn-eruptive gas release from unerupted magma.

3.1 Introduction

Volatiles in magma play a key role in the timing, magnitude, and style of volcanic eruptions (e.g., Parfitt and Wilson, 1994; Sparks, 1997; Sutton *et al.*, 2001; Edmonds and Gerlach, 2007; Shinohara, 2008), and can provide valuable insight into the depth and source of magma, whether the conduit is open or sealed and, potentially, the rate at which magma is erupting (e.g., Greenland *et al.*, 1985; Sutton *et al.*, 2001). Studies of volcanic degassing typically focus on either volatiles within the pre-eruptive magma or on gas emissions between or during eruptions. Here, we evaluate the dynamics of volcanic degassing through a combination of volcanic gas emissions, melt inclusion compositions, and associated erupted lava volumes. Melt inclusions are tiny droplets of magma trapped in growing crystals that are brought to the surface during eruption in lava flows or tephra deposits. The crystal serves as a pressure vessel, essentially preserving the original composition of the trapped magma, assuming that diffusion has not modified the composition significantly (see Gaetani and Watson, 2000; Spandler *et al.*, 2007; Portnyagin *et al.*, 2008). Olivine-hosted inclusions are often targeted since olivine is an early crystallizing phase, thus magma compositions over a range of depths (pressures) can be recorded. This allows pre-eruptive magma to be "sampled" from deep to shallow depths in the system. Pre-eruptive magma volatile concentrations derived from melt inclusion studies provide insight into crystallization processes, magma storage depths, and how volatiles contribute to magma ascent and eruption (Anderson, 1974; Devine *et al.*, 1984; Dunbar *et al.*, 1989; Wallace *et al.*, 1999; Wallace, 2001; Roggensack, 2001; Metrich *et al.*, 2004).

Volcanic gas emissions, on the other hand, are typically measured via ground- or satellite-based remote sensing methods. Satellite-based techniques are particularly useful for remote or hazardous volcanoes and large eruptions, but are usually restricted to measurements of

sulfur dioxide (SO_2), because the other dominant volcanic gases (water (H_2O) and carbon dioxide (CO_2)) are difficult to resolve from the atmospheric background. Here we examine the relationship between satellite-based volcanic SO_2 emissions measurements and SO_2 emissions derived from sulfur concentrations in melt inclusions coupled with magma eruption volumes.

Previous studies of basaltic eruptions in hotspot-related localities such as Hawaii and Iceland have suggested that remote sensing SO_2 flux estimates are similar to those derived from melt inclusion S concentrations combined with erupted magma volumes (petrologic method; e.g., Gerlach *et al.*, 1996; Wallace, 2001; Sharma *et al.*, 2004). However, for more silicic volcanic eruptions such as the 1991 Pinatubo eruption (Philippines), and for some mafic arc volcanoes, the SO_2 emissions measured via satellite remote sensing often greatly exceed sulfur yields predicted from petrological data (Wallace and Gerlach, 1994; Wallace, 2001; Witter *et al.*, 2005). This inequality, known as "excess sulfur", has been attributed to the presence of an exsolved vapor phase in the magma prior to eruption (Wallace, 2001; Shinohara, 2008). Although explosive eruptions of silicic arc magmas are more typically associated with excess sulfur, preliminary studies of SO_2 emissions and lava production for effusive basaltic hotspot and rift eruptions suggest that excess sulfur emissions may also occur in non-arc settings. In this contribution, we test the hypothesis using data from Nyamuragira volcano (*1.408ºS, 29.20ºE; 3058 m*), located in the extensional tectonic setting of the East African Rift. We focus on Nyamuragira's SO_2 emissions, comparing satellite-based remote sensing fluxes with those derived using the petrologic technique, and show that its SO_2 emissions are significant and cannot be reconciled with the amount of erupted lava.

Nyamuragira volcano, located in the Virunga region of the Democratic Republic of the Congo (D.R. Congo; Figure 3.1), is one of the most active volcanoes in Africa, with 16 effusive eruptions between 1980 and 2010. Due to the difficulties of ground-based work owing to the region's adverse political climate, volcanic gas emissions from Nyamuragira

have been evaluated via satellite methods (Carn and Bluth, 2003; Bluth and Carn, 2008). Satellite-based measurements of global volcanic SO_2 began in 1978 with the launch of the ultraviolet (UV) Total Ozone Mapping Spectrometer (TOMS; Krueger, 1983). The Ozone Monitoring Instrument (OMI) continued UV space-based monitoring of volcanic SO_2 emissions from September 2004, overlapping TOMS measurements for ~16 months, until the end of the TOMS mission in 2005 (Krotkov *et al.*, 2006; Yang *et al.*, 2007). Based on TOMS data, SO_2 emissions from Nyamuragira's frequent effusive eruptions were found to comprise a significant fraction (~10 %) of the global volcanic sulfur budget (Halmer *et al.*, 2002); it is estimated that ~25 Mt of SO_2 was released from Nyamuragira into the atmosphere between 1980-2004 (Bluth and Carn, 2008).

Nyamuragira erupts low-silica, alkalic lavas, including alkali basalts, hawaiites, basanites and tephrites (SiO_2= 43-56 wt%, K_2O+Na_2O up to 7 wt%; Aoki *et al.*, 1985). It erupts very fluid lava that can achieve flow rates of up to ~20 km/hr (Smithsonian Institution, 1982). Bluth and Carn (2008) suggested that syn-eruptive SO_2 emissions from Nyamuragira may correlate with effusive lava emissions. Hence, understanding the link between SO_2 emissions and erupted lava is important for future monitoring and hazard assessment and to further our understanding of degassing and eruption mechanisms at Nyamuragira. In addition, evolved alkalic melts have been important carriers of sulfur to the atmosphere in several globally significant eruptions, such as Tambora in 1815 (phonolite), Vesuvius in 79 AD (phonolite), Laacher See in 12900 BP (phonolite), and El Chichon in 1982 (trachyandesite) (Self *et al.*, 1984; Schmincke *et al.*, 1999; Harms and Schmincke, 2000). Investigation of sulfur behavior in less evolved alkaline magmas such as those erupting at Nyamuragira could illuminate the origin of volatiles released by these eruptions, several of which have been linked to global climate variations. Furthermore, ascertaining the connection between melt inclusion S concentrations and S emissions in alkaline magmas is important when evaluating whether melt inclusions are accurately describing the S release, as they do for many tholeiitic basaltic eruptions.

Previous studies of Nyamuragira volcanic products have focused on the physical, major and trace element, and isotope characteristics of lavas and tephras (Denaeyer, 1969; Pouclet, 1975; Kampunzu *et al.*, 1984; Aoki *et al.*, 1985; Hayashi *et al.*, 1992; Chakrabarti *et al.*, 2009a). Volatile studies of Nyamuragira magmas, on the other hand, are currently lacking. Here we present new volatile (H_2O, CO_2, S, Cl, F) and major element data from olivine-hosted melt inclusions from six Nyamuragira lava and tephra samples from five historic eruptions (1912, 1938, 1939, 1986, and 2006). These results are then compared to SO_2 emissions derived from TOMS and OMI data. Given the significance of Nyamuragira to present day global volcanic gas emissions, it is important to understand the role of volatiles in Nyamuragira's eruptions. Our work constitutes the first reported analysis of melt inclusions in magmas from an active segment of the East African Rift (EARS) system; the only other similar study know to us reported preliminary data from Turkana (Waters *et al.*, 2004).

3.2 Geologic setting and eruption characteristics

The first volcanic activity associated with the East African Rift occurred 45 Ma in Ethiopia and propagated south to Kenya, where the rift split around the Tanzanian craton into eastern and western branches (George *et al.*, 1998). Volcanism in the western branch began 11 Ma and its eruptive products are less voluminous, more potassic, and silica-undersaturated compared to those from the eastern branch (Kampunzu *et al.*, 1998; Furman and Graham, 1999; Furman, 2007). The western branch spans ~750 miles between Lakes Albert and Malawi and can be broken up into four volcanic regions from north to south: 1) Toro-Ankole in western Uganda, 2) Virunga and 3) Kivu spanning the D.R. Congo, Rwanda, Burundi, and southern Uganda, and 4) the Rungwe in southern Tanzania (Ebinger, 1989; Furman, 1995; Rogers *et al.*, 1998; Kampunzu *et al.*, 1998; Furman and Graham, 1999; Spath *et al.*, 2001; Ebinger and Furman, 2002; George and Rogers, 2002; Furman *et al.*, 2004).

Nyamuragira and its neighboring volcano, Nyiragongo, are currently the only active volcanoes in the western branch and are part of the Virunga volcanic chain. The less active volcanoes within this chain are, from northeast to southwest, Muhavura, Sabinyo, Visoke, Karisimbi, and Mikeno (Figure 3.1), with the last eruptive activity from Visoke in 1957. Nyamuragira, Muhavura, Karisimbi, and Mikeno have erupted similar lava compositions consisting of K-basanites with evolved derivatives (Rogers *et al.*, 1998). In contrast, Sabinyo has erupted silica-rich lavas (K-trachytes and latites), which are suggested to have evolved from K-basanites through crustal mixing (Rogers *et al.*, 1998). Nyiragongo produces more extreme compositions of leucite-bearing nephelinites and melilitites (Platz *et al.*, 2004). Using both Nd-Sr-Pb and ^{238}U-^{230}Th-^{226}Ra-^{120}Pb isotopic data from Nyiragongo lavas, Chakrabarti *et al.* (2009a,b) suggested that Nyiragongo magmas are generated at greater mantle depths and lower degrees of partial melting than Nyamuragira. The last flank eruption from Nyiragongo occurred in 2002, and a lava lake now occupies its summit crater (Tedesco *et al.*, 2007).

Volcanism at Nyamuragira since 1948 has been dominated by episodic flank effusive eruptions with intervals of summit lava lake activity (Hamaguchi and Zana, 1983). Twenty-six eruptions have occurred over the last 62 years with an average inter-eruptive repose period of ~3 years since 1980 (Burt *et al.*, 1994). Activity typically begins with fire fountains ~200 m in height from one or more fissure vents, and most of the lava volume is issued in the early stage of the eruption. Hawaiian-type fire fountaining often changes to Strombolian-type activity later in the eruption (Ueki, 1983; Smithsonian Institution, 1971-2010). Vents for Nyamuragira flank eruptions tend to cluster along a major line of weakness, which extends from the summit caldera (Figure 3.1). Since 1996, most eruptions have originated from this NW-SE rift zone that has been shown to align with the axis of maximum extensional strain in the region (Pouclet and Villeneuve, 1972; Kasahara, 1983; Zana, 1983; Chorowicz *et al.*, 1987). Geophysical data (seismicity and tilt) have been used to infer the existence of a magma chamber at a depth of ~3-7 km beneath Nyamuragira (Hamaguchi, 1983). An aseismic zone was found between clusters of short-period

earthquakes at 0-3 km depths and long-period earthquakes at 7-16 km depths. Modeling of benchmark and tiltmeter data corroborate the location and depth of this aseismic zone, which is considered to be Nyamuragira's magma reservoir (Hamaguchi, 1983; Kasahara, 1983).

3.3 Analytical techniques

Major and trace element whole rock compositions of Nyamuragira lava samples (1912, 1938, and 1948 eruptions), tephra samples (1986 and 2006 eruptions), and a 2006 bomb sample were determined by X-Ray Fluorescence (XRF) and Inductively Coupled Plasma-Mass Spectrometry (ICP-MS) at the GeoAnalytical Laboratory at Washington State University (Appendix C).

Lava and tephra samples (Figure 3.1) were crushed, sieved, and handpicked for olivine crystals. The olivines were placed in ethanol and then examined under a binocular microscope to identify suitable melt inclusions. All olivine-hosted melt inclusions from the lava samples were devitrified, with the exception of one naturally glassy inclusion in the 1912 sample. The 1986 and 2006 tephra samples contained naturally glassy melt inclusions, but nothing suitable was found in the 2006 bomb sample. A total of 34 inclusions ranging in size from ~15 to 150 μm were selected for study, and 11 out of the 34 contained spherical vapor bubbles with diameters between 6 and 33 μm. An effort was made to select only melt inclusions that were fully enclosed within the olivine to minimize selection of inclusions affected by late-stage volatile loss.

Although the lava flow samples contained abundant olivine and pyroxene crystals, most melt inclusions were devitrified (crystalline) and, therefore, these inclusions were rehomogenized following the approach described in Roedder (1979, 1984) and Danyushevsky *et al.* (2002). We recognize that both the crystallization process and the re-homogenization processes have the potential to modify volatile composition.

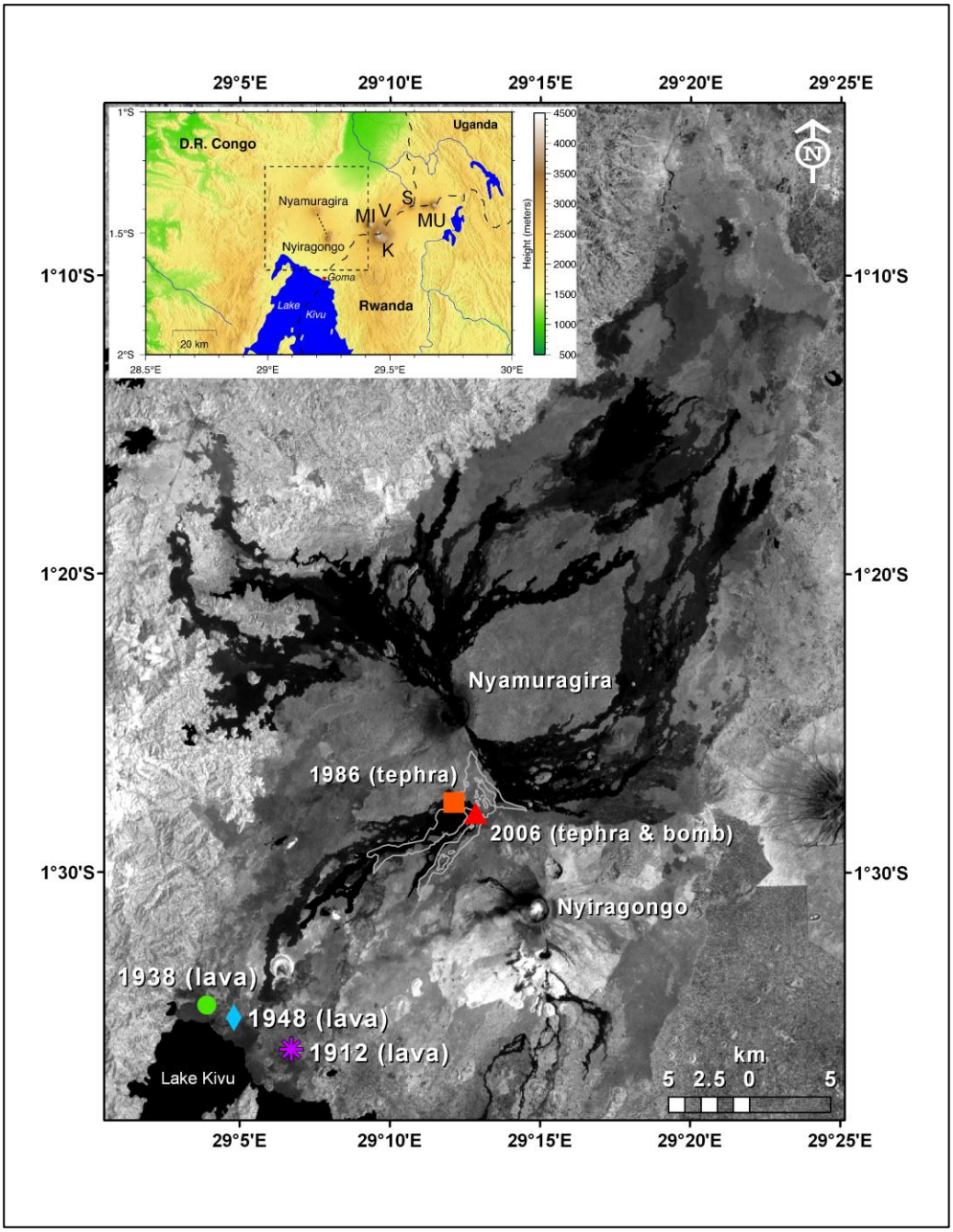

Figure 3.1 Location of Nyamuragira (D.R. Congo) within the western branch of the East African Rift near the Rwandan border. Sample locations are marked by eruption year and symbols correspond to the data presented in all figures. The base map is a Landsat image (http://glovis.usgs.gov/) acquired on 21 February 2005 with the 2006 and an outline of the 2010 lava flows superimposed (from Head *et al.*, *in press*). The inset SRTM image (http://earthexplorer.usgs.gov/) shows the locations of volcanoes within the Virunga chain: Mu- Muhavura, S- Sabinyo, V- Visoke, Mi- Mikeno, and K- Karisimbi, as well as the NNW-SSE rift zone (dotted line), which has been linked to regional tectonic stresses. Nyamuragira eruptions since 1996 have occurred along this zone.

Rehomogenization can result in H_2O loss due to H diffusion upon reheating (e.g., Massare *et al.*, 2002). However, we used temperatures ≤ 1200 ˚C and the samples were reheated for ≤ 15 minutes. These time constraints during reheating experiments have been shown to minimize H_2O-loss considerably (Sobolev *et al.*, 1983; Danyushevsky *et al.*, 2002; Rowe *et al.*, 2007) (see discussion in section 3.5.2).

To estimate crystallization temperatures (maximum temperature of heating) for the re-homogenization experiments, we used the major element composition of representative olivines from each lava flow sample and the geothermometer of Roeder and Emslie (1970). Olivines from each sample were heated to the estimated crystallization temperature (1150-1200°C) in a Deltech furnace with oxygen fugacity maintained at FMQ (fayalite-magnetite-quartz buffer) for no longer than 15 minutes following Rowe *et al.* (2007). The olivines were then released into a beaker of water to quench the inclusions. Only melt inclusions from the 1912 sample did not appear to revitrify after heating and quenching, perhaps because of an inaccurate crystallization temperature estimate.

Naturally glassy melt inclusions from the 1986 and 2006 tephra samples, as well as reheated 1938 and 1948 inclusions with ≤50 μm diameters, were prepared for SIMS analyses. Olivines were mounted in epoxy and hand polished to expose the inclusions on one side. The olivines were then removed from epoxy mounts, cleaned, mounted in indium metal, and polished for ion and electron microprobe analyses. The indium-mounted inclusions were then analyzed with the 1280 ion microprobe (H_2O, CO_2, S, Cl, and F) at Woods Hole Oceanographic Institution following methods described in Shaw *et al.* (2010). A 15-20 μm rastered spot was measured with a 1-2 nA Cs^+ beam. Combined accuracy and precision is ~10% (2σ) and detection limits for H_2O, CO_2, S, Cl, and F are 100, 8, 8, 2, and 1 ppm, respectively.

A subset of 1938 and 1948 reheated melt inclusions, as well as the 1912 glassy inclusion, were also analyzed for H_2O and CO_2 using infrared (IR) spectroscopy at the University of Oregon. Only inclusions ≥50 μm in diameter were analyzed because analytical uncertainties are much larger for smaller inclusions. Descriptions of sample preparation and analytical methods are given in Vigouroux *et al.* (2008) and Johnson *et al.* (2008). We used Dixon and Pan (1995) to determine the compositionally dependent molar absorption coefficients for the carbonate peaks, and we used an absorption coefficient of 63 L/mol cm for the fundamental O-H stretching vibration (Dixon *et al.*, 1995).

Major and volatile (S, Cl, and F) element compositions of the melt inclusions, tephra glasses, and olivine host crystals were determined using the Cameca SX-100 electron microprobe at the University of Oregon and the JEOL-JXA-733 electron microprobe at the Massachusetts Institute of Technology (MIT) (Appendix D; Appendix E). At the University of Oregon, a 15kV accelerating voltage and a spot size of 20 μm was used. Beam current was 10 nA for Na, Si, K, Al, Mg, Fe, and Ca, and 50 nA for F, S, Cl, Ti, Mn, and P. The counting time was 20 s for Mn, 40 s for K, Ca, F, and Si, 60 s for Mg, Al, and P, 80 s for Na and Ti, 96 s for S, 100 s for Cl, and 120 s for Fe. At MIT, a 15kV accelerating voltage, 10 nA beam intensity, and a spot size of 1-10 μm was used. Counting times were 5 s for Na and 40 s for all other elements. Each olivine grain was measured 3 times at variable distances from the melt inclusion to evaluate the presence of compositional zoning. We found uniform olivine compositions at all distances from the inclusion, suggesting that our olivines are not zoned.

All melt inclusion data were corrected for post-entrapment crystallization (PEC) of olivine along the walls of the inclusion. Equilibrium olivine was added in 0.1 wt% increments to melt inclusion compositions until they were in equilibrium with their host olivine. An Fe-Mg K_d $[(FeO/MgO)_{olivine}/(FeO/MgO)_{melt\ inclusion}]$ of 0.3 was used, and we assumed that 30% of the total Fe was present as Fe^{3+}. On average, 8% or less olivine was added back to the 1986 and 2006 tephra samples. For the rehomogenized samples, however, a range of -11%

to 11% olivine was added (Appendix C). Negative values indicate that the olivine was heated to a higher temperature than its trapping temperature during the rehomogenization process or, alternatively, large amounts of cooling between inclusion entrapment and eruption, especially for melt inclusions in high-Fo olivine, could have occurred (Danyushevsky *et al.*, 2000; Johnson *et al.*, 2010). We also corrected 9 inclusions for shrinkage bubble formation to determine the amount of gas present in the bubble (see Shaw *et al.*, 2008). Through this process, H_2O and CO_2 are added back to the mass of the inclusion. In all cases, this correction resulted in a <0.01 wt% change in water concentrations. Carbon dioxide corrections, on the other hand, resulted in an 11-46% change between the original and corrected values.

3.4 Results

3.4.1 Major and Minor Element Chemistry

The Virunga volcanoes have produced lava compositions ranging from melilitites to basanites to trachyandesites. Based on major element melt inclusion and whole rock compositions (Appendix C; Appendix D), our Nyamuragira samples fall within the basanite-tephrite and alkali basalt fields on the total alkali vs. silica diagram, and are within the range of whole rock compositions previously determined (e.g., Aoki and Yoshida, 1983; Aoki *et al.*, 1985; Hayashi *et al.*, 1992). The major element chemistry of melt inclusions can be used for evaluating processes that influence inclusion composition, such as variations caused by pre-entrapment and post-entrapment crystallization.

Our data show that most melt inclusions are more primitive than whole rock samples (Figure 3.2a), and the variations in melt inclusion compositions suggest fractional crystallization of olivine and potentially pyroxene. Aoki *et al.* (1985) attributed Nyamuragira whole rock major element variations to the fractionation of 30-40% olivine, clinopyroxene, plagioclase, and magnetite using a least-squares mixing model. They determined that olivine was the first phase to crystallize and, therefore, we chose olivine-

hosted melt inclusions to increase the likelihood of sampling primitive melt compositions. Within our dataset, the highest MgO concentration (13 wt%) was found in the 1912 melt inclusion. However, the 1912 inclusion has similar K_2O and higher P_2O_5 concentrations compared to the more evolved 1986 and 2006 inclusions, suggesting that the 1912 inclusion does not represent a parental composition for the more evolved magmas. In addition, the 1912 inclusion has significantly higher S and Cl but lower F than most of the other inclusions, despite the similar K_2O values. These features suggest that the 1912 inclusion was derived from a different mantle source, and it may represent a more volatile-rich magma composition in the Nyamuragira system. The fact that the 1912 Rumoka eruption was unusually explosive compared to other Nyamuragira eruptions also supports a higher volatile concentration in the 1912 magma. The high S content (0.35 wt%), in particular, suggests that some Nyamuragira magmas may initially be very S-rich at depth, as implied by the large SO_2 emissions measured from its eruptions. The Mg# (100 * MgO/ (FeO + MgO)) of host olivines from our dataset range from 71 to 84, and melt inclusions range from Mg# 42 to 61, with the exception of the 1912 inclusion (olivine Mg # = 90; melt inclusion Mg # = 74).

Most corrected melt inclusion FeO_T data fall within a distinct range of values that are similar to whole rock and matrix glass compositions. Deviations from this trend suggest post-entrapment diffusion of Fe and, in fact, 11 out of 34 inclusions have values that indicate potential Fe loss or gain (Figure 3.2b). Data from five 1938 and four 1948 reheated inclusions, and two 1986 naturally glassy inclusions, were significantly above or below the MgO vs. FeO_T range set by the remainder of the melt inclusion data, as well as the matrix glass and the majority of the whole rock data. If a primary (co-entrapped) titanomagnetite crystal had been present within the devitrified inclusions and subsequently melted during reheating, this addition could explain the anomalously high FeO_T data (Rowe *et al.*, 2007). Anomalously low FeO_T in some of the reheated and naturally glassy inclusions, however, suggests that Fe diffused out of the inclusion (Danyushevsky *et al.*, 2000). Gaetani and Watson (2000) have shown that various amounts of Fe and Mg diffusion can occur between

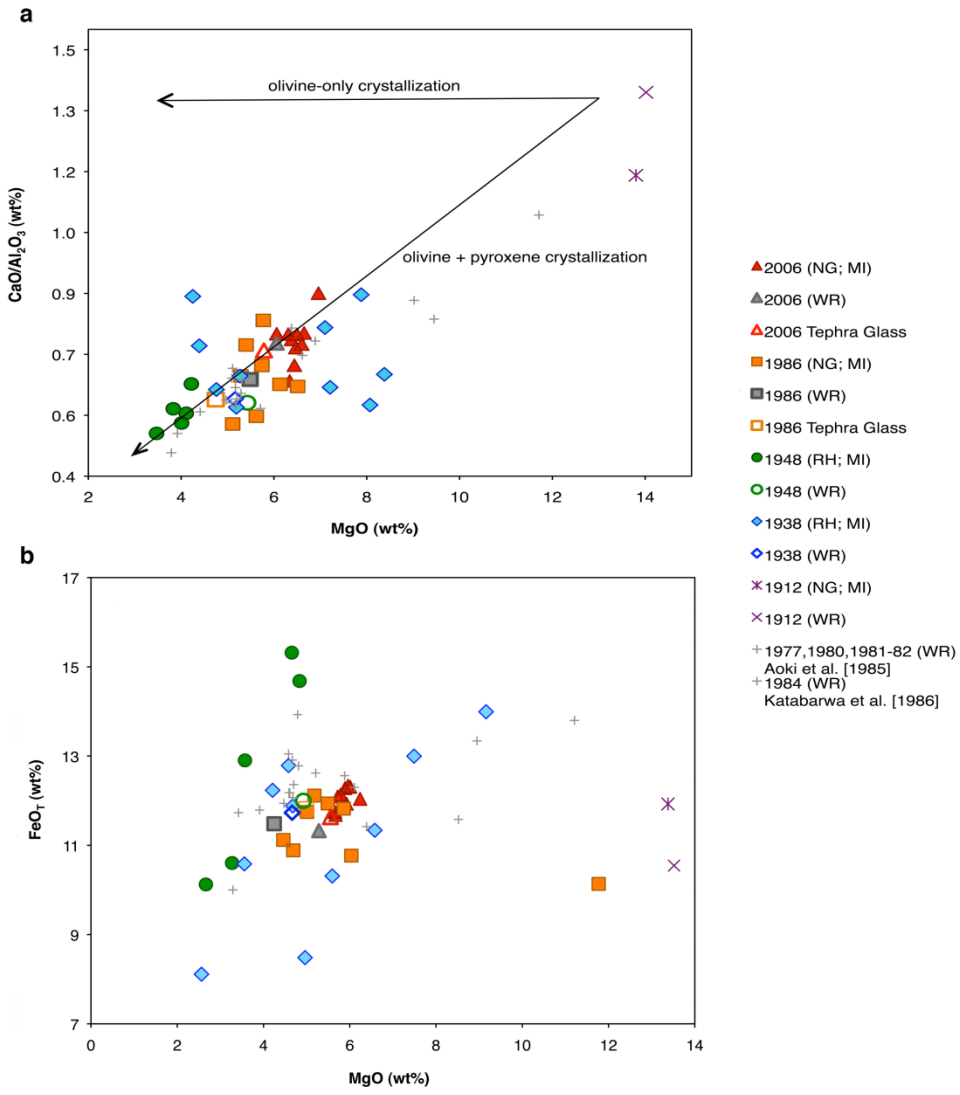

Figure 3.2 For all variations diagrams, melt inclusions are "MI", naturally glassy inclusions are "NG", rehomogenized inclusions are "RH", and whole rock is "WR". The 1984 WR data are from Katabarwa *et al.* (1986) and the 1977, 1980, and 1981-82 WR data are from Aoki *et al.* (1985). (a) MgO vs. CaO/Al_2O_3 data suggest olivine + clinopyroxene crystallization; (b) MgO vs. FeO_T data suggest Fe loss and gain for inclusions with FeO_T concentrations that fell outside the 11-13 wt% FeO_T range set by the majority of our melt inclusion, tephra glass, and whole rock data.

the melt inclusion and the olivine host while the melt inclusion is still within the magma reservoir. We addressed this variation by adjusting the original FeO_T values of the anomalous data points to 12 wt% FeO_T (e.g., Danyushevsky *et al*., 2000; Johnson *et al.*, 2010). This value fell within the range of FeO_T concentrations (11-13 wt%) that defined the majority of our dataset. New PEC corrections were then carried out only for the inclusions that fell outside of the 11-13 wt% FeO_T range.

1.1.1 Melt inclusion volatile concentrations

The naturally glassy melt inclusions from the 1986 and 2006 eruptions generally have the highest H_2O and CO_2 concentrations (Figure 3.3a; Appendix D). H_2O contents of the 1986 and 2006 melt inclusions range from 0.6-1.4 wt %, and CO_2 contents range from 350-1900 ppm. These data are higher than MORB H_2O values (0.1-0.3 wt%), but overlap the typical range for E-MORB values (0.3-1.0 wt%; e.g., Dixon *et al.*, 1995). Our inclusions contain significantly higher CO_2 concentrations than typical MORB (< 350 ppm in both MORB inclusions and glassy pillow rims; e.g., Saal *et al*., 2002; le Roux *et al.,* 2006). The 1912, 1938 and 1948 samples have CO_2 concentrations ranging between 30-1000 ppm, but H_2O contents are significantly lower (0.03-0.4 wt %) than inclusions from the tephra samples. Other than rehomogenization causing potential H_2O loss, the low H_2O concentrations observed in the 1938 and 1948 samples could have resulted from the H diffusion that readily occurs during slow cooling of lava flows (Figure 3.3b; e.g., Hauri, 2002; Metrich and Wallace, 2008).

A high CO_2 content melt inclusion should have lost minimal amounts of S, owing to the lower solubility of CO_2 relative to S. Based on the observation of relatively uniform S concentrations over a range of CO_2 values, we suggest little pre-eruptive S degassing for the 2006 eruption (Figure 3.3c). The primary CO_2 contents of our Nyamuragira magmas are unknown, although there is evidence supporting alkalic magmas being initially CO_2-rich (Spera and Bergman, 1980; Dixon, 1997). Primary CO_2 concentrations in non-alkalic

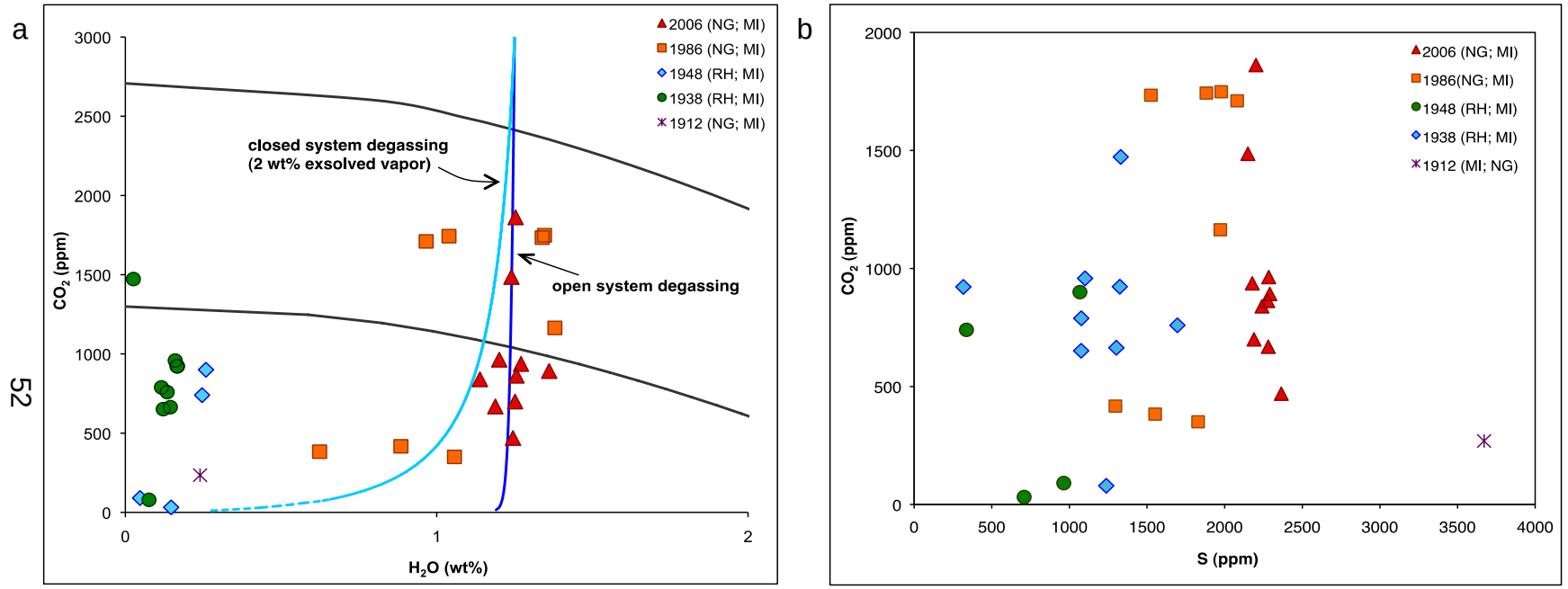

Figure 3.3 (a) Melt inclusion entrapment pressures calculated from Nyamuragira H_2O and CO_2 data allow an assessment of degassing with decompression. Assuming vapor saturation, these entrapment pressures, degassing trends, and isobars were calculated with VolatileCalc (Newman and Lowenstern, 2002). We modeled the degassing trends for the tephra samples only (1986 and 2006) only, due to likely H loss from lava flow samples (1938 and 1948). The 2006 data are best fit by an open system trend, whereas the 1986 data are best fit by a closed system trend with 2% exsolved vapor coexisting in the melt; (b) S vs. CO_2 data suggest little S degassing with ascent; (c, below) K_2O vs. H_2O suggest that some 1986 samples trapped melts degassed of H_2O.

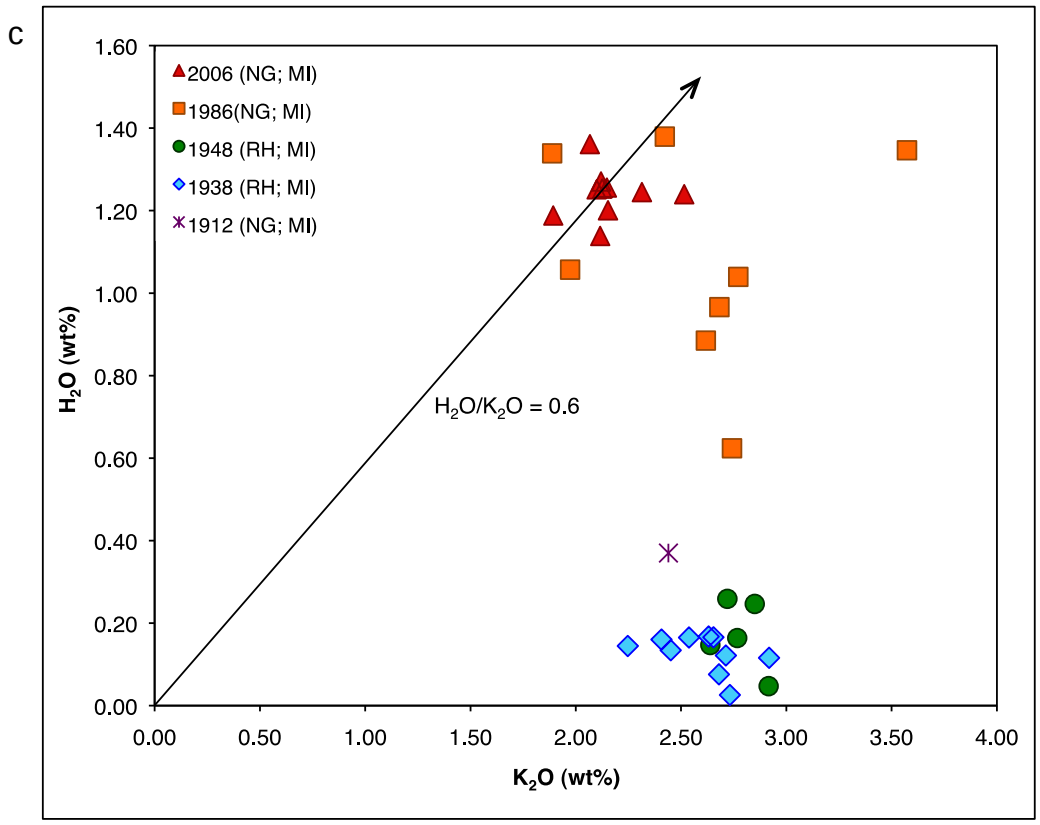

magmas at Kilauea (Hawaii) and the Michoacan-Guanajuato Volcanic Field (Mexico) are estimated to be ~0.6-0.7 wt%; melt inclusions trapped at shallow depths in these systems record significant CO_2 loss at upper crustal pressures (Gerlach and Graeber, 1985; Wallace, 2005; Johnson *et al.*, 2010). If we assume that Nyamuragira magmas start off with a higher CO_2 content than the Kilauea and Michoacan-Guanajuato systems, our data also suggest strong degassing of CO_2 prior to entrapment. In addition to CO_2, degassing of S could have occurred prior to inclusion entrapment as the magma ascended and cooled, particularly for the 1938, 1948, and 1986 inclusions (Figure 3.3c).

Sulfur concentrations of the 2006 sample show little variation (2100-2400 ppm), whereas the 1986 S data show slightly more variability (1300-2000 ppm) and suggest some S loss. A clear degassing pattern in the 1938 and 1948 data is difficult to see due to scatter. The 1938 and 1948 samples with 300-1700 and 300-1000 ppm S, respectively, also show wider

variation than the 2006 sample. The 1912 melt inclusion has the highest S concentration (~3600 ppm). The range of Nyamuragira S concentrations are comparable to values reported for melt inclusions in other alkaline systems. The Nyamuragira data lie between Etna (alkali basalt), Kilauea (alkali basalt), Vulcano (shoshonitic basalt), and Mt. Cameroon (basanite) samples, which range in S concentration from 1000-3500 ppm (Figure 3.4; Metrich and Clocchiatti, 1996; Spilliaert *et al.*, 2006; Coombs *et al.*, 2006; Suh *et al.*, 2008). Melt inclusions from cinder cones around the flanks of Colima volcano (Mexico;basanite, minette) contain the largest S concentrations (~5000 ppm) reported thus far. In comparison with MORB S concentrations (1300-1700 ppm S; PetDB), the 1938 and 1948 data are low, whereas the 1986 and 2006 data are relatively high, and the 1912 S concentration (3600 ppm) is well above the range of MORB values. Chlorine concentrations (800-1300 ppm) are significantly higher than MORB values (< 150 ppm; Michael and Schilling, 1989), but are within the range of other alkali basalt and basanite values from Italy, Hawaii, Mt. Cameroon, and Mexico (100-2500 ppm; Spilliaert *et al.*, 2006; Coombs *et al.*, 2006; Suh *et al.*, 2008; Vigouroux *et al.*, 2008). Fluorine concentrations (92-2200 ppm) overlap MORB (300-840 ppm; PetDB) and Mt. Cameroon (1530-1982 ppm; basanite; Suh *et al.*, 2008) values. Two exceptions of anomalously low Cl and F values are found in the 1938 and 1948 samples (Appendix D). We note that the 1938 and 1948 samples with the lowest Cl and F also have the lowest S in the dataset, suggesting that these samples may have suffered extensive degassing.

3.5 Discussion

3.5.1 Melt Inclusion Entrapment Depths and Volatile Degassing

The volatile contents of Nyamuragira melt inclusions suggest that the melts have undergone variable extents of degassing. Interpreting this variation requires an assessment of the magmatic processes that occur throughout magma storage, ascent, and eruption. As magma ascends, decompression can induce both degassing and crystallization (e.g., Sisson

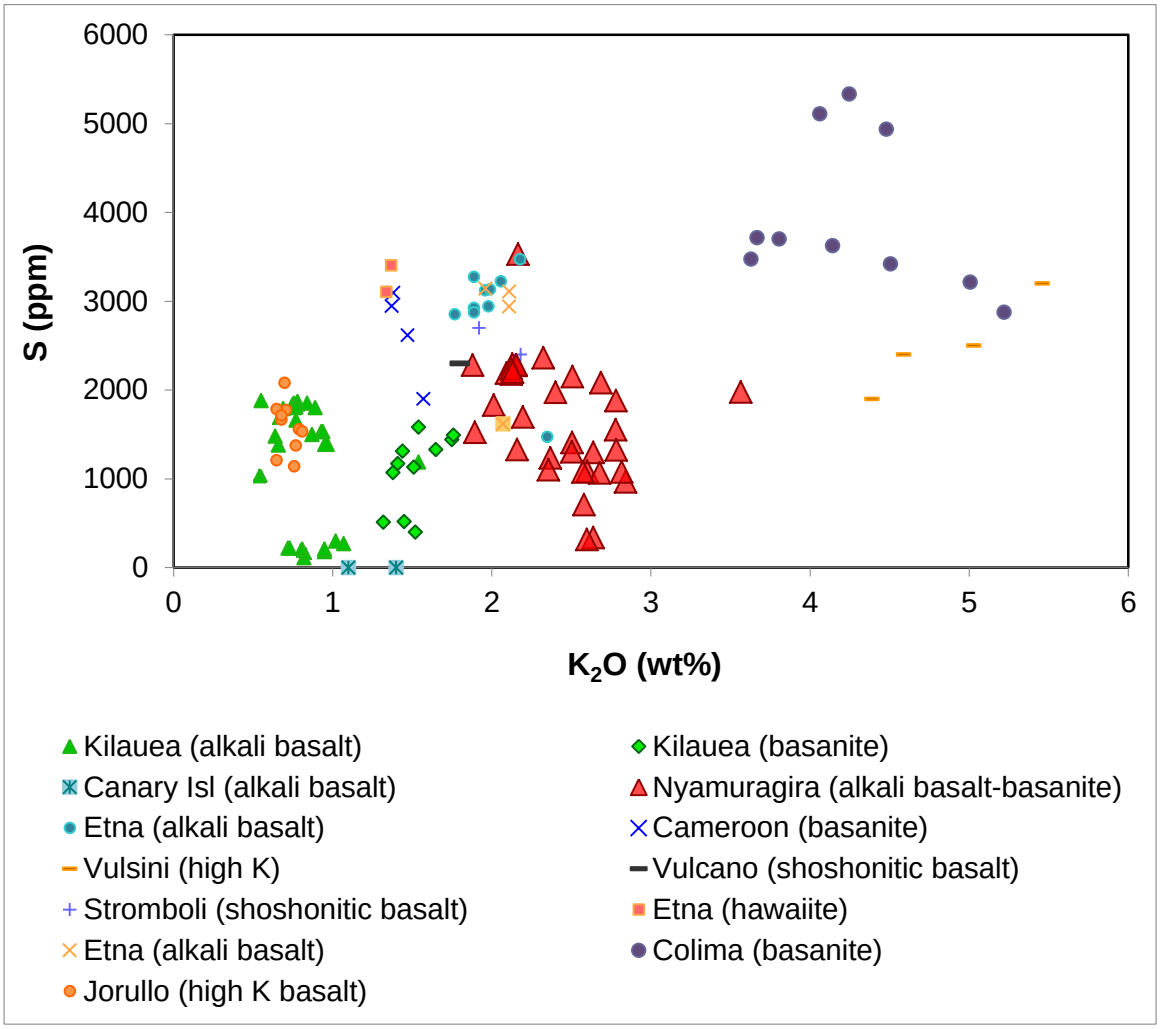

Figure 3.4 K_2O vs. S for Nyamuragira melt inclusion data, along with global S melt inclusion data from: Vigouroux *et al.*, (2008) (Colima); Spilliaert *et al.*, (2006) (Etna); Johnson *et al.*, (2008) (Jorullo); Coombs *et al.*, (2006) (Kilauea); Metrich *et al.*, (2004) (Etna); Suh *et al.*, (2008) (Cameroon); Gurenko *et al.*, (2001) (Canary Islands); Metrich and Clocchiatti (1996) (Vulsini; Volcano and Stromboli; Etna).

and Layne, 1993; Roggensack, 2001; Couch *et al.*, 2003; Blundy and Cashman, 2005). The following discussion will consider the degassing history of melts from Nyamuragira, focusing primarily on naturally glassy (rather than re-homogenized) melt inclusions from the 1912, 1986, and 2006 eruptions. We consider these samples to best represent pre-

eruptive Nyamuragira magma compositions and hence we use them to estimate syn-eruptive SO_2 degassing for comparison with satellite-based SO_2 measurements.

Estimates of melt inclusion entrapment depths using H_2O and CO_2 data allow crystallization and degassing to be placed within the context of magma ascent and storage. Water and CO_2 concentrations can be used to infer the depth at which melt inclusions are trapped based on experimentally-determined solubility relationships and assuming that the melts were vapor saturated when they were trapped. Entrapment pressures (Appendix D) and degassing paths are calculated using VolatileCalc (Newman and Lowenstern, 2002) (Figure 3.3a).

The 1986 and 2006 melt inclusion data indicate entrapment over a range of pressures from 1-~1.7 kb (~3-5 km). This is consistent with magma chamber depth estimates inferred from seismic investigations, which range from 3 – 7 km (Hamaguchi, 1983). The 2006 data define a trend that is best explained by open system degassing, whereby volatiles can escape from the melt after exsolution. The 1986 data show more scatter and do not define any coherent degassing path. Some of the variation could be explained by closed system degassing with excess exsolved gas (see Figure 3.3a), but other more complex processes like open system gas fluxing (e.g., Spilliaert *et al.*, 2006; Johnson *et al.*, 2008) could also account for the scatter. For both the 1986 and 2006 eruptions, we used the highest H_2O and CO_2 values in the dataset (presumably the deepest melts) to represent initial magma compositions. The 2006 data suggest that, as the magma decompresses over the ~3-5 km depth range, CO_2 exsolves while H_2O remains dissolved in the melt. Our data agree well with modeling studies for alkalic systems, which show that CO_2 exsolves at depths ranging from ~3-6 km while H_2O does not exsolve until ~1 km depth (Dixon, 1997).

Wallace and Anderson (1998) evaluated melt inclusion H_2O and K_2O data to assess the effects of magma degassing on melt inclusion compositions prior to entrapment. On a plot of K_2O vs. H_2O, an H_2O/K_2O ratio (1.3) was established from the least degassed data, and

all data below this line were interpreted as having degassed variable amounts of H_2O. For our samples, if we assume a constant H_2O/K_2O ratio (0.6) for the initial undegassed magma (based on a line projected from the origin to the highest H_2O values in our dataset), the 1986 and 2006 data points that fall below this line are likely to have undergone H_2O degassing prior to entrapment (Figure 3.3c). The low H_2O data from the reheated inclusions are, as discussed above, likely due to either H-loss by diffusion in the lava or possibly by the reheating process itself.

From S, Cl, and F concentrations plotted against Mg# (Figure 3.5), we find that the single 1912 inclusion is exceptionally primitive and S and Cl rich, whereas the 1986 and 2006 inclusions are more evolved but still relatively undegassed compared to the 1938 and 1948 samples. Sulfur concentrations decrease with decreasing Mg# for the 1938, 1948, and 1986 eruptions (Figure 3.5a). This trend is consistent with simultaneous fractional crystallization and degassing. Excluding the 1912 inclusion, Cl and F data neither decrease nor increase with decreasing Mg# (Figure 3.5b and c, respectively). Furthermore, residual Cl and F measured in the tephra glasses (800 and 1300 ppm, respectively, for the 2006 sample and 900 and 1700 ppm, respectively, for the 1986 sample) support the assumption that Cl and F do not degas significantly prior to or even during eruption. The 1912 sample has lower F and CO_2 concentrations than the rest of the dataset.

3.5.2 Sulfur Solubility in Nyamuragira Magma

In order to make robust estimates of primary melt S concentrations, we need to evaluate S solubility and determine whether Nyamuragira melts have been influenced by variable oxidation conditions. More specifically, could primary Nyamuragira magmas contain enough S to account for what is observed in SO_2 emissions? Sulfur concentrations measured in MORB glasses are typically controlled by immiscible sulfide liquid saturation (Mathez, 1976; Wallace and Carmichael, 1992). The positive correlation between FeO_T and S in basaltic glasses with relatively low oxygen fugacities is caused by the effect of FeO on

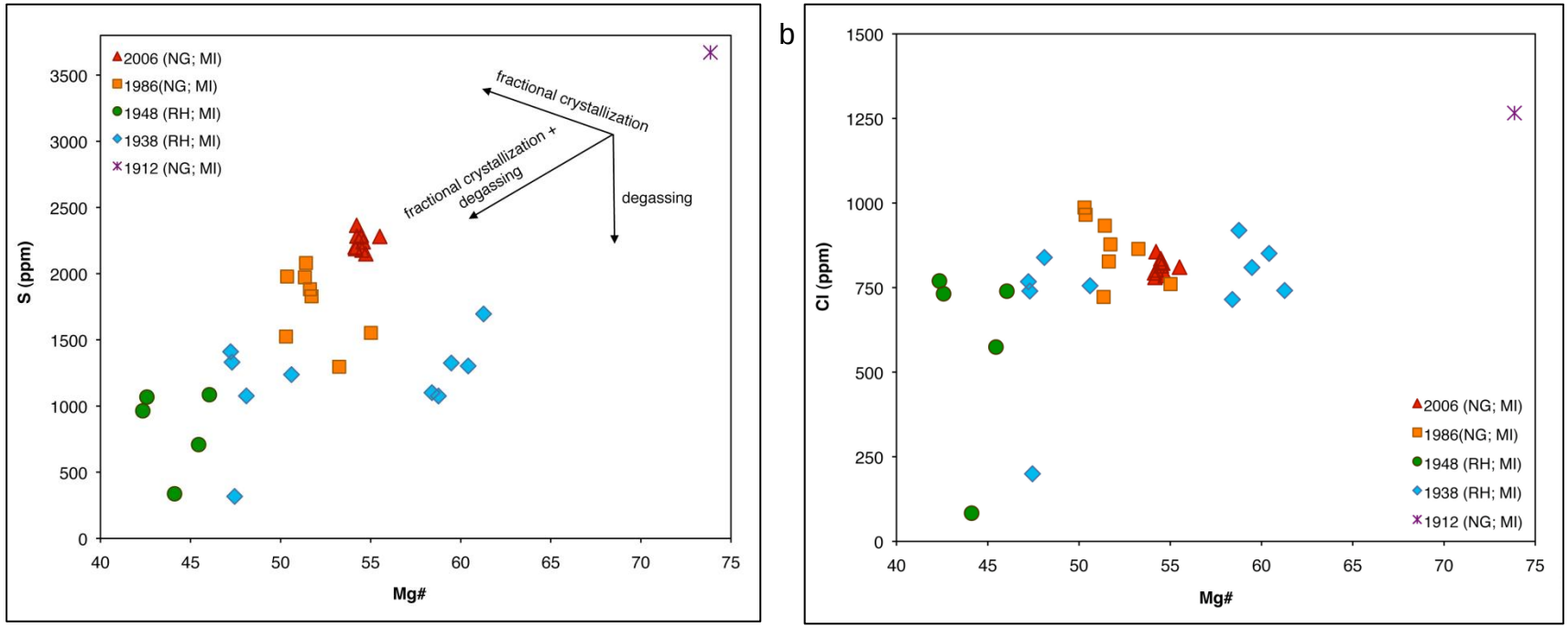

Figure 3.5 (a) S vs. Mg#; (b) Cl vs. Mg#; (c, below) F vs. Mg#. The 1912 inclusion is exceptionally primitive and S and Cl rich, whereas the 1986 and 2006 inclusions are more evolved but still relatively undegassed compared to the 1938 and 1948 samples. The S vs. Mg# trend is consistent with simultaneous fractional crystallization and degassing. Cl and F neither decrease nor increase with decreasing Mg# and residual Cl and F measured in the tephra glasses (800 and 1300 ppm, respectively, for the 2006 sample and 900 and 1700 ppm, respectively, for the 1986 sample) suggest that Cl and F do not degas significantly prior to or even during eruption.

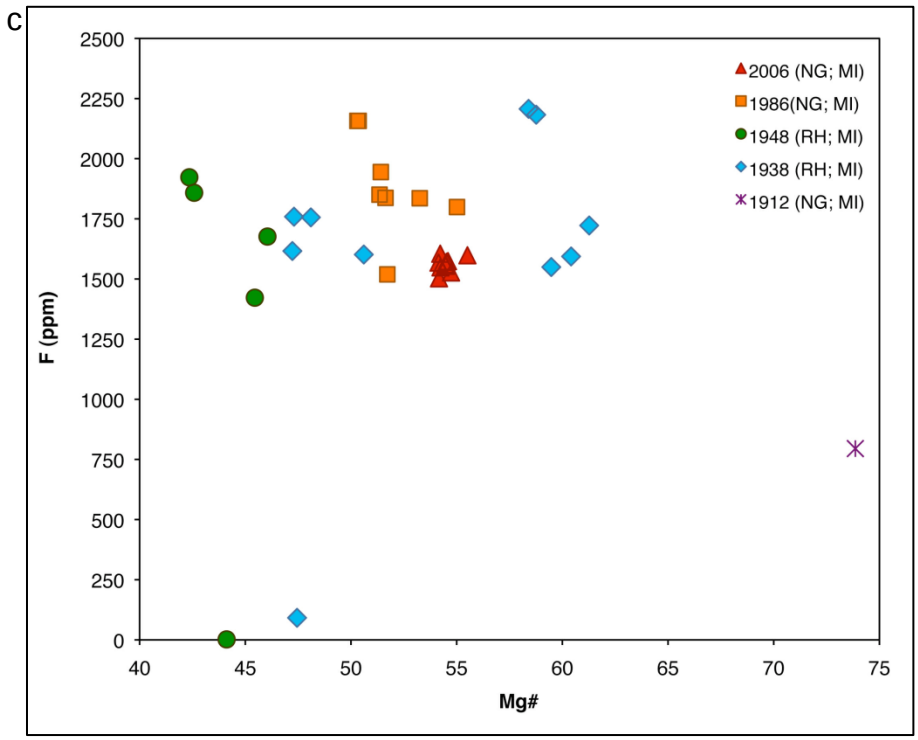

S solubility. In contrast, magmas that have oxygen fugacities higher than NNO contain a substantial proportion of sulfate, which makes the total S solubility much higher than for MORB (e.g., Metrich and Wallace, 2008). Some of our Nyamuragira data fall within the range of MORB values that are controlled by this sulfide-saturation field, with other points plotting both below and above the field (Figure 3.6). Thermodynamic modeling as described in Wallace and Carmichael (1992) can be used to estimate S solubilities at fO_2 <NNO and 1150˚C for Nyamuragira magmas (Figure 3.6). The results require that Nyamuragira data lying above the NNO solubility curve represent inclusions with fO_2 values that were higher than NNO, whereas lower values may represent melts that originally contained a higher S concentration but have degassed S prior to inclusion entrapment. An interesting outlier in our data is the 1912 inclusion, which has significantly higher S than the rest of the data set for a given FeO_T. We cannot draw solid conclusions with this one data point, but it suggests that magma with even higher fO_2 may exist in the Nyamuragira system. Our S data indicate that Nyamuragira magmas commonly have a

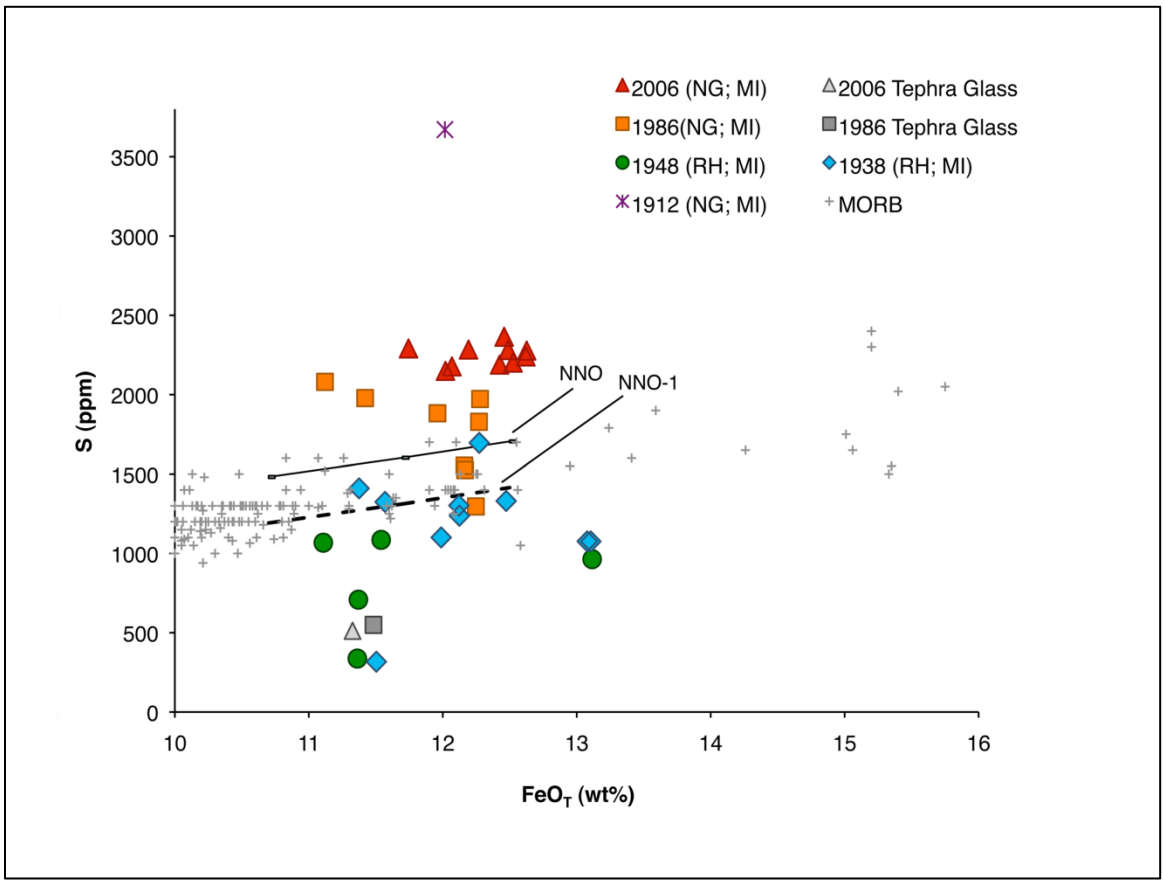

Figure 3.6 S vs. FeO_T data for Nyamuragira melt inclusions and tephra glasses compared to MORB glasses. The relatively high S contents of some Nyamuragira melt inclusions require fO_2 values >NNO. The NNO and NNO^{-1} lines were calculated using the method of Wallace and Carmichael (1992), modified to incorporate the temperature dependence of Mavrogenes and O'Neill (1999), for Nyamuragira magmas with a range of FeO_T contents (11-13 wt%) at 1150˚C and NNO. The S solubility model is not calibrated for fO_2 higher than NNO.

higher fO_2 than NNO, resulting in relatively high initial S contents.

3.6 Comparison between satellite-based SO_2 emissions, lava volumes, and estimated SO_2 emissions from melt inclusion data

Nyamuragira emits large amounts of SO_2 (up to 1.7 Mt/day; 1981 eruption) compared to both arc and non-arc volcanic eruptions (Figure 3.7), but the source of the SO_2 emissions (e.g., syn-eruptive S release from melt or release of a pre-eruptive vapor phase) and the

mechanisms of S release during eruptions are poorly understood. An important aim of our study, therefore, is to compare Nyamuragira SO_2 emission estimates based on satellite data (TOMS and OMI measurements) to estimates of SO_2 released based on melt inclusion data and lava flow volume estimates (Figure 3.7). We estimated the total amount of SO_2 released from Nyamuragira for the 1986 and 2006 events using the petrologic method, whereby S contents in melt inclusions are scaled to erupted lava volumes. Lava volumes were calculated using satellite-based lava flow maps and published lava flow thicknesses (1986 = 0.063 km^3; 2006 = 0.070 km^3; Head *et al., in press*). The resulting petrologic estimates are 0.04 Mt SO_2 for the 1986 eruption and 0.06 Mt SO_2 for the 2006 eruption. These results are significantly smaller than the SO_2 emissions measured through satellite-based methods for the same eruptions (~1 Mt for 1986 (Bluth and Carn, 2008) and ~2 Mt for 2006). Measured SO_2 emissions for a number of recent Nyamuragira eruptions (1980-2006) compared to petrologic estimates based on the melt inclusion data further illustrate this point (Figure 3.8). Errors associated with the satellite measurements are ± 30% and the petrologic method has a combined error (melt inclusion S measurements and lava volume calculations) of ± 22%.

Using the highest melt inclusion S concentration we measured (3600 ppm; 1912) still does not resolve the discrepancy, as the satellite-based SO_2 measurements require as much as 5000 ppm S or more to explain the SO_2 emissions by syn-eruptive degassing. Although magmatic S concentrations up to 5000 ppm have been measured in melt inclusions from potassic magmas on the flanks of Colima volcano (Mexico; Vigouroux *et al.*, 2008), there is no evidence in the Nyamuragira melt inclusions that such high concentrations are present in primitive melts.

3.6.1 Degassing Mechanisms at Nyamuragira

The origin of excess S emissions at Nyamuragira can be assessed through the examination of degassing mechanisms. As the degassing process can strongly influence eruption style,

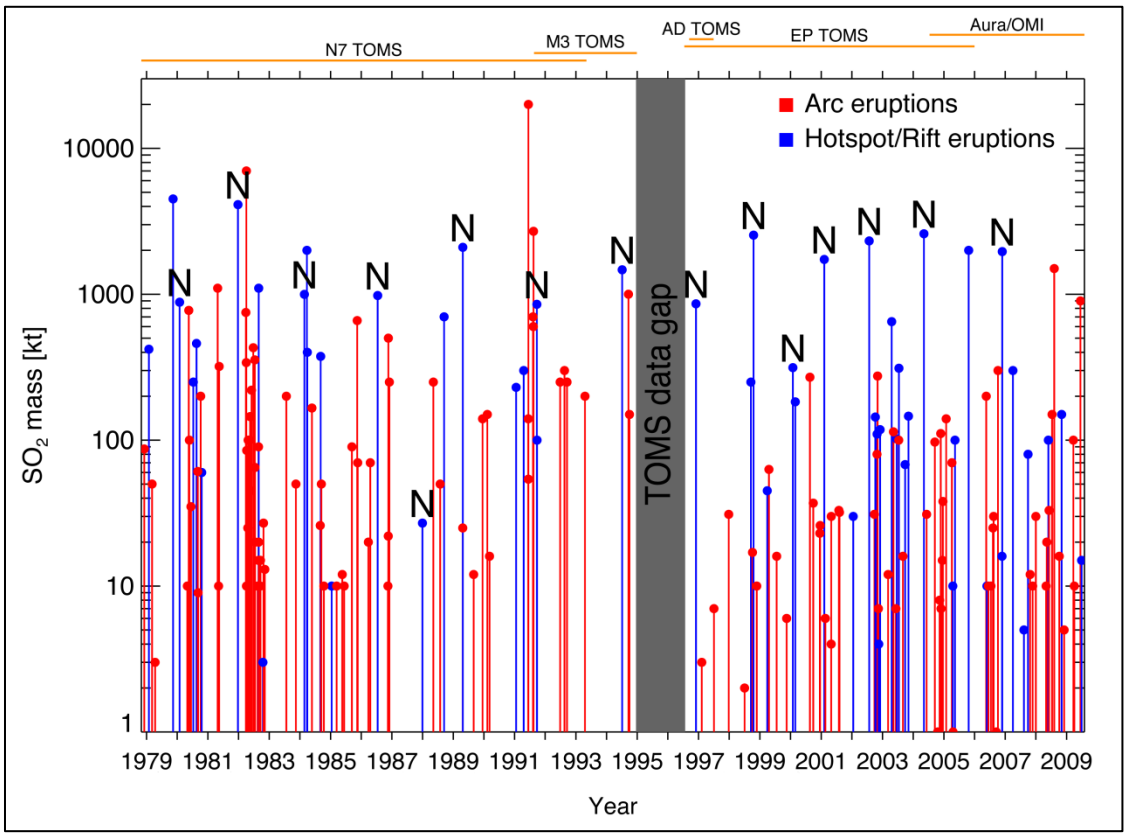

Figure 3.7 Global volcanic SO_2 emissions (kt) measured by the Total Ozone Mapping Spectrometer (TOMS) sensors and the Ozone Monitoring Instrument (OMI) since 1978. The blue lines represent individual non-arc eruptions and the red lines represent individual arc eruptions that detected by TOMS and/or OMI. Nyamuragira eruptions are labeled with an "N". Since 1980, Nyamuragira has been one of the most prolific sources of volcanic SO_2. (Image courtesy of Simon Carn.)

we summarize Nyamuragira's recent eruptive activity and then evaluate two different degassing models that are consistent with our observations. Nyamuragira eruptions typically begin with fire fountaining, a gas-rich jet that propels hot lava from the vent(s) to heights of several hundred meters (Swanson *et al.*, 1979). This eruption style was first documented at Kilauea (Hawaii) and is, therefore, often termed "Hawaiian". Initial fountain heights at Nyamuragira are ~200 m and, as eruptions progress, these fountain heights diminish until the end of the eruption; during the fire fountaining phases SO_2

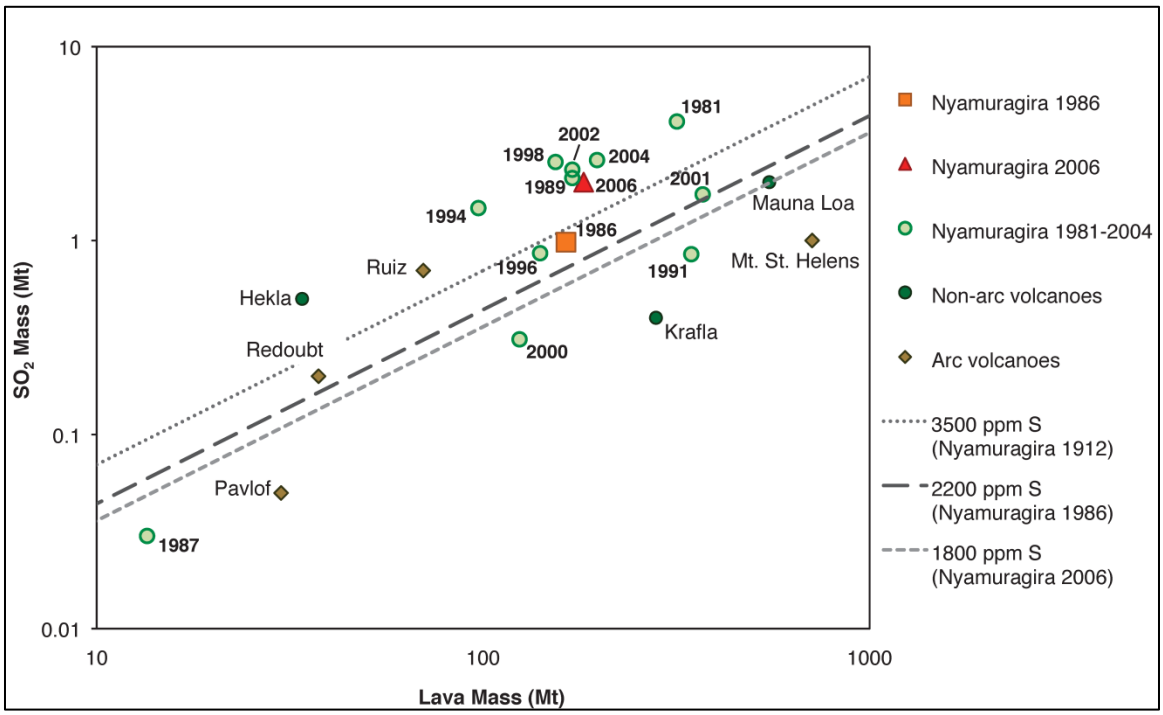

Figure 3.8 Lava and SO_2 mass (Mt) measured by satellite remote sensing methods. The diagonal lines show the amounts of SO2 released by syn-eruptive degassing based on concentrations of S we measured in melt inclusions from the 1912, 1986 and 2006 samples. The 1986 and 2006 eruptions are the only Nyamuragira eruptions with both melt inclusion volatile data and remotely sensed SO_2 measurements available. The satellite SO_2 measurements for the 1986 and 2006 eruptions lie above the lines representing the highest S concentrations, which imply that a mechanism other than syn-eruptive degassing occurred for both eruptions. Other Nyamuragira eruptions for which we have SO_2 emission estimates also plot above the highest measured S concentrations.

emissions also start high and wane as the eruption proceeds (Bluth and Carn, 2008). During the middle to late phase of some eruptions, renewed fire fountaining occurs, although fountain heights are reduced compared to the initial activity, and/or Strombolian-style eruptions are observed (Smithsonian Institution, 1971-2010), consisting of large gas slugs bursting at the vent (Wilson, 1980).

For the 2006 Nyamuragira eruption, initial fire fountain heights were over 300 m, whereas the 1986 fire fountains reached a maximum height of 200-250 m (Smithsonian Institution,

1971-2011). Satellite-based SO_2 emissions associate with the 2006 eruption (~2 Mt) are significantly larger than those of the 1986 eruption (~1 Mt), and there is a larger excess S component observed for the 2006 eruption compared to the 1986 eruption. The gas plume associated with the 2006 eruption plume reached the tropopause and could be tracked for almost a week by satellites, whereas maximum plume altitudes during the 1986 eruption were ~9 km (Bluth and Carn, 2008). Higher fire fountain and plume heights, along with larger SO_2 emissions suggests that the 2006 eruption was more energetic than the 1986 eruption (Wilson, 1980; Wilson and Head, 1981; Parfitt and Wilson, 1999).

Two models of degassing can be considered to explain the eruptive behavior at Nyamuragira. Firstly, the collapsing foam model (CF; Vergniolle and Jaupart, 1990) where degassing of basaltic magma results in exsolved gas bubbles rising to the roof of a reservoir, creating a foam layer. When this foam layer reaches a critical thickness, it collapses and eruption occurs. If the collapse is instantaneous, Hawaiian-style activity results; but if there is sufficient time for bubbles to coalescence within the foam, a Strombolian eruption results. Secondly, the rise speed dependent model (RSD; Wilson, 1980; Wilson and Head, 1981) where the speed at which magma ascends controls the style of eruption instead of a foam collapse. If the rise speed is high, the bubbles move with the magma, allowing a homogeneous two-phase flow until fragmentation at the surface (i.e., Hawaiian-style eruption). A slower magma rise speed would allow the bubbles to rise faster than the magma and coalesce, creating a Strombolian eruption. A decrease in gas content would not cause the style to change from Hawaiian to Strombolian, as has been postulated for the CF model. Instead, a decrease in gas content with similar rise speeds would produce an effusive lava flow regime, which has been observed at basaltic volcanoes such as Kilauea and Nyamuragira.

In the first case, we determine whether the accumulation of a foam layer is possible at Nyamuragira. Based on gas solubility behavior for alkaline magmas, both CO_2 and H_2O would have degassed to some extent during ascent to the magma reservoir at 3-7 km

(Dixon, 1997). Our 1986 and 2006 melt inclusion data show that this degassing continued in the magma chamber along with fractional crystallization. Hence, accumulation of exsolved volatiles could have occurred in the magma reservoir prior to eruption. We suggest that a foam layer is plausible and that the CF model could explain fragmentation processes (eruption styles) associated with Nyamuragira degassing and the large excess SO_2 emissions during the fire fountain phases. In the second case, the RSD model could also explain the Hawaiian fire fountaining, Strombolian activity, and transitions between the two styles observed at Nyamuragira. As evidenced by our melt inclusion data, the 2006 magma did not contain significantly higher volatile concentrations than the 1986 magma, although we recognize that variable extents of degassing could have occurred prior to melt inclusion entrapment for either eruption. However, if both magmas had the same initial gas content, an explanation for the more energetic 2006 eruption, as well as the style transitions for both eruptions, could lie in differences in magma rise speeds rather than accumulation and collapse of a foam. A difference in the timescales of gas accumulation might have also influenced the eruption styles, although there were similar repose periods prior to the 2006 (29 months) and 1986 (28 months) eruptions.

Both models address the fact that exsolved gas is propelled to the surface, often with little associated erupted magma. Reconciling the large Nyamuragira SO_2 emissions and disproportionate lava volumes, it is possible that some magma is degassing but not erupting. This degassed magma would then sink back into the system (Allard *et al.*, 1994; Allard, 1997). We evaluated the amount of unerupted magma that would have to degas in order to explain the apparent excess SO_2 emissions. The 1986 and 2006 eruptions would have required degassing of ~1 km^3 and >2 km^3 of unerupted magma, respectively.

In order to further constrain the application of these models to Nyamuragira activity, additional geochemical datasets are needed. In addition, the role of passive degassing in the system between eruptions is unclear as ground-based measurements at Nyamuragira were

not made due to political unrest. These data would allow a better assessment of the volatile budget at Nyamuragira. Gas composition data from techniques such as ground-based Fourier-Transform IR (FTIR) spectroscopy would be particularly useful for evaluating the degassing mechanisms during eruptions (e.g., Allard *et al.*, 2005; Sawyer *et al.*, 2008). If a foam layer exists at Nyamuragira, the gases would have time to equilibrate with the melt, which would be reflected in volcanic gas ratios. For example, the CO_2/SO_2 and S/Cl ratios from FTIR measurements of fire fountaining from Etna (Italy) were shown to be higher than typical Etnean emissions. The ratios indicated exsolution and storage of CO_2 and SO_2 at depth, suggesting gas accumulation. A lower CO_2/SO_2 ratio would be indicative of syn-eruptive degassing of CO_2 and SO_2 (Allard *et al.*, 2005).

3.7 Conclusions

New volatile data from Nyamuragira melt inclusions indicate inclusion entrapment over a range of pressures (vapor saturation pressures) from <1.0-1.7 kbar (~0.1-5 km), where the greater depths inferred agree with seismically determined estimates of magma storage depth. Nyamuragira melt inclusion volatile contents show evidence of variable extents of shallow degassing, which occurred together with crystallization. The 1986 and 2006 tephra samples yielded volatile concentrations that best represent initial values for Nyamuragira magmas. For the 1986 and 2006 eruptions, S concentrations ranged from 1300-2400 ppm, H_2O from 0.6-1.4 wt%, CO_2 from 350-1900 ppm, Cl from 720-990 ppm, and F from 1500-2200 ppm. The relatively high S contents of some Nyamuragira melt inclusions require higher-fO_2 values (>NNO) than MORB. Based on the melt inclusion data, the total SO_2 emissions for the 1986 and 2006 eruptions that could be produced by syn-eruptive degassing are 0.04 and 0.06 Mt, respectively, which is significantly less than satellite-derived estimates (~1 Mt for 1986 and ~2 Mt for 2006). Even when taking into account errors on the SO_2 emissions and melt inclusion S measurements, the magnitude of this discrepancy suggests an additional source of S for both eruptions. Variable pre-eruption gas loss, as inferred from the melt inclusion data, is consistent with a model of shallow

degassing and gas accumulation, although the rise speed of the magma could also be influencing degassing and eruptive behavior at Nyamuragira. Ground-based gas composition measurements have not been possible to date due to the political climate of the region, but we stress the need for this type of data to further constrain Nyamuragira's degassing mechanisms.

ACKNOWLEDGEMENTS

We dedicate this paper to Jim Luhr, who began this research endeavor with us, contributing greatly until his untimely death just a year into the project. Funding for this work was provided by NSF (grant EAR 0910795 to SAC) and the National Geographic Society (grant 7698-04 to SAC). We are grateful for the assistance of Dario Tedesco, the late Jacques Durieux, the Goma Volcano Observatory staff, and the UNOPS with D.R. Congo fieldwork. We thank John Donovan for assistance with EMPA analysis at UO, Nobu Shimizu and Andrey Gurenko for assistance with SIMS analysis at WHOI, and Nilanjan Chatterjee for assistance with EMPA analysis at MIT. We would also like to thank Tyrone Rooney and an anonymous reviewer for thoughtful reviews that greatly improved the manuscript.

CHAPTER 4: EVALUATING THE DYNAMICS AND FATE OF VOLCANIC SO_2 CLOUDS FROM THE 2006 AND 2010 ERUPTIONS OF NYAMURAGIRA VOLCANO (D.R. CONGO, AFRICA)

4.1 Introduction

Volatiles in magma largely control the style of volcanic eruptions. Once injected into the troposphere or stratosphere, volcanic clouds can oxidize and react with atmospheric constituents, causing local and/or global impacts (Robock 1991; Lacis *et al.*, 1995; Spiro *et al.*, 1992; Hansen *et al.*, 1996). Therefore, it is important to quantify the emitted volcanic gases, to constrain their vertical distribution in the atmosphere, and to track volcanic clouds during atmospheric transport and dispersion. Gases in volcanic clouds can be quantified by either ground-based or satellite-based methods (e.g., Giggenbach, 1975; Krueger, 1983). Ground-based methods, such as fumarolic gas sampling and Fourier-transform infrared (FTIR) spectroscopy, allow the quantification of a number of gas species (FTIR: H_2O, CO_2, CO, OCS, SO_2, HCl, HF and SiF_4; Mori *et al.*, 1995; Oppenheimer *et al.*, 1998). Satellite remote sensing techniques, on the other hand, mainly detect volcanic sulfur dioxide (SO_2), although detection of HCl, BrO, and OClO is possible for some larger eruptions (Yang *et al.*, 2007). Satellite remote sensing is an important tool for volcanoes in remote or dangerous locations and/or which exhibit dangerous activity.

Nyamuragira volcano (D.R. Congo, Africa) is one of the most prolific SO_2 emitters on Earth. The SO_2 emissions from its recent eruptions in 2006 and 2010 have not been thoroughly investigated; only rough emissions estimates have been calculated for the 2006 eruption (Smithsonian Institution, 2006; Prata and Bernardo, 2007). Emissions from the 2006 eruption reached at least 7 km altitude (Prata and Bernardo, 2007) and drifted as far

as China within ~1 week. The 2010 eruption, however, appeared to be less energetic, although the heights of the eruption clouds from both eruptions are not well constrained. It is important to determine the height and distribution of volcanic plumes in the atmosphere because the properties of the atmosphere (temperature, pressure, water content) differ with altitude, which affects the plume's absorption of ultraviolet (UV) radiation (Yang *et al.*, 2010). Volcanic gases will also undergo different chemical reactions depending on whether they were injected into the troposphere (Oppenheimer *et al.*, 1998; Delmelle *et al.*, 2002; Carn *et al.*, 2005) or stratosphere (Baroni *et al.*, 2007); where the volcanic plume resides in the atmosphere has significant implications for local and global climate changes. Algorithms for UV satellite data have been developed using forward modeling and radiative transfer theory to quantify SO_2 at various plume altitudes (Yang *et al.*, 2007). Choosing the appropriate algorithm, then, requires an estimate of plume altitude in order to more accurately quantify SO_2 from an eruption. We use the following satellite sensors in NASA's A-Train spacecraft constellation to continue the investigation of SO_2 emissions from the most recent Nyamuragira eruptions: the Ozone Monitoring Instrument (OMI), the Atmospheric Infrared Sounder (AIRS), the Microwave Limb Sounder (MLS), the Multi-Angle Imaging Spectroradiometer (MISR), and the Cloud-Aerosol Lidar with Orthogonal Polarization (CALIOP). The A-Train is a series of satellites that take measurements temporally close to one another, allowing comparisons between their data products.

4.1.1 OMI

OMI is a second-generation UV sensor. The first UV satellite remote sensing of volcanic clouds began with the launch of the Total Ozone Mapping Spectrometer (TOMS) in 1978 on the Nimbus 7 satellite. Its original purpose was the measurement of ozone through the absorption of backscattered solar radiation by ozone molecules in six discrete wavelengths within the region of 312-380-nm (Krueger *et al.*, 1995). In 1982, El Chichon volcano (Mexico) erupted and TOMS imagery displayed anomalous ozone values around the volcano, which were later revealed to be the volcanic cloud from El Chichon; Krueger

(1983) determined that SO_2 molecules within volcanic clouds absorb at the shortest TOMS wavelengths and, therefore, produce a similar response as ozone. From then on, TOMS was used to quantify and track volcanic SO_2.

Four satellites have carried the TOMS sensor: 1) Nimbus 7 was launched in November 1978, but failed in May 1993, 2) Meteor-3 was launched in August 1991 and continued taking measurements until November 1994, 3) Earth Probe was launched in July 1996 and collected data until the mission's end in December 2005, and 4) ADEOS, a Japanese satellite, was launched in August 1996, but the satellite's solar array failed in June 1997. These satellites were in a sun-synchronous polar orbit, passing over the equator at roughly local noon every day. The TOMS sensor, therefore, was able to produce daily contiguous global maps of ozone and SO_2 with a footprint of 50 x 50 km (Nimbus), 47 x 47 km (Meteor-3), and 39 x 39 km (EP) at nadir.

TOMS is a spectrophotometer, which measures the albedo of Earth's atmosphere by determining the ratio between the spectral radiance of the sunlit Earth's atmosphere and the radiance of a sunlit-calibrated diffuser plate from a satellite platform (Krueger *et al.*, 1995). Two pairs of shorter wavelengths are sensitive to ozone and SO_2 absorption (312, 317, 331, and 339) and two longer wavelengths (360 and 380) are not affected by absorption, making them appropriate for the determination of radiance from the ground or clouds (Krueger *et al.*, 1995). At short wavelengths, SO_2 absorbs more strongly and differences in absorption coefficients between SO_2 and ozone allow the discrimination between the two species (Figure 4.1; Krueger *et al.*, 1995).

Estimates of SO_2 abundance are calculated with a Linear Model (Kerr Algorithm), which takes into account absorption and scattering of UV radiation and utilizes Beer's Law:

$$I(\lambda) = I_0(\lambda) \exp [-\tau_\alpha(\lambda)]$$

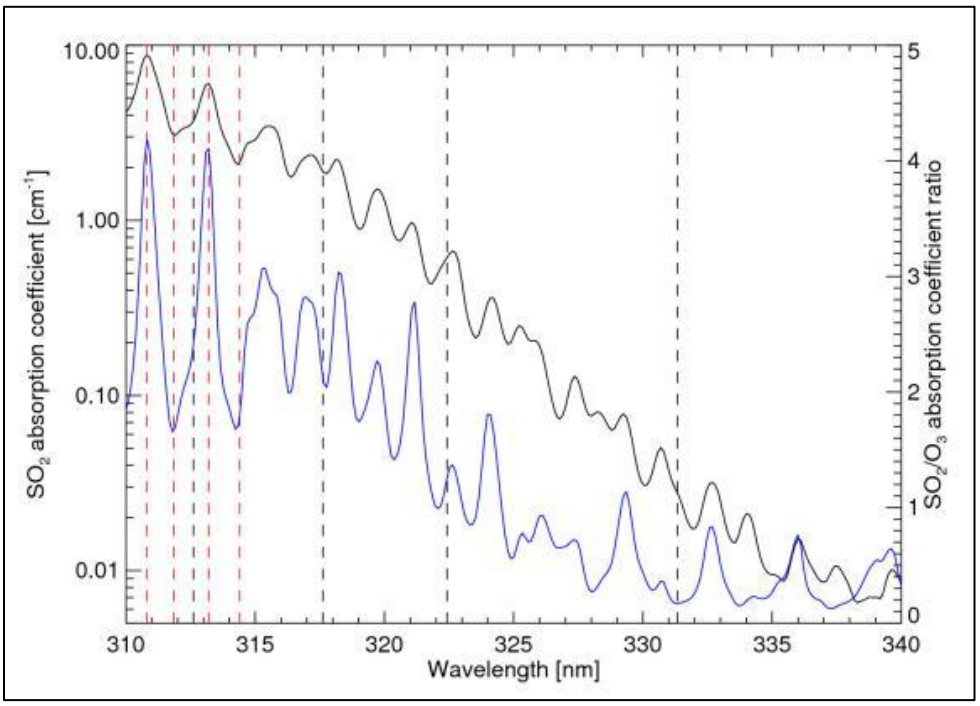

Figure 4.1 The windows of SO_2 and ozone absorption. SO_2 absorbs more strongly at shorter wavelengths, while ozone absorbs more strongly at longer wavelengths. Both TOMS and OMI utilize these absorption features. Dashed lines represent the OMI wavelengths used for the Linear Fit (LF) algorithm (see below). (Image courtesy of Simon Carn.)

where $I(\lambda)$ is the intensity of the radiation at wavelength, λ, reaching the satellite, τ_a is the absorption optical path through the atmosphere, and $I(\lambda)$ is the intensity of the radiation expected in the absence of any atmospheric absorption. Background SO_2 is estimated by interpolating between areas north and south of the plume that contained no volcanic SO_2 (Krueger *et al.*, 1995). Subtraction of background SO_2 from the plume SO_2 results in the true SO_2 column amounts. Column SO_2 is reported in Dobson units (milli-atm cm; a one-dimensional thickness (0.01 mm) of the gas layer at STP). The detection limit of TOMS is 5-10 kt and the accuracy of TOMS measurements is ±30%. Errors include anomalies in background SO_2 concentrations, reflective background surfaces and meteorological clouds,

plume altitude, scan position biases, and ash or aerosols within the SO_2 plume (Krueger *et al.*, 1995). At higher latitudes, larger algorithm errors occur due to the increasing path lengths. Published TOMS studies use the ±30% error estimate due to variations between each study location, and sometimes between each scene, with respect to meteorology, geography, cloud composition, and background.

OMI was launched on July 15, 2004 to replace TOMS. The latter was not originally designed for volcanic cloud detection and, therefore, higher spectral and spatial resolution was implemented in the OMI instrument to help better resolve volcanic and anthropogenic SO_2. OMI is on-board NASA's Aura polar-orbiting sun-synchronous satellite at an altitude of 705 km, with an equatorial crossing (ascending node) at 1:45pm local time. Aura also carries the MLS sensor, allowing a closely timed comparison of data between MLS and OMI.

Like TOMS, OMI detects backscattered radiation in the UV. However, OMI employs a two-dimensional charge coupled device (CCD) detector, which allows simultaneous measurement of backscattered radiation in both spectral and spatial dimensions (Krueger *et al.*, 1995). Pushbroom measurements enable instantaneous collection of OMI data across the swath compared to the whiskbroom mode of TOMS. These improvements allow OMI to be much more sensitive to trace gas measurement than TOMS. OMI is also a hyperspectral sensor, which measures the full UV (270-365 nm) and visible (VIS) (365-500 nm) spectra instead of the six discrete bands TOMS detected. The coverage is global with once-daily images at low latitudes and an improved footprint of 13 km x 24 km compared to TOMS (Levelt *et al.*, 2006). Other than SO_2 and ozone, OMI also measures other trace gases including NO_2, HCHO, BrO, and OClO, and provides an Aerosol Index (AI) and cloud pressures (Levelt *et al.*, 2006). SO_2 detection limits for OMI are on the order of 0.05 kt compared to the higher detection limits of TOMS (~7 kt; Carn *et al.*, 2008).

The first OMI SO_2 retrievals were generated using the band residual difference (BRD) algorithm. Four wavelengths were used between 311 and 314 nm, centered on minimum and maximum SO_2 absorption, which allows maximum sensitivity to small SO_2 column abundances due to the large differential absorption at these wavelengths (Krotkov *et al.*, 2006). Unfortunately, the BRD algorithm is unsuitable for plumes with large amounts of SO_2 (> ~20 DU) when band residual differences exhibit nonlinear responses (Yang *et al.*, 2007). To address the problems associated with high SO_2 column amounts, the linear fit (LF) algorithm was developed (Yang *et al.*, 2007). Originally applied to Solar Backscattered Ultraviolet (SBUV) data, the LF algorithm was adapted to perform simultaneous retrieval of ozone, SO_2, and surface reflectivity using a flexible set of UV wavelengths (Yang *et al.*, 2007). Although the LF algorithm extends the range of measurable SO_2 column amounts relative to the BRD technique, it also underestimates SO_2 columns for very high SO_2 loadings (>100 DU; Yang *et al.*, 2009).

The most recent improvement is the Iterative Spectral Fit (ISF) algorithm, which attempts to resolve the problem with large SO_2 column amounts. The BRD and LF techniques assumed a linear relationship between SO_2 column and the N-value residual (N-value, N=-100 $\log_{10} I/F$, where I is Earth radiance and F is solar irradiance) differences between the satellite measurement and forward model simulation data (Yang *et al.*, 2009). When the SO_2 amount is small, the linear relationship is valid. However, larger SO_2 column amounts cause stronger absorption, which in turn lowers the amount of photon scatterings, and lowers the measured radiance that passes through the SO_2 plume (thus reducing the measured SO_2 column). The ISF algorithm addresses the non-linear effect by solving the LF equation iteratively with an updated linearization point and weighting functions at each step (Yang *et al.*, 2009). A further improvement was made in Yang *et al.* (2010a) to include an estimate for plume altitude. Radiative properties vary vertically in the atmosphere and, therefore, in order to retrieve the most accurate SO_2 column amount, the algorithm must be adjusted depending on the altitude of the plume in the atmosphere. This is accomplished through successive ISF retrievals until the residuals (difference between the measurements

and forward modeling results) are minimized (Yang *et al.*, 2010b). With a more accurate quantification of SO_2 from the 2006 and 2010 Nyamuragira eruptions, we aim to investigate the fate of the volcanic clouds and the eruption mechanisms. OMI errors are similar those previously mentioned for TOMS and, therefore, we cite a 30% error for our SO_2 values (Krotkov *et al.*, 2006).

4.1.2 AIRS

AIRS is on-board the sun-synchronous Aqua polar orbiting satellite, which is part of the A-Train along with Aura. AIRS infrared pixels are circular at nadir with a diameter of 13.5 km. The pixel size increases and distorts to an elliptical shape with 41 x 21 km dimensions at the swath edges. Measurements are made in a water vapor channel centered near the 7.34 nm wavelength (Prata and Bernardo, 2007), allowing day and night retrievals. AIRS standard operational products include atmospheric temperature, moisture, and minor gases, such as CO_3, CO, and CH_4. However, SO_2 column abundance is possible by exploiting the 1295-1405 cm^{-1} SO_2 absorption window through radiative transfer programs (Carn *et al.*, 2005; Prata *et al.*, 2007). The SO_2 retrieval is a two-step process with the first step consisting of SO_2 pixel identification and the second step consisting of a least squares solution based on off-line radiative transfer calculations (Prata and Bernardo, 2007). Like OMI retrievals, it was found that up to 40 DU the relationship between measured and modeled absorption spectra is linear, but beyond 50 DU the absorption becomes non-linear and follows more of a square-root relationship (Prata and Bernardo, 2007). A reference or background pixel is found by comparing the absorbance spectrum with a library of synthetic spectra for each pixel and the highest R^2 correlation is then deemed the reference (Prata and Bernardo, 2007). The reference pixel is typically geographically near the SO_2 plume and the assumption, therefore, is that the reference pixel is sampling similar atmospheric conditions as the SO_2 plume.

The detection limit for AIRS is 6 DU (~24-115 kt, a range corresponding to 6 DU measured from nadir to swath edge pixels). Errors in AIRS retrievals occur when SO_2 exists in the background absorbance spectrum, and also depend on the radiometric accuracy of AIRS channels, plume height inaccuracies, spectroscopic parameters for SO_2, or interference from meteorological clouds and other gas species, especially when the plume lies within or below meteorological clouds (Prata and Bernardo, 2007). Water vapor strongly absorbs in this infrared channel and, therefore, water vapor influences the SO_2 retrievals. As water vapor is most abundant in the lower troposphere (below ~3 km), SO_2 retrievals from infrared sensors like AIRS are less reliable at these lower altitudes. Above 3 km (upper troposphere) and into the lower stratosphere (~8-15 km), the SO_2 retrievals are more reliable (Prata and Bernardo, 2007).

4.2 OMI and AIRS Retrieval Methods

4.2.1 OMI

We used the Level 2 OMSO2 OMI product and these data were downloaded from NASA's Mirador web site (http://mirador.gsfc.nasa.gov/). OMI data from 27 November until 4 December were processed for the 2006 Nyamuragira eruption and data from 3 January until 28 January were processed for the 2010 eruption. The OMI data were processed with a script called OMIPLOT written in Interactive Data Language (IDL). After navigating to the appropriate directory that contains the code and data, the IDL program and OMIPLOT script is called up at the prompt. After the program loads, the "Load a single OMSO2 orbit" is then chosen. There are options to filter the SO_2 data with reflectivity, cloud fraction, or solar zenith angle data, but the data were not filtered. The linear fit (LF) algorithm was chosen and the day/month/year of interest was input. A minimum and maximum latitude and longitude is entered to focus in on the region of interest. A Mercator projection was used and volcano locations were plotted. A scale is input for the average SO_2 column (0,5) and Aerosol Index (-2,2) plots.

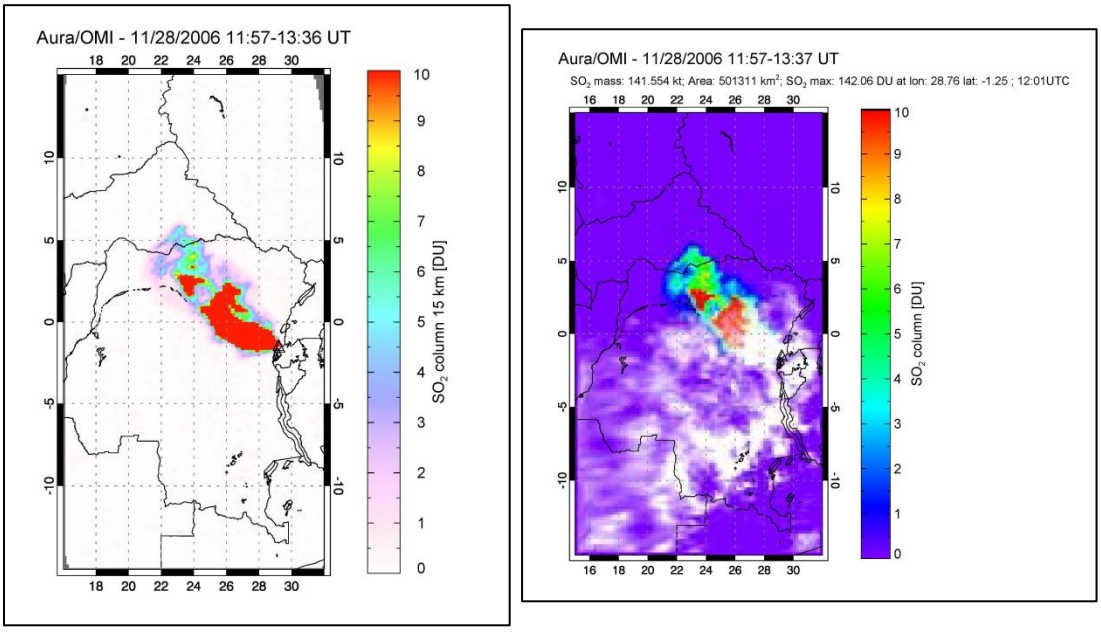

Figure 4.2 An OMI image of the 28 November 2006 Nyamuragira eruption plume (left), and an OMI image of the same day with meteorological cloud cover superimposed over the SO_2 image (right). It is necessary for the user to define background SO_2 areas (nominally free of SO_2) near the plume. An average SO_2 value between the north and south background areas (typically boxes are drawn within the program) is subtracted from the plume SO_2 to arrive at total SO_2 column amount. As seen in Table 4.1, the program automatically subtracts the SO_2 within the defined background from the defined plume amount.

The program outputs include images of SO_2 retrievals for four different plume altitudes, as well as reflectivity and aerosol index. SO_2 column amounts are determined for the plume and reference background by drawing "plume" and "background" boxes on one of the SO_2 images (Figure 4.2). The OMIPLOT program automatically subtracts the normalized background SO_2 amounts from the SO_2 amount calculated in the plume box and outputs SO_2 column amounts for each of the plume attitudes (Table 4.1).

Table 4.1

The output from the omiplot program for the Nyamuragira 28 November 2006 eruption. SO_2 masses are calculated for several potential atmospheric plume altitudes (e.g., 3, 5, and 15 km).

```
Background box (N) 1:
Enter minlat, minlon, maxlat, maxlon of plume box: -4,20,7,31
Enter minlat, minlon, maxlat, maxlon of background box 1: 8, 21, 16, 32
Choose new boxes? (y/n) n
   Cloud Min lat :    -4.00000
   Cloud Min lon :     20.0000
   Cloud Max lat :     7.00000
   Cloud Max lon :     31.0000
   SO2PBL cloud box tonnage :     825094 tonnes
   SO23k cloud box tonnage :     327112 tonnes
   SO25k cloud box tonnage :     130104 tonnes
   SO215k cloud box tonnage :     142645 tonnes
   SO2 cloud box area :    1535388 km^2
   Normalized background PBL tonnage :      -8550 tonnes
   Normalized background 3 km tonnage :       1441 tonnes
   Normalized background 5 km tonnage :       478 tonnes
   Normalized background 15 km tonnage :       247 tonnes
   Background box area :    1091883 km^2
   SO2 cloud tonnage (PBL):     833645 tonnes
   SO2 cloud tonnage (3 km):     325671 tonnes
   SO2 cloud tonnage (5 km):     129625 tonnes
   SO2 cloud tonnage (15 km):     142397 tonnes


Background box (S) 2:
Enter minlat, minlon, maxlat, maxlon of plume box: -4,20,7,31
Enter minlat, minlon, maxlat, maxlon of background box 1: -15,19,-5,29
Choose new boxes? (y/n) n
   Cloud Min lat :    -4.00000
   Cloud Min lon :     20.0000
   Cloud Max lat :     7.00000
   Cloud Max lon :     31.0000
   SO2PBL cloud box tonnage :     825094 tonnes
   SO23k cloud box tonnage :     327112 tonnes
   SO25k cloud box tonnage :     130104 tonnes
   SO215k cloud box tonnage :     142645 tonnes
   SO2 cloud box area :    1535388 km^2
   Normalized background PBL tonnage :     -42373 tonnes
   Normalized background 3 km tonnage :      -4915 tonnes
   Normalized background 5 km tonnage :      -1940 tonnes
   Normalized background 15 km tonnage :      -1547 tonnes
   Background box area :    1241357 km^2
   SO2 cloud tonnage (PBL):     867468 tonnes
   SO2 cloud tonnage (3 km):     332028 tonnes
   SO2 cloud tonnage (5 km):     132044 tonnes
   SO2 cloud tonnage (15 km):     144192 tonnes
```

4.2.2 AIRS

We used the Level 1B AIRIBRAD (geolocated and calibrated radiances) AIRS product and these data were downloaded from NASA's Mirador web site. The same image dates were chosen for AIRS as they were for OMI data in order to compare the two. AIRS data were processed with an IDL batch script (SO2AIRS.b) that invokes the SO_2 algorithm of Prata and Bernardo (2007). Again, after navigating to the appropriate directory, open IDL. The SO2AIRS.b script is called up and the program loads. The event directory is entered (in this case, "Nyamuragira") and the appropriate AIRS hdf file is chosen. Since the algorithm chooses a background pixel, there is no need to identify background reference for AIRS, unlike OMI. However, this may create a source of error, especially if the granule is filled with the plume and no suitable background is available (Prata and Bernardo, 2007). The output includes a binary file (placed in the Binary subdirectory) and a Quicklook image (placed in the JPEGs directory), which displays the brightness temperature difference between two key AIRS channels. An additional script (SO2_map.b) allows the binary file to be plotted as a georeferenced color map of the SO_2 plume (Figure 4.3).

4.2.3 Volcanic Cloud Height Determinations

OMI measures total column SO_2 abundance in the atmosphere. The distribution of this SO_2 within the column is very important as variations in plume altitude impact the algorithm's estimate of column amount due to the pressure and temperature dependence of SO_2 absorption and radiative transfer (Figure 4.4). Two algorithms are used to retrieve SO_2 column amounts corresponding to four different SO_2 vertical profiles. The SO_2 plume heights in each profile are calculated using a center of mass altitude (CMA), which is derived from SO_2 vertical distribution and used to interpolate between the four different profiles. The planetary boundary layer (PBL) column amount is produced with the BRD algorithm. PBL is most appropriate for low altitude SO_2 (e.g., CMA of 0.9 km; anthropogenic sources). The LF algorithm retrieves SO_2 column amounts for lower

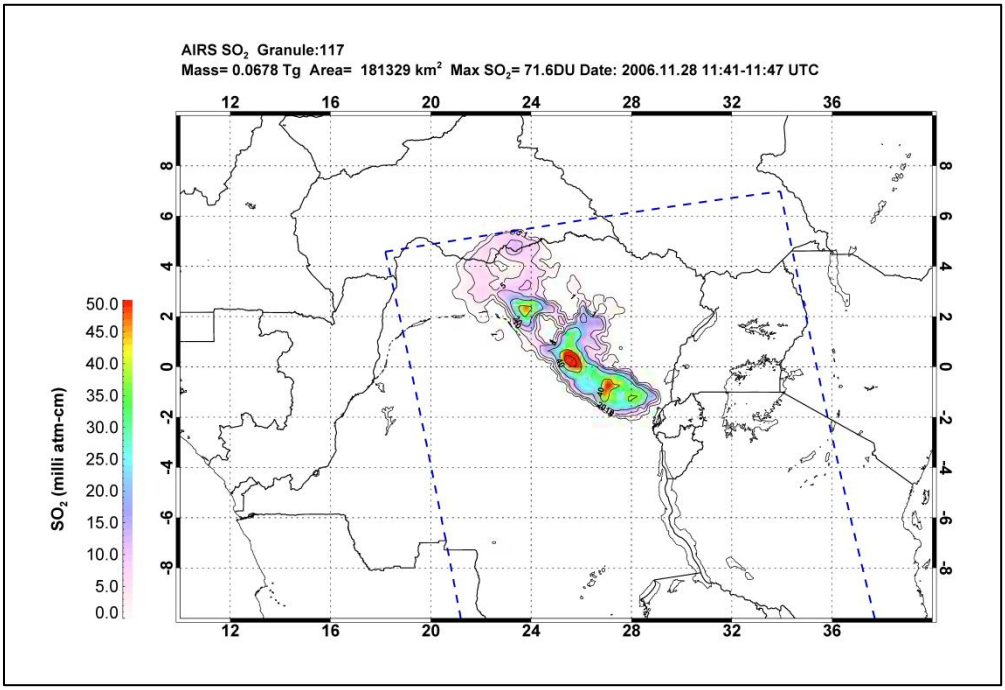

Figure 4.3 AIRS SO_2 retrieval for the 28 November 2006 eruption. Note the blue dashed line, which represents the extent of the AIRS granule. A background pixel (nominally SO_2 free) within this granule is determined automatically by the program. Figure 4.2 shows the same plume as measured by OMI.

tropospheric (TRL; CMA of 2.5 km), middle tropospheric (TRM; CMA of 7.5 km), and upper tropospheric (STL; CMA of 17 km) plumes. Choosing the correct altitude, then, becomes important for accurate retrievals.

For example, if the actual SO_2 in a cloud-free pixel is at a lower altitude than the estimated level (e.g., 15 km), the TRM retrieval will greatly underestimate the actual SO_2 column amount (Yang *et al.*, 2007). With AIRS, although it does constrain the volcanic plume height in the atmosphere in some respect (e.g., the plume has to be above meteorological clouds for AIRS to sense the plume), additional methods helped to better constrain the plume heights and, in turn, better constrain the OMI SO_2 measurements. In order to determine the altitudes of the volcanic clouds from the 2006 and 2010 Nyamuragira

eruptions, Hybrid Single-Particle Lagrangian Integrated Trajectory (HYSPLIT; Draxler and Rolph, 2003) modeling and assessment of Microwave Limb Sounder (MLS), Multi-Angle Imaging Spectroradiometer (MISR), and Cloud-Aerosol Lidar and Infrared Pathfinder Satellite Observation (CALIPSO) data were carried out.

HYSPLIT

HYSPLIT is a model that computes simple air parcel trajectories at various altitudes using archive meteorological data (http://www.arl.noaa.gov/HYSPLIT_info.php). Effusive eruptions often emit a continuous stream of volcanic gas and, because UV and IR satellite sensors take daily "snapshots" of the volcanic cloud, the daily images usually include SO_2 plume ages ranging from freshly emitted to >24 hours old (Carn and Bluth, 2003; Bluth and Carn, 2008). In addition to constraining the altitude and maximum drift distance of each daily plume, we used HYSPLIT modeling to determine what portion of the cloud was </= 24-hours old (Figure 4.5).

MLS

Launched 15 July 2004 on-board the Aura satellite, MLS is a forward-looking radiometer that detects microwave emission (between 118 GHz-2.5 THz) from the atmosphere day and night using a limb view and provides coarse vertical profiles of gases (e.g., SO_2, ozone, HCl, BrO, ClO, N_2O), temperature, humidity, pressure, and cloud ice (Waters *et al.*, 2006). MLS measures volcanic SO_2 between 190-640 GHz in the upper troposphere and lower stratosphere only (~17-50 km altitude; 215-10 hPa), which provides constraints on the height of Nyamuragira's plumes. The 190-640 GHz channels have a horizontal field of view of 2.9-8.4 km and a vertical field of view of 1.4-4.2 km (Waters *et al.*, 2006). Vertical resolution of the SO_2 product is ~3 km and the horizontal resolution is 170 km (Livesey *et al.*, 2011). The accuracy of SO_2 retrievals are ~5 ppbv for pressures less than 147 hPa and at 215 hPa, the accuracy increases to ~20 ppbv (Livesey *et al.*, 2011). We used the version

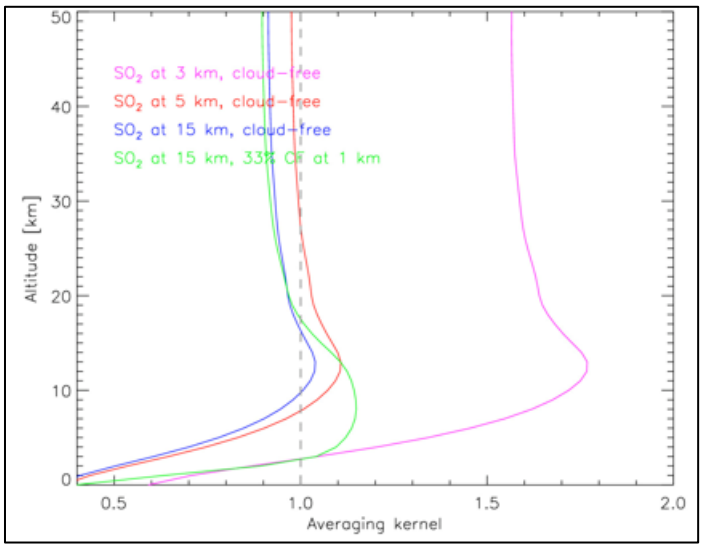

Figure 4.4 OMI LF SO2 algorithm averaging kernel (AK) showing the vertical sensitivity of OMI SO_2 retrievals. The y-axis is plume altitude, while the x-axis is calculated by multiplying weighting functions by a set of retrieval coefficients. The curves shown correspond to different a-priori assumptions of SO_2 altitude and cloud fraction in an OMI scene. SO_2 column amounts are overestimated where AK > 1 and underestimated where AK < 1. (Image courtesy of Simon Carn.)

3 MLS Level 2 SO_2 Mixing Ratio product (ML2SO2). Data were downloaded from NASA's Reverb web site (http://reverb.echo.nasa.gov/reverb/).

MISR

MISR is on-board the sun-synchronous Terra satellite, with an equator crossing (descending node) at ~10:30 local time and a global repeat time of 16 days. The spatial resolution is 216 m for "local mode" selected scenes and 1.73 km for "global mode" global coverage; there are no gaps in coverage (Diner *et al.*, 1989). Three visible wavelength bands (blue, green, and red) and one near-infrared channel images the Earth's surface and atmosphere. MISR is equipped with nine cameras with different viewing angles (25.8°, 45.6°, 60.0°, and 72.5°) aligned along the spacecraft ground track (Diner *et al.*, 1989). MISR provides estimates of aerosol amounts and optical characteristics, as well as aerosol

scattering properties, in the atmosphere, cloud classification, and land surface cover (Diner *et al.*, 1989). MISR data can be downloaded from NASA's Reverb web site (http://reverb.echo.nasa.gov/reverb/). We obtained the 20 November 2006 L1B2 MISR product and used all nine cameras to compute the plume height stereoscopically. An IDL-based program called the MISR Interaction explorer (MINX) (Nelson *et al.*, 2009) uses the data from the nine different camera positions to create a 3-D cloud image, from which cloud height is obtained. The output is a height profile plot, corrected for wind velocity (Figure 4.6).

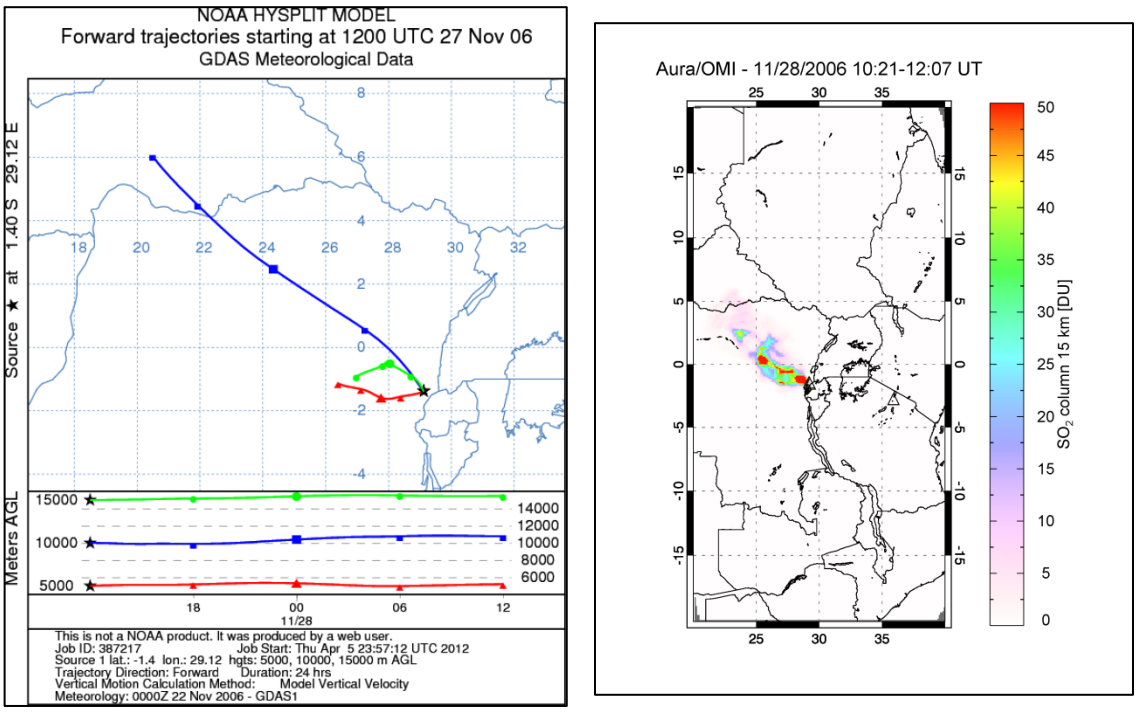

Figure 4.5 A HYSPLIT modeling run for the 24-hours proceeding the daily OMI image (taken at ~local noon) for the 28 November 2006 plume, indicates that an altitude of ~10 km best represents the Nyamuragira plume on this day (left). The 5 km OMI retrieval (CMA=7.5 km), therefore, was used to calculate SO_2 column amounts for this day of the eruption (right).

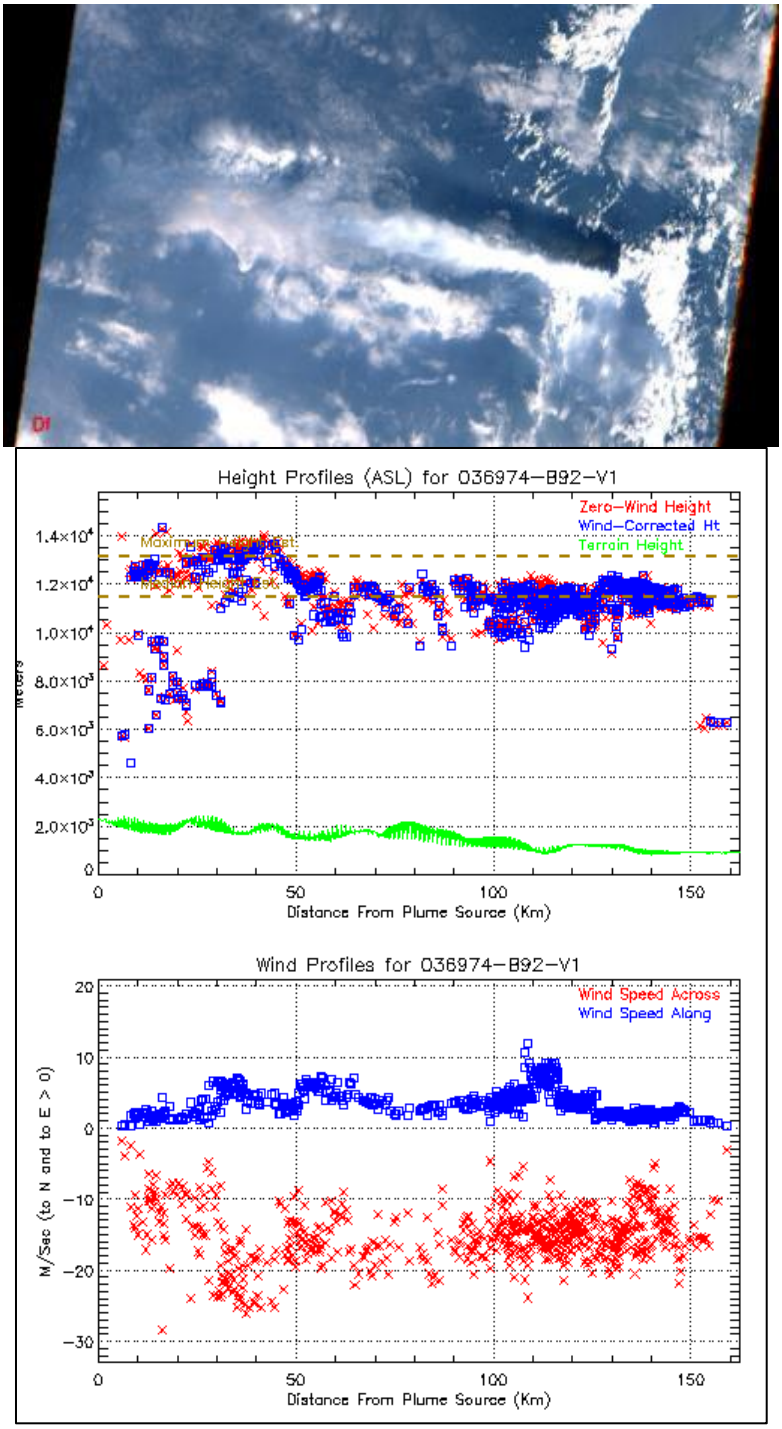

Figure 4.6 An image of MISR camera 9 (top) illustrates the shadowing effect of the Nyamuragira 30 November 2006 plume. Using data from MISR cameras 1-9, MINX software (Nelson *et al.*, 2009) allows the stereoscopic calculation of plume height, shown as the height profile, which has been corrected for wind velocity (bottom). The Nyamuragira cloud height peaks at 14 km (assumed to be over the vent) and then drifts to an 11-12 km height as it disperses from the vent. Clouds are estimated at heights between 12-14 km.

CALIPSO

The CALIPSO satellite, part of the A-Train, carries both an active lidar instrument and two passive detectors of infrared and visible wavelengths (Winker *et al.*, 2009). The primary instrument on-board is the CALIOP (Cloud-Aerosol LIdar with Orthogonal Polarization), which acquires vertical daytime and nighttime profiles of atmospheric backscatter at 1064 and 532 nm with a repeat time of 16 days. Clouds and aerosols produce different backscattering signals, which allows CALIOP to discriminate between the two, using various algorithms. Primary algorithms allow the identification of cloud and aerosol layers, secondary algorithms classify each layer as cloud or aerosol, and tertiary algorithms create atmospheric profiles of both cloud and aerosol (Winker *et al.*, 2009). The retrieval is more sensitive with altitude because molecular scattering decreases with altitude (Winker *et al.*, 2009). A depolarization feature allows ice clouds, water clouds, and non-spherical aerosol particles to be discriminated as well (Winker *et al.*, 2009). CALIOP's ground footprint is 100 m with a footprint spacing (horizontal resolution) of 333 m and a vertical resolution of 30-300 m from 0-40 km. Unlike MLS and MISR, which were used for plume height estimates, we used the CALIOP data mainly to determine the height of the meteorological clouds around the plume. We attempted to determine plume height by exploiting the ability of CALIOP to detect aerosols (potentially within the volcanic plume), but the results were inconclusive.

4.3 Results

Volcanic plumes are detected once daily by OMI, providing a "snapshot" of the emissions. For effusive plumes, it is possible for each daily image to contain new SO_2 (erupted between OMI images) and older, decaying SO_2 from previous day(s), particularly for high-altitude plumes where SO_2-to-sulfate conversion is slower compared to low-altitude tropospheric plumes (Oppenheimer *et al.*, 1998). For an initial evaluation of "fresh" SO_2 within each OMI image, two SO_2 emissions estimates were determined, which include a total SO_2 emission value (all SO_2 in each daily image) and a 24-hour SO_2 emission value

(only the portion of the cloud deemed to have been emitted in the 24-hours prior to the last OMI image) for each day of the Nyamuragira eruptions. Since late August 2008, OMI data has been affected by a row anomaly, thought to originate from an obstruction of the sensor's nadir viewing port (http://www.knmi.nl/omi/research/product/rowanomaly-background.php). The 2010 data was, therefore, affected by this issue and retrievals for some days were not possible.

Appendix F shows each of these values along with the AIRS estimates (when AIRS detected the SO_2 plume), the HYSPLIT trajectory results, and the suggested plume heights from MLS and/or MISR data. The MISR data on 30 November 2006 suggest a maximum plume height of 12-14 km, HYSPLIT results suggest a 10 km cloud altitude (Figure 4.5), and MLS data suggest a 11 km plume height. When comparing these data, it is important to keep in mind that MISR and MLS data typically report the top of the plume, although effusive plumes are undoubtedly distributed throughout the atmospheric column, from the vent to the "plume top" altitude.

We only compared AIRS to OMI Total SO_2 values because we have not yet carried out AIRS 24-hour calculations. AIRS emission values were always lower than OMI Total SO_2, suggesting that AIRS detected only part of the plume (Appendix F). In order to determine which OMI retrieval to apply, the following guidelines were consistently used: if the MLS height was ~10 km, the TRM retrieval was chosen and for heights below 10 km, we used the TRL retrieval. At times, the HYSPLIT-derived heights were below 10 km while the MLS was above. In these instances, the AIRS data were helpful. If AIRS detected much of the plume (implying a high-tropospheric altitude plume), the OMI TRM retrieval was chosen. The plume heights for days prior to and after the day in question were also observed. If it was clear that the plume was at ~10 km the day before and after, then the plume was assumed to be at ~10 km. Although daily fluctuations in activity may cause plume height to vary, due to a lack of distinct corroborating data we found this protocol most logical in order to choose an algorithm.

Emissions from the 2006 eruption appear to build to a peak on 30 November and then decline until the eruption was no longer detected by OMI. The 2010 eruption also appears to build to a peak on 9 January, but then another peak later in the eruption (17 January) implies renewed activity (Figure 4.7). Emissions from the 2010 eruption seem to vary more with low emissions interspersed between the higher emission days and the first peak was preceded by more erratic emissions than for the 2006 eruption. The OMI row anomaly resulted in the inability to retrieve SO_2 from some days in 2010, which is seen in both Appendix F and Figure 4.7.

4.4 Discussion

4.4.1 OMI Observations of the 2006 and 2010 Eruptions

Variations in Retrievals with Cloud Height

In the tropical region of the D.R. Congo, cloud cover is common and these clouds may have affected our SO_2 emissions estimates by increasing scattering and decreasing SO_2 column amounts (e.g., a day of low SO_2 between days of high SO_2). After observation of the reflectivity product of OMI (mostly backscattered UV radiation from meteorological clouds) for each scene, we found that high reflectivity clouds were often geographically located in the same area as the SO_2 plume. The position of the clouds (above or below the plume) would dictate whether the SO_2 retrieval might be overestimating or underestimating the SO_2 column amounts. MLS data suggest that the top of the Nyamuragira cloud was at a maximum height of 11-12 km (Figure 4.8). Using a backscattered LiDAR CALIOP image on 28 November 2006 as an example (Figure 4.9), we assess the altitude of the meteorological clouds near the plume. The OMI image shows cloud cover near the southern portion of the plume, closest to the vent (Figure 4.2).

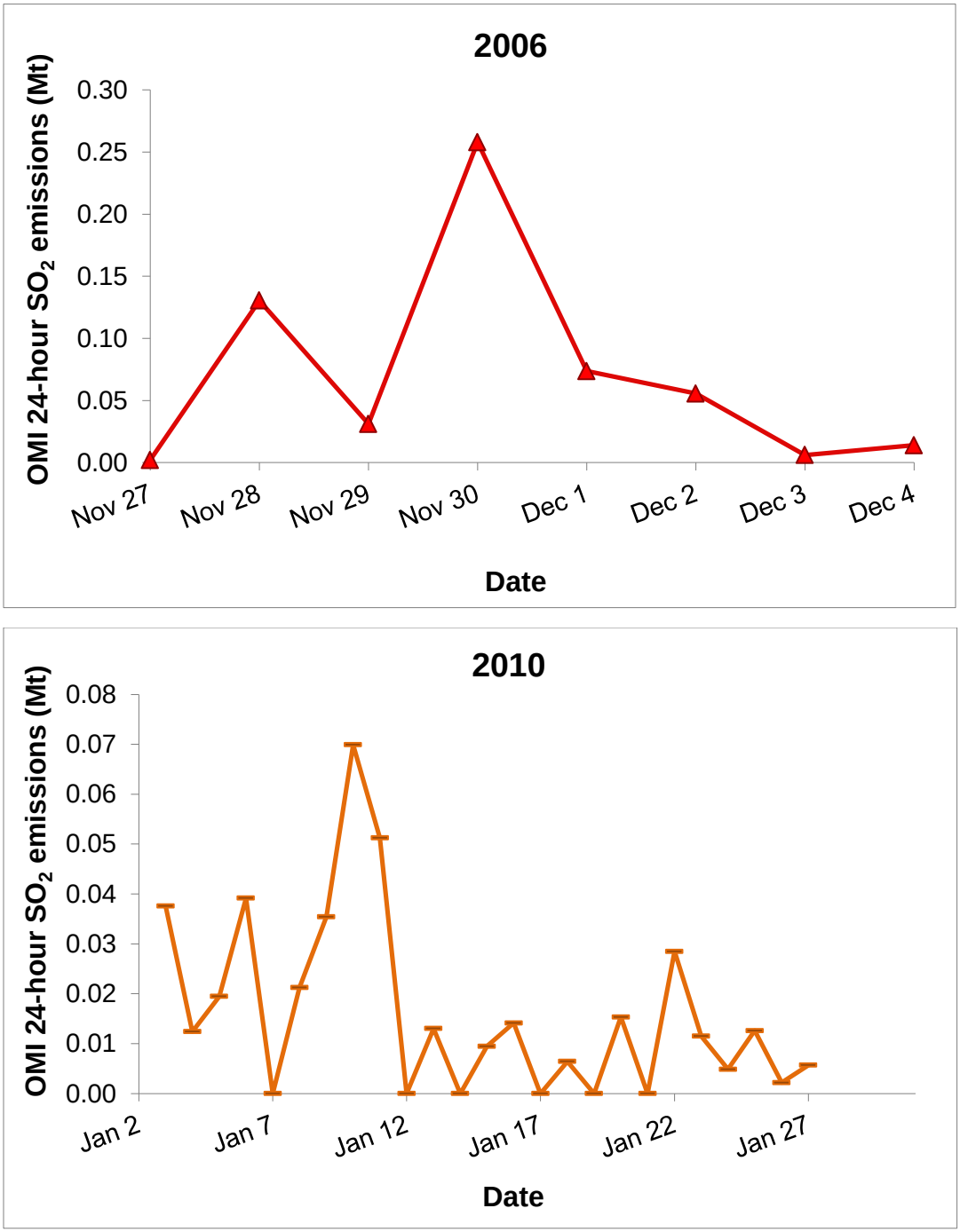

Figure 4.7 OMI 24-hour daily SO_2 column amounts (revised with knowledge of cloud height) for the 2006 and 2010 eruptions. The 24-hour amounts entailed analyses of only the fraction of the plume (SO_2) we determined was emitted within the previous 24-hours using HYSPLIT modeling.

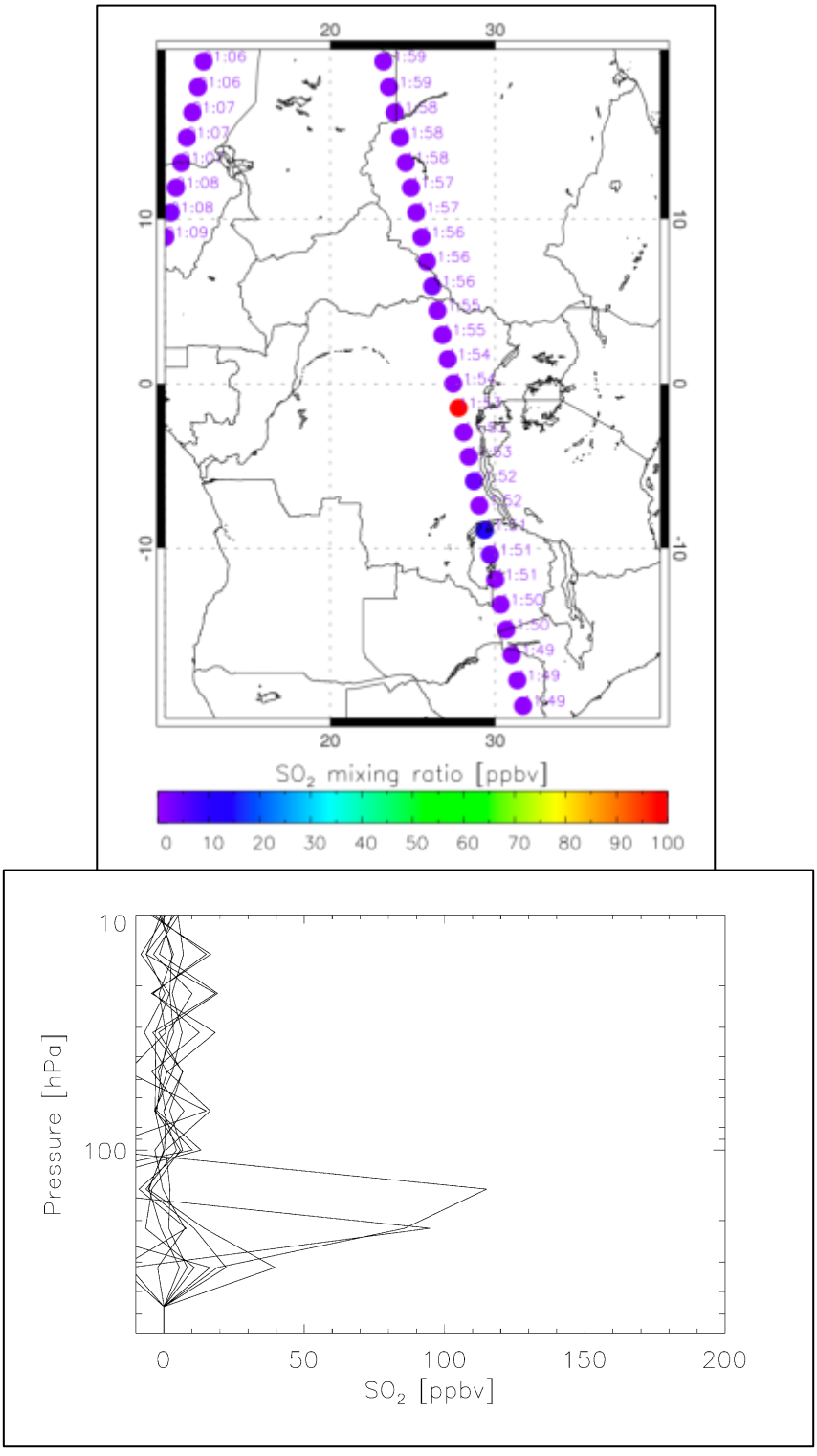

Figure 4.8 The MLS image (top) was acquired on 28 November 2006 and shows large SO_2 column amounts in the path of the Nyamuragira plume. This MLS retrieval is at 146 mb pressure (just under 10 km). A profile of column SO_2 (bottom) for the same day further illustrates that the peak pressure (altitude) of detected SO_2 lies at ~10 km

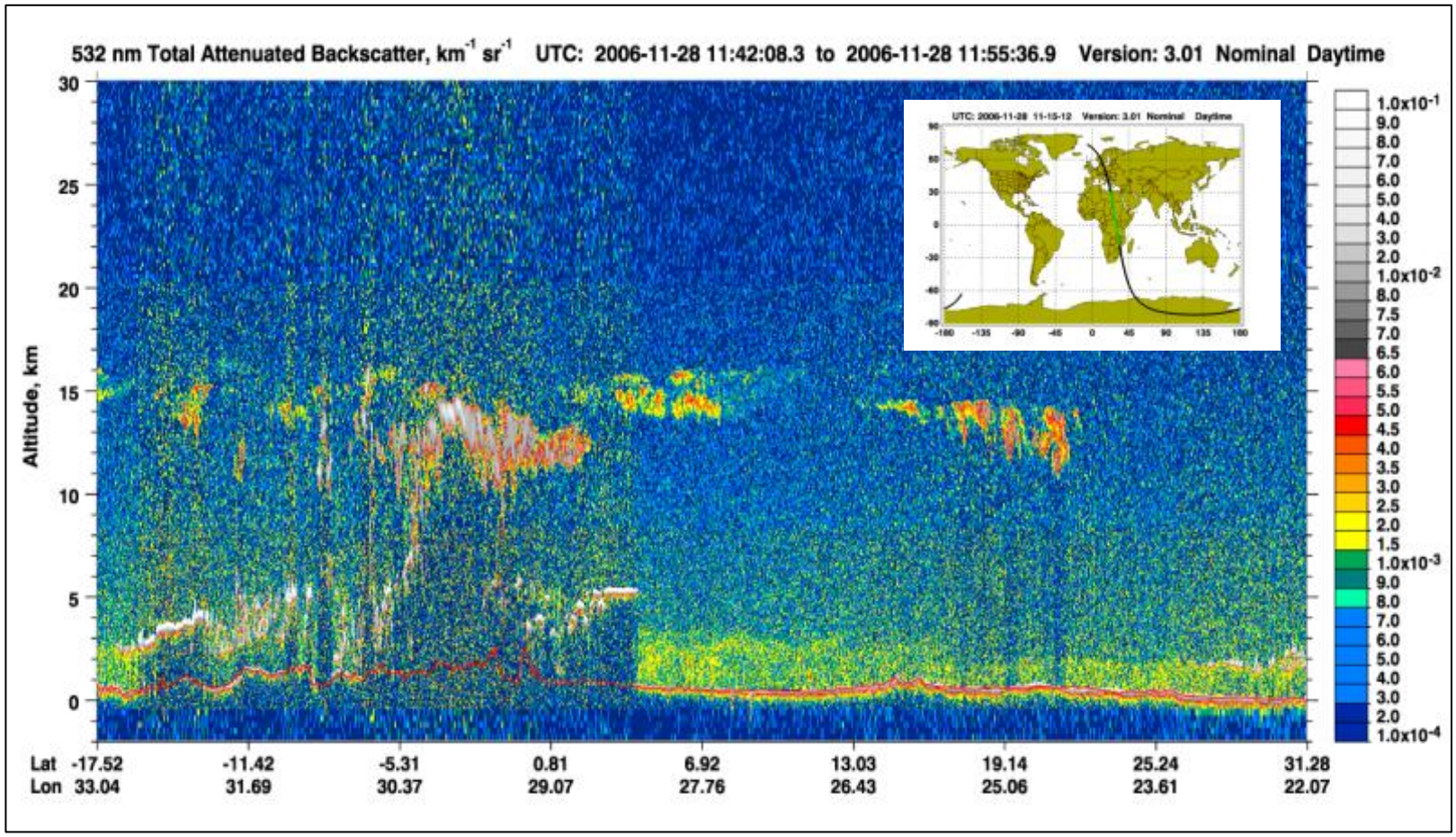

Figure 4.9 The grey mass between -5.31, 30.37 and 0.81, 28.07 likely represents the meteorological clouds present in the OMI image above. These clouds lie between 10-15 km where the MLS data constrain the top of the SO_2 cloud at 11-12 km. Therefore, clouds may have affected at least part of the SO_2 retrieval on this particular day of the eruption. (These data were obtained from the NASA Langley Research Center Atmospheric Science Data Center.)

4.4.2 Observations of Nyamuragira Eruptions

Ground observations of the eruptions are another way to determine if our cloud height estimates and, hence, revised OMI SO_2 emissions estimates are reasonable. Observations of the 2006 eruption were hindered by poor weather conditions and the inability to fly helicopters over the eruption site due to political issues. Some observations were made, however, and these are available on the Smithsonian's Global Volcanism Network (GVN) web site (Smithsonian Institution, 2006). The 2010 eruption, on the other hand, was well documented with written observations and aerial photos; these observations are also available on the GVN web site. Observers included personnel from the United Nations Organization Mission in the D.R. Congo, GVO staff, the United Nations Office for Project Services (UNOPS), the Royal Museum for Central Africa (Belgium), and the National Museum of Natural History of Luxembourg.

2006

Heightened seismic activity occurred eleven months prior to the 2006 eruption (Mavonga *et al.*, 2010). In late June 2005, the activity peaked with long-period earthquakes in two main areas of concentration, 15-25 km depth and 0-4 km depth. Another peak of long-period earthquakes occurred in October 2005 N of the volcano. No other pre-eruption information was reported. As there are very little observations associated with the 2006 eruption, our SO_2 measurements are important to further our understanding of this eruption.

OMI and AIRS both first detected the 2006 plume at ~local noon on 27 November (AIRS-Figure 4.10). However, the eruption was not observed on the ground until later that day (8 pm; Smithsonian, 2006). This indicates that OMI is useful for constraining eruption start dates, particularly in remote locations. Strong degassing with little to no fire fountaining may have occurred as early as 26 November; only when fire fountaining began (or heightened) and darkness fell would observers notice the eruption glow from Goma. The

possibility of the plume originating from Nyiragongo is unlikely for the fact that the plume structure on the 27th indicates an origin near the Nyamuragira main crater and the plume is moving in a northeast direction, where Nyiragongo plumes typically travel southeast (Figure 4.10).

After eruption began on 27 November, the Toulouse VAAC determined that there was an ash cloud at 3-6 km altitude. Our HYSPLIT and MLS height measurements indicate that the maximum height of the SO_2 cloud was between 7-12 km. This suggests a potential separation between the ash and gas portions of the cloud. The Aerosol Index (AI) images

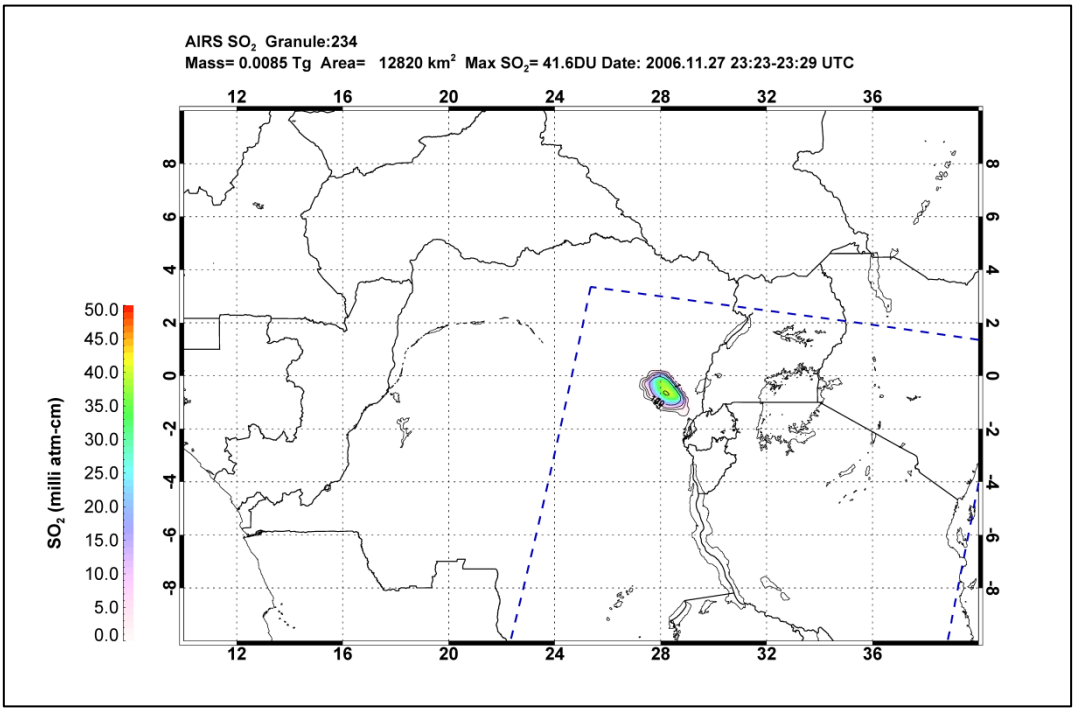

Figure 4.10 AIRS image of the 2006 Nyamuragira eruption. OMI detected the plume even earlier (~noon that day, compared to the ~midnight AIRS acquisition seen here). Ground observations were not made of this eruption until 2000 on the 27th.

for the 2006 eruption show a positive AI signal (suggesting ash; Krueger *et al.*, 2007) and the AI drifts in the same direction as the SO_2 plume. Since the gas and ash appear to move in the same direction, they could have been either separated by variable heights or contained at the same height. The fact that the SO_2 cloud remained visible by daily OMI images for almost a week supports the higher altitude of the SO_2 cloud. SO_2 dissipates rapidly in the troposphere and, therefore, our observations indicate that the 2006 plume was at least in the tropopause where it would oxidize more slowly.

2010

Six months of heightened seismic activity in the Nyamuragira region started after 3 February 2008 (Smithsonian Institution, 2010). For the next year and a half, seismicity did not increase until the magma reached the surface on the first day of the 2010 eruption, 2 January. This seismicity consisted of both tectonic earthquakes and volcanic tremors, associated with fracturing and magma degassing respectively, which was interpreted to indicate lava being close to the surface prior to the eruption. Nearby GPS and tilt stations located around Goma, Nyiragongo, and Nyamuragira provided continuous geodetic data for the eruption. During the first week, ash fell on Goma and villages to the W and SW, but there was a decrease in ash after this time. The ash caused damage to crops (green beans, sweet potatoes, cassava, and banana).

Both the 2006 and 2010 eruptions began with fire fountaining several hundred meters high, large SO_2 emissions that peaked and then dropped off until the eruptions ended. However, our OMI SO_2 data suggest that the 2006 eruption was more energetic that the 2010 eruption. The AIRS instrument detected more days of the 2006 than the 2010 eruption and both HSYPLIT and MLS data suggests that the 2006 eruption clouds were injected higher into the atmosphere. The 2006 SO_2 plume was injected higher into the atmosphere, remaining visible for almost a week. The weeklong 2006 eruption output a larger amount of SO_2 than the month-long 2010 eruption. A key to the differences between the two

eruptions may lie in the pre-eruptive conditions and the eruption mechanisms of each eruption. The 2006 eruption was preceded by seismicity that suggests magma from depth was injected into the magma reservoir. This injection may have been more volatile-rich and the exsolution of these new volatiles could have triggered the eruption. Interestingly, InSAR data suggest no pre-eruption deformation prior to the 2006 eruption (M. Poland, pers. comm.), which would imply that the magma breached the surface from great depth. If this was the case, the eruption would only last as long as the pressure was relieved and the magma reservoir re-equilibrated (e.g., Burt *et al.*, 1994).

For the 2010 eruption, the seismicity seemed to indicate that the magma was close to the surface prior to the eruption, as suggested by D. Tedesco (Smithsonian Institution, 2010). Perhaps the 2010 eruption was more similar to a Kilauea-style Pu'u O'o eruption in that pressure build-up from continued exsolution of volatiles in the system initiated the propagation of magma into a tectonically weakened dike. Either tectonic conditions or pressurization of the system may have triggered the eruption. Initially, the degassing via fire fountaining would be more vigorous, but as the magma became depleted of volatiles, the fire fountain heights would diminish and eruptive activity would change to mainly lava flows toward the end of the eruption. The 2010 eruption may have been longer because a path was already "started" prior to the initiation of the eruption at the surface, where the 2006 eruption may have "exploded" to the surface from a greater depth. Melt inclusion data and InSAR modeling for the 2010 eruption would help to further elucidate the differences between the two eruptions. More in-depth InSAR modeling of pre-eruption deformation for both the 2006 and 2010 eruptions would lend insight into the magma depth prior to eruption.

Future work includes investigation into the effusion rates of these Nyamuragira eruptions. Effusion rate has been tied to plume heights (e.g., Stothers *et al.*, 1986) and, therefore, a difference in effusion rate between the 2006 and 2010 eruptions could explain the variation in eruption style. At Nyamuragira, as well as other basaltic volcanoes, effusion rate has also

been shown to wax at the beginning of the eruption and then wane until the eruption's end (Wadge, 1980; Wright and Pilger, 2008). We determined volume eruption rates for the 2006 and 2010 eruptions, 60 m^3 s^{-1} and 22 m^3 s^{-1}, respectively. Comparing these rates and our estimated plume heights with the empirical calculations of Stothers *et al.* (1986), our data plot at a higher plume height and lower eruption rate than Mauna Loa (1984) and Laki (1783). However, instantaneous effusion rates will undoubtedly be higher and will follow the waxing and waning pattern, which is also mimicked in our SO_2 data. Effusion rates can be derived via thermal satellite remote sensing and, therefore, future work will focus on attempting to determine more accurate effusion rates with these methods (e.g., Harris *et al.*, 1998). These daily rates could also be compared to SO_2 emissions, in order to assess the relationship between gas and lava emissions.

4.4.3 Impacts of Effusive Basaltic Eruptions

The ability of effusive basaltic eruptions to inject volcanic gases high into the atmosphere (tropopause or stratosphere) has been suggested by researchers focusing on mainly historic eruptions (e.g., Laki 1783; Stothers *et al.*, 1986 and Thordarson *et al.*, 2003). Stothers *et al.* (1986) also included the Mauna Loa 1984 eruption into their study to show that modern, smaller volcanic eruptions are equally capable of injecting volcanic clouds as far into the atmosphere as the tropopause. We add to this line of thought by showing that Nyamuragira effusive eruptions have injected SO_2 to high tropospheric levels. As Nyamuragira is one of the most prolific emitters of SO_2 on Earth, emitting up to 1 Mt SO_2/day (1981 eruption; Bluth and Carn, 2008), if sustained at this level for several days to weeks, Nyamuragira could contribute a significant portion of SO_2 to the upper troposphere. This, in turn, would affect more than the local climate as the SO_2 in the plume would oxidize to aerosols and travel a greater distance. Researchers often rely on melt inclusions to estimate the SO_2 loadings from historical eruptions with little recorded observations. Thordarson *et al.* (2003) and Sharma *et al.* (2006) assume that melt inclusions from divergent and hotspot settings will always yield a 1:1 (no excess S) relationship. However, in Chapter 3, we show

that significant excess S can occur from rift products and this should be considered when making historical estimates of S release.

4.5 Conclusions

OMI was able to detect the first day of the 2006 earlier than ground observations were made, proving its capability to constrain eruption start dates. The 2006 eruption ejected clouds higher into the atmosphere (~15 km) and, therefore, AIRS could see more of this eruption. We calculated more accurate SO_2 emissions from the 2006 and 2010 eruption with the knowledge of volcanic cloud height, which was achieved through both MLS data and HYSPLIT modeling. The 30 November 2006 volcanic cloud was further constrained with MISR data, while CALIOP data allowed an estimation of meteorological cloud height. Clouds, as well as plume heights, affect the SO_2 retrievals. These emissions will be further constrained by performing back-calculations to the vent, as has been carried out by Bluth and Carn (2008) and Head (2006). Effusive eruptions are thought to be more docile than explosive eruptions, injecting volcanic gas to lower altitudes in the atmosphere than larger, explosive eruptions. Basaltic eruptions can, however, be considered explosive. We found that plume heights from Nyamuragira's effusive eruptions reached ~15 km (near-tropopause levels; 2006 eruption). The 2006 volcanic cloud was tracked by OMI for ~1 week and was visible over India. This supports findings that other effusive eruptions in the past (e.g., Laki 1783) were able to inject SO_2 and related aerosols high into the atmosphere, where decay rates are slower, allowing the volcanic constituents to remain in the atmosphere and potentially have global effects.

CHAPTER 5: CONCLUSIONS

Magmatic volatiles exsolve and expand within a magma reservoir, creating pressure on the reservoir walls. When this pressure exceeds the strength of the wall rock, eruptions result, and an elastic strain release occurs until reservoir pressure is equilibrated (e.g. Wadge, 1980). Therefore, understanding how volatiles exsolve in a system and how their exsolution is associated with crystallization and eruption (magma evolution) is very important. Once volcanic volatiles erupt at the surface, they interact with the atmosphere, creating aerosols, which can have negative climatic impacts locally and globally. The relationship between these volatiles (volcanic gases) and the syn-erupted lava has implications for pre-eruptive activity, eruption mechanisms, and eruptive style. In order to begin to understand a system, it is important to quantify 1) the magmatic volatiles prior to eruption, as well as the 2) erupted lava/tephra that potentially carry the volatiles to the surface, and 3) volcanic emissions during eruption. As data was nonexistent for the first and second points and not well constrained for the third during the beginning of my research, this was the main motivation and goal of my dissertation. Through these research efforts, a better understanding of Nyamuragira eruptive activity was accomplished, as well as a better understanding of basaltic and alkalic magma degassing.

1) Addressing the pre-eruptive magma conditions, we carried-out new olivine-hosted melt inclusion volatile (H_2O, CO_2, S, Cl, F) and major element analyses on samples from five historic Nyamuragira eruptions. This data allowed us to estimate the total amount of SO_2 released from the 1986 (0.04 Mt) and 2006 (0.06 Mt) Nyamuragira eruptions using the petrologic method, whereby S contents in melt inclusions are scaled to erupted lava volumes (see 2 below). As these amounts are significantly less than satellite-based SO_2 emissions for the same eruptions (1986 = ~1 Mt; 2006 = ~2 Mt), this indicates that processes within the Nyamuragira magma chamber that may occur prior to eruption are: 1) accumulation of a vapor phase within the magmatic system that is only released during eruptions, and/or 2) syn-eruptive gas release from unerupted magma.

2) Constraining erupted Nyamuragira lava volumes through satellite-based lava flow mapping, we were able to create a map of and derive lava volumes for 1967-2011 flows; volumes for the 1994-2011 eruptions were unknown and only a 1958 flow field map existed at the beginning of this research. We found that, with increasing age, there is an increase in band-4 reflectance. This mainly reflects lava flow (re)vegetation with time, which allows Nyamuragira flows to be easily mapped with Landsat, Hyperion, and ALI data, an advantage for, particularly, volcano observatories where resources are limited as lava flows can be can be quickly and inexpensively mapped (Landsat, Hyperion, and ALI data are free).

3) Nyamuragira gas emissions were quantified with the OMI satellite sensor. The OMI retrievals are sensitive to the plume's altitude in the atmosphere and, therefore, to obtain more accurate SO_2 column amounts, we constrained the maximum height of the SO_2 plume. Cloud height estimates for the 2006 eruption (~15 km) were consistently higher than the for the 2010 eruption (5-10 km). The high-altitude 2006 eruption was also detected by AIRS for more days that the 2010 eruption. Effusive eruptions are not considered capable of injecting volcanic gas to high altitudes in the atmosphere, but we show that they can indeed reach the tropopause. This supports findings that other effusive eruptions in the past (e.g., Laki 1783) were able to inject SO_2 and related aerosols high into the atmosphere, where decay rates are slower, allowing the volcanic constituents to remain in the atmosphere and potentially have global effects.

Future work, which will result in an additional publication, includes the expansion of Chapter 4. An eruption of Nyamuragira in November 2011, during the writing of this dissertation, will be investigated in a similar manner as what is presented for the 2006 and 2010 eruptions. We will quantify both OMI Total and OMI 24-hour SO_2, AIRS SO_2, and we will better constrain cloud heights. Effusion rates for the 2006, 2010, and 2011 Nyamuragira eruptions will also be explored. In addition, we will advance our knowledge of Nyamuragira SO_2 output by constraining a flux of 24-hour SO_2. We will accomplish this

by making 24 transects through each 24-hour plume from vent to terminus, quantifying the SO_2 within each of these transects, and backcalculating the original SO_2 by evaluating various decay rates of sulfur to sulfate conversion within the plume (e.g., Bluth and Carn, 2008; Head, 2006).

CHAPTER 6: REFERENCES

Abrams, M., Abbott, E., Kahle, A., 1991. Combined Use of Visible, Reflected Infrared, and Thermal Infrared Images for Mapping Hawaiian Lava Flows. Journal of Geophysical Research 96, 475-484.

Abrams, M., Bianchi, R., Pieri, D., 1996. Revised Mapping of Lava Flows on Mount Etna, Sicily. Photogrammetric Engineering and Remote Sensing 62 (12), 1353-1359.

Allard, P., Carbonnelle, J., Metrich, N., Loyer, H., Zettwoog, P., 1994. Sulphur output and magma degassing budget of Stromboli volcano. Nature 368, 326-330.

Allard, P., 1997. Endogenous magma degassing and storage at Mount Etna. Geophysical Research Letters 24 (17), 2219-2222.

Allard, P., Burton, M., Mure, F., 2005. Spectroscopic evidence for a lava fountain driven by previously accumulated magmatic gas. Nature 433, 407-410.

Anderson, A.T., 1974. Evidence for a Picritic, Volatile-rich Magma beneath Mt. Shasta, California. Journal of Petrology 15, 243-267

Aoki, K., Kurasawa, H., 1984. Sr isotope study of the tephrite series from Nyamuragira volcano, Zaire. Geochemical Journal 18, 95-100.

Aoki, K., Yoshida, T., 1983. Petrological and Geochemical Studies on the 1981-1982 Lava from Nyamuragira Volcano. In: Hamaguchi, H. (Ed.), Volcanoes Nyiragongo and Nyamuragira: Geophysical Aspects. The Faculty of Science, Tohoku University, Sendai, Japan, pp. 91-96.

Aoki, K., Yoshida, T., Yusa, K., Nakamura, Y., 1985. Petrology and Geochemistry of the Nyamuragira Volcano, Zaire. Journal of Volcanology and Geothermal Research 25, 1-28.

Baroni, M., Thiemens, M.H., Delmas, R.J., Savarino, J., 2007. Mass-Independent Sulfur Isotopic Compositions in Stratospheric Eruptions. Science 315, 84-87.

Bell, K., Powell, J.L., 1969. Strontium Isotopic Studies of Alkalic Rocks: The Potassium-rich Lavas of the Birunga and Toro-Ankole Regions, East and Central Equatorial Africa. Journal of Petrology 10(3), 536-572.

Bluth, G. J. S., Carn, S. A., 2008. Exceptional sulfur degassing from Nyamuragira volcano, 1979-2005. International Journal of Remote Sensing 29 (22), 6667-6685.

Blundy, J., Cashman, K., 2005. Rapid decompression-driven crystallization recorded by melt inclusions from Mount St. Helens volcano. Geology 33, 793-796.

Bonneville, A., Lanquette, A.M., Pejoux, R., Bayon, C., 1988. Reconnaissance des principales unites geologiques du Piton de la Fournaise, La Reunion, a partir de SPOT1. Bulletin de la Societe geologique de France 8, 1101-1110.

Burt, M.L., Wadge, G., Scott, W.A., 1994. Simple stochastic modeling of the eruption history of a basaltic volcano: Nyamuragira, Zaire. Bulletin of Volcanology 56, 87-97.

Carn, S.A., 1999, Application of synthetic aperture radar (SAR) imagery to volcano mapping in the humid tropics: a case study in East Java, Indonesia. Bulletin of Volcanology 61, 92-105, doi: 10.1007/s004450050265.

Carn, S.A., Oppenheimer, C., 2000, Remote monitoring of Indonesian volcanoes using satellite data from the Internet. International Journal of Remote Sensing, 21, 873-910, doi: 10.1080/014311600210344.

Carn, S., Bluth, G.J.S., 2003. Prodigious sulfur dioxide emissions from Nyamuragira volcano (D.R. Congo). Geophysical Research Letters 30 (23), 2211, doi:10.1029/2003GL018465.

Carn, S., Krueger, A.J, Bluth, G.J.S., Schaefer, S.J., Krotkov, N.A., Watson, I.M., Datta, S., 2003. Volcanic eruption detection by the Total Ozone Mapping Spectrometer (TOMS) instruments: a 22-year record of sulphur dioxide and ash emissions. In: Oppenheimer, C., Pyle, D.M., and Barclay, J. (Eds.), Volcanic Degassing. Geological Society, London, Special Pubs 213, pp. 177-202.

Carn, S.A., Strow, L.L., de Souza-Machado, S., Edmonds, Y., Hannon, S., 2005. Quantifying tropospheric volcanic emissions with AIRS: The 2002 eruption of Mt. Etna (Italy). Geophysical Research Letters 32, L02301, doi:10.1029/2004GL021034.

Chakrabarti, R., Basu, A.R., Santo, A.P., Tedesco, D., Vaselli, O., 2009a. Isotopic and geochemical evidence for a heterogeneous mantle plume origin of the Virunga volcanics,Western rift, East African Rift system. Chemical Geology doi:10.1016/j.chemgeo.2008.11.010.

Chakrabarti, R., Sims, K.W.W., Basu, A.R., Reagan, M., Durieux, J., 2009b. Timescales of magmatic processes and eruption ages of the Nyiragongo volcanic from ^{238}U-^{230}Th-^{226}Ra-^{210}Pb disequilibria. Earth and Planetary Science Letters 288, 149-157.

Chavez, P.S., 1996. Image-based atmospheric corrections- revisited and improved. Photogrammetric Engineering and Remote Sensing 62, 1025-1036.

Chorowicz, J., Le Fournier, J., Vidal, G., 1987. A model for rift development in Eastern Africa. Geological Journal 22 (S2), 495-513.

Colclough, S.J., 2005. Investigations of Nyamuragira and Nyiragongo volcanoes (DRC), Using Interferometric Synthetic Aperture Radar, PhD dissertation: University of Cambridge.

Crown, D.A., Baloga, S.M., 1999. Pahoehoe toe dimensions, morphology, and branching relationships at Mauna Ulu, Kilauea Volcano, Hawai'i. Bulletin of Volcanology 61 (5), 288-305, doi:10.1007/s004450050298.

Coombs, M.L., Sisson, T.W., Lipman, P.W., 2006. Growth history of Kilauea inferred from volatile concentrations in submarine-collected basalts. Journal of Volcanology and Geothermal Research 151, 19-49.

Couch, S., Sparks, R.S.J., Carroll, M.R., 2003. The Kinetics of Degassing-Induced Crystallization at Soufriere Hills Volcano, Montserrat. Journal of Petrology 44 (8), 1477-1502.

Danyushevsky, L.V., Della-Pasqua, F.N., Sokolov, S., 2000. Re-equilibration of melt inclusions trapped by magnesian olivine phenocrysts from subduction-related magmas: petrological implications. Contributions to Mineralogy and Petrology 138, 68-83.

Danyushevsky, L., McNeill, A.W., Sobolev, A.V., 2002. Experimental and petrological studies of melt inclusions in phenocrysts from mantle-derived magmas: an overview of techniques, advantages, and complications. Chemical Geology 183, 5-24.

Delmelle, P., Stix, J., Baxter, P., Garcia-Alverez, J., Barquero, J., 2002. Atmospheric dispersion, environmental effects and potential health hazard associated with the low-altitude gas plume of Masaya volcano, Nicaragua. Bulletin of Volcanology 64(6), 423-434.

Demant, A., Lestrade, P., Lubala, R.T., Kampunzu, A.B., Durieux, J., 1994. Volcanological and petrological evolution of Nyiragongo volcano, Virunga volcanic field, Zaire. Bulletin of Volcanology 56(1), 47-61.

Denaeyer, M.E., 1965. Recueil d'analyses des laves du fosse tectonique de l'Afrique centrale (Kivu, Rwanda, Toro - Ankole). Annales/Musee Royal de l'Afrique central, Serie in-8o. Sciences geologiques 49, 234.

Denaeyer, M.E., 1972. Les laves du fosse tectonique de l'Afrique Centrale (Kivu, Rwanda, Toro - Ankole). Annales/Musee Royal de l'Afrique Centrale, Sciences geologiques 72, 134.

Denaeyer, M.E., 1969. Nouvelles donnees lithologiques sur les volcans actifs des Virunga (Afrique Centrale). Bulletin of Volcanology 33 (4), 1128-1144.

Devine, J. D., Sigurdsson, H., Davis, A. N., Self, S., 1984. Estimates of sulfur and chlorine yield to the atmosphere from volcanic eruptions and potential climatic effects. Journal of Geophysical Research 89 (B7), 6309–6325, doi:10.1029/ JB089iB07p06309.

Diner, D.J., Bruegge, C.J., Martonchik, J.V., Ackerman, T.P., Davies, R., Gerstl, S.A.W., Gordon, H.R., Sellers, P.J., Clark, J., Daniels, J.A., Danielson, E.D., Duval, V.G., Klaasen, K.P., Lilienthal, G.W., Nakamoto, D.I., Pagano, R.J., Reilly, T.H., 1989. MISR: A multiangle imaging spectroradiometer for geophysical and climatological research from EOS. Geoscience and Remote Sensing 27(2), 200-214.

Dixon, J.E., Stolper, E.M., Holloway, J.R., 1995. An experimental study of water and carbon dioxide solubilities in mid-ocean ridge basaltic liquids. Part I: Calibration and solubility models. Journal of Petrology 36 (6), 16 07-1631.

Dixon, J.E., Pan, V., 1995. Determination of the molar absorptivity of dissolved carbonate in basanitic glass. American Mineralogist 80, 1339-1342.

Dixon, J.E., 1997. Degassing of alkalic basalts. American Mineralogist 82, 368-378.

Dunbar, N.W., Hervig, R.L., Kyle, P.R., 1989. Determination of pre-eruptive H_2O, F, and Cl contents of silicic magmas using melt inclusions: examples from Taupo volcanic center, New Zealand. Bulletin of Volcanology 51, 177-184.

Ebinger, C., 1989. Tectonic development of the western branch of the East African Rift system. Geological Society of American Bulletin 101, 885-903.

Ebinger, C.J., Sleep, N.H., 1998. Cenozoic magmatism throughout east Africa resulting from impact of a single plume. Nature 395, 788-791.

Ebinger, C., Furman, T., 2002. Geodynamical Setting of the Virunga Volcanic Province, East Africa. Acta Vulcanologica 14 (1-2), 1-8.

Edmonds, M., Gerlach, T.M., 2007. Vapor segregation and loss in basaltic melts. Geology 35, 751-754.

Endreny, T.A., Wood, E.F., Lettenmaier, D.P., 2000. Satellite-derived digital elevation model accuracy: hydogeomorphological analysis requirements. Hydrological Processes 14, 1-20.

Froidevaux, L., Harwood, R.S., Jarnot, R.F., Pickett, H.M., Read, W.G., Siegel, P.H., Cofield, R.E., Filipiak, M.J., Flower, D.A., Holden, J.R., Lau, G.K., Livesey, N.J., Manney, G.L., Pumphrey, H.C., Santee, M.L., Wu, D.L., Cuddy, D.T., Lay, R.R., Loo, M.S., Perun, V.S., Schwartz, M.J., Stek, P.C., Thurstans, R.P., Boyles, M.A., Chandra, K.M., Chavez, M.C., Gun-Shing Chen, Chudasama, B.V., Dodge, R., Fuller, R.A., Girard, M.A., Jiang, J.H., Yibo Jiang, Knosp, B.W., LaBelle, R.C., Lam, J.C., Lee, K.A., Miller, D., Oswald, J.E., Patel, N.C., Pukala, D.M., Quintero, O., Scaff, D.M., Van Snyder, W., Tope, M.C., Wagner, P.A.. Walch, M.J., 2006. The Earth observing system microwave limb sounder (EOS MLS) on the aura Satellite. Geoscience and Remote Sensing 44(5), 1075-1092.

Filella, I., Penuelas, J., 1994, The red edge position and shape as indicators of plant chlorophyll content, biomass, and hydric status. International Journal of Remote Sensing 15, 1459-1470.

Fischer, T.P., Burnard, P., Marty, B., Hilton, D.R., Furi, E., Palhol, F., Sharp, Z.D., Mangasini, F., 2009. Upper-mantle volatile chemistry at Oldoinyo Lengai volcano and the origin of carbonatites. Nature 459, 77-80.

Fujimaki, H., Tatsumoto, M, Aoki, K., 1984. Partition coefficients of Hf, Zr, and REE between phenocrysts and groundmass. Journal of Geophysical Research 89, B662-B672.

Furman, T., 1995. Melting of metasomatized subcontinental lithosphere: undersaturated mafic lava from Rungwe, Tanzania. Contributions of Mineralogy and Petrology 122 (1-2), 97-115.

Furman, T., D., Graham, D., 1999. Erosion of lithospheric mantle beneath the East African Rift system: geochemical evidence from the Kivu volcanic province. Lithos 48, 237-262.

Furman, T., Bryce, J.G., Karson, J., Iotti, A., 2004. East African Rift System (EARS) Plume Structure: Insights from Quaternary Mafic Lavas of Turkana, Kenya. Journal of Petrology 45 (5), 1069-1088.

Furman, T., 2007. Geochemistry of the East African Rift basalts: An overview. Journal of African Earth Sciences 48, 147-160.

Gaetani, G.A., Watson, E.B., 2000. Open system behavior of olivine-hosted melt inclusions. Earth and Planetary Science Letters 183 (1-2), 27-41.

George, R.M., Rogers, N.W., Kelley, S., 1998. Earliest magmatism in Ethiopia: evidence for two mantle plumes in one flood basalt province. Geology 26 (10), 923-926.

George, R.M., Rogers, N.W., 2002. Plume dynamics beneath the African plate inferred from the geochemistry of the Tertiary basalts of southern Ethiopia. Contributions to Mineralogy and Petrology 144, 286-304.

Gerlach, T.M., Graeber, E.J., 1985. Volatile budget of Kilauea volcano. Nature 313, 273-277.

Gerlach, T.M., Westrich, H.R., Symonds, R.B., 1996. Preeruption vapor in magma of the climactic Mount Pinatubo eruption: Source of the giant stratospheric sulfur dioxide cloud. In: Newhall, C.G. and R.S. Punongbayan (Eds.), Fire and Mud: Eruptions and Lahars of Mount Pinatubo, Philippines. University of Washington Press, Seattle, pp. 415-433.

Greenland, P., Rose, W.I., Stokes, J.B., 1985. An estimate of gas emissions and magmatic gas content from Kilauea volcano. Geochimica et Cosmochimica Acta 49 (1), 125-129.

Giggenbach, W.F., 1975. A simple method for the collection and analysis of volcanic gas samples. Bulletin of Volcanology 39 (1), 132-145, DOI: 10.1007/BF02596953.

Gurenko, A.A., Chaussidon, M., Schmincke, H.U., 2001. Magma ascent and contamination beneath one intraplate volcano: Evidence from S and O isotopes in glass inclusions and their host clinopyroxenes from Miocene basaltic hyaloclastites southwest of Gran Canaria (Canary Islands). Geochimica et Cosmochimica Acta 65 (23), 4359-4374.

Halmer, M.M., Schmincke, H.U., Graf, H.F., 2002. The annual volcanic gas input into the atmosphere, in particular into the stratosphere: a global data set for the past 100 years. Journal of Volcanology and Geothermal Research 115, 511-528.

Hamaguchi, H.,1983. Seismological Evidence for Magma Intrusion during the 1981-1982 Nyamuragira Eruption. In: Hamaguchi, H. (Ed.), Volcanoes Nyiragongo and Nyamuragira: Geophysical Aspects. The Faculty of Science, Tohoku University, Sendai, Japan, pp. 35-42.

Hamaguchi, H., Zana, N., 1983. Introduction to Volcanoes Nyiragongo and Nyamuragira. In: Hamaguchi, H. (Ed.), Volcanoes Nyiragongo and Nyamuragira: Geophysical Aspects. The Faculty of Science, Tohoku University, Sendai, Japan, pp. 1-6.

Hansen, J., Ruedy, R., Sato, M., Reynolds, R., 1996. Global surface air temperature in 1995: Return to pre-Pinatubo level. Geophysical Research Letters 23(13), 1665-1668.

Harms, E., Schmincke, H.U., 2000. Volatile composition of the phonolitic Laacher See magma (12,900 yr BP): implications for syn-eruptive degassing of S, F, Cl, and H_2O. Contributions to Mineralogy and Petrology 138, 84-98.

Harris, A.J.L., Flynn, L.P., Keszthelyi, L., Mouginis-Mark, P.J., Rowland, S.K., Resing, J.A., 1998. Calculation of lava effusion rates from Landsat TM data. Bulletin of Volcanology 60(1), 52-71.

Harris, A.J.L., Wright, R., Flynn, L.P., 1999. Remote monitoring of Mount Erebus Volcano, Antarctica, using Polar Orbiters: Progress and Prospects. International Journal of Remote Sensing 20, 3051-3071.

Hauri, E., Wang, J., Dixon, J.E., King, P.L., Mandeville, C., Newman, S., 2002. SIMS analysis of volatiles in silicate glasses 1. Calibration, matrix effects, and comparisons with FTIR. Chemical Geology 183, 99-114.

Hayashi, S., Kasahara, M., Tanaka, K., Hamaguchi, H. N. Zana, N., 1992. Major element chemistry of recent eruptive products from Nyamuragira volcano, Africa (1976-1989). Tectonophysics 209, 273-276.

Head, E.M., 2006. Galapagos Islands volcanic SO_2 emissions, 1979-1998. M.S. Thesis, Michigan Technological University.

Head, E.M., Shaw, A.S., Wallace, P.J., Sims, K.W.W., Carn, S.A., 2011. Insight into volatile behavior at Nyamuragira volcano (D.R. Congo) through olivine-hosted melt inclusions. Geochemistry, Geophysics, and Geosystems, doi:10.1029/2011GC00 3699.

Head, E.M., Maclean, A.L., Carn, S.A., *in press*, Mapping lava flows from Nyamuragira volcano (1967-2011) with satellite data and automated classification. Geomatics, Natural Hazards and Risk, doi:10.1080/19475705.2012.680503

Hensley, S., 2005. An assessment of the SRTM topographic products. Technical Report, JPL D-31639 (Jet Propulsion Laboratory, Pasadena, California).

Hirano, A., Welch, R., Lang, H., 2003. Mapping from ASTER stereo image data: DEM validation and accuracy assessment. ISPRS Journal of Photogrammetry and Remote Sensing 57, 356-370.

Holmes, A., Harwood, H.F., 1937. The petrology of the volcanic field of Bufumbira, south-west Uganda. Memoir/Geological Survey of Uganda 3(2), 300.

Jensen, J.R., 2007. Remote Sensing of the Environment: An Earth Resource Perspective. (2^{nd} ed.), Pearson Prentice Hall, New Jersey, pp. 544.

Johnson, E.R., Wallace, P.J., Cashman, K.V., Granados, H.D., Kent, A.J.R., 2008. Magmatic volatile contents and degassing-induced crystallization at Volcan Jorullo, Mexico: Implications for melt evolution and the plumbing systems of monogenetic volcanoes. Earth and Planetary Science Letters 269 (3-4), 478-487.

Johnson, E.R., Wallace, P.J., Cashman, K.V., Granados, H.D., 2010. Degassing of volatiles (H_2O, CO_2, S, Cl) during ascent, crystallization, and eruption at mafic monogenetic volcanoes in central Mexico. Journal of Volcanology and Geothermal Research, doi:10.1016/j.jvolgeores.2010.02.017.

Kahle, A.B., Abrams, M.J., Abbott, E.A., Mouginis-Mark, P.J., Realmuto, V.J., 1995. Remote Sensing of Mauna Loa. In: Rhodes, J.M. and Lockwood, J.P. (Eds.), Mauna Loa Revealed: Structure, Composition, History, and Hazards. Washington, D.C.: American Geophysical Union, Geophysical Monograph 92, pp. 145-170.

Kampunzu, A.B., Lubala, R.T., Brousse, R., Caron, J.P.H., Cluzel, D., Lenoble, L., Vellutini, P.J., 1984. Sur l'eruption du Nyamulagira de decembre 1981 a janvier 1982: cone et coulee du Rugarambiro (Kivu, Zaire). Bulletin of Volcanology 47 (1), 79-105.

Kampunzu, A.B., Mohr,P., 1991. Magmatic evolution and petrogenesis in the East African Rift System. In: Kampunzu, A.B., Lubala R.T. (Eds.), Magmatism in Extensional Structural Settings, The Phanerozoic African Plate. Springer-Verlag, Heidelberg, pp. 85-136.

Kampunzu, A.B., Bonhomme, M.G., Kanika, M., 1998. Geochronology of volcanic rocks and evolution of the Cenozoic Western Branch of the East African Rift System. Journal of African Earth Science 26 (3), 441-461.

Kasahara, M., 1983. Near-field Tilt Measurements Related to the 1981-1982 Nyamuragira Eruption. In: Hamaguchi, H. (Ed.), Volcanoes Nyiragongo and Nyamuragira: Geophysical Aspects. The Faculty of Science, Tohoku University, Sendai, Japan pp. 47-54.

Kasahara, M., Tanaka, K., Zana, N., 1991. A flank eruption of volcano Nyamuragira in 1991. Journal of African Studies 39, 29-50.

Katabarwa, J.B., 1983. Petrologie du volcan Gahinga (chaine des Virunga, Rwanda). PhD Thesis, Universite de Paris-Sud, Orsay, France.

Katabarwa, J.B., Brousse, R., Lubala, R.T., Thouin, C., 1986. Construction of Kivandimwe (from February to March 1984), two new adventive cones on the north-west flank of Nyamuragira (Birunga volcanic chain, Zaire). Comptes rendus de l'Academie des sciences, Paris Serie I 302, 1249-1252.

Kent, A.J.R., 2008. Melt inclusions in basaltic and associated volcanic rocks. Reviews in Mineralogy and Geochemistry 69, 173-231.

Krotkov, N. A., Carn, S.A., Krueger, A.J., Bhartia, P.K., Yang, K., 2006. Band residual difference algorithm for retrieval of SO_2 from the Aura Ozone Monitoring Instrument (OMI), IEEE Transactions on Geoscience and. Remote Sensing, AURA Special Issue 44 (5), 1259-1266, doi:10.1109/TGRS.2005.861932.

Krueger, A.J., 1983. Sighting of El Chichon Sulfur Dioxide Clouds with the Nimbus 7 Total Ozone Mapping Spectrometer. Science 220 (4604), 1377-1379.

Krueger, A.J., L.S Walter, P.K. Bhartia, C.C Schnetzler, N.A. Krotkov, I. Sprod, G.J.S Bluth, 1995. Volcanic sulfur dioxide measurements from the total ozone mapping spectrometer instruments. Journal of Geophysical Research 100 (D7), 14057-14076.

Lacis, A. A., M. Mishchenko, 1995. Climate forcing, climate sensitivity, and climate response: A radiative forcing modeling perspective on atmospheric aerosols. In: R.J. Charlson and J. Heintzenberg (Eds.), Aerosol Forcing of Climate. John Wiley and Sons, New York, pp. 11–42.

Legeley-Padovani, A., Mering, C., Guillande, R., Huaman, D., 1997. Mapping of lava flows through SPOT images – an example of the Sabancaya volcano (Peru). International Journal of Remote Sensing 18 (15), 3111-3133.

Levelt, P.F., Hilsenrath, E., Leppelmeier, G.W., van den Oord, G.H.J., Bhartia, P.K., Tamminen, J., de Haan, J.F., Veefkind, J.P., 2006. Science objectives of the ozone monitoring instrument. Geoscience and Remote Sensing 44(5), 1199-1208.

Liu, X., Zhang, Z., Peterson, J., Chandra, S., 2007. LiDAR-derived high quality ground control information and DEM for image orthorectification**.** Geoinformatica 11 (1), 37-53.

Livesey, N.J., Read, W.G., Froidevaux, L., Lambert, A., Manney, G.L., Pumphrey, H.C., Santee, M.L., Schwartz, M.J., Wang, S., Cofeld, R.E., Cuddy, D.T., Fuller, R.A., Jarnot, R.F., Jiang, J.H., Knosp, B.W., Stek, P.C., Wagner, P.A., Wu, D.L., 2011. Version 3.3 Level 2 data quality and description document. Technical Report JPL D-33509, Jet Propulsion Laboratory, Pasadena, California.

Lloyd, F.E., Huntingdon, A.T., Davies, G.R., Nixon, P.H., 1991. Phanerozoic volcanism of southwest Uganda: a case for regional K and LILE enrichment of the lithosphere beneath a domed and rifted continental plate. In: Kampunzu, A.B., Lubala R.T. (Eds.) Magmatism in Extensional Structural Settings, The Phanerozoic African Plate. Springer-Verlag, Heidelberg, pp. 85-136.

Lu, Z., Rykhus, R., Masterlark, T., Dean, K.G., 2004. Mapping recent lava flows at Westdahl Volcano, Alaska, using radar and optical satellite imagery. Remote Sensing of the Environment 91, 345-353.

Mackay, M.E., Mouginis-Mark, P.J., 1997. The effect of varying acquisition parameters On the interpretation of SIR-C radar data: The Virunga volcanic chain. Remote Sensing of Environment 59, 321-336.

Mathez, E.A., 1976. Sulfur Solubility and Magmatic Sulfides in Submarine Basalt Glass. Journal of Geophysical Research 81(23), 4269-4276.

Massare, D., Metrich, N., Clocchiatti, R., 2002. High-temperature experiments on silicate melt inclusions in olivine at 1 atm: inference on temperatures of homogenization and H_2O concentrations. Chemical Geology 183, 87-98.

Mavonga, T., Kavotha, S.K., Lukaya, N., Etoy, O., Mifundu, W., Bizimungu, R.K., Durieux, 2010. Some aspect of seismicity prior to the 27 November 2006 eruption of Nyamuragira volcano and its implications for volcano monitoring and risk mitigation in the Virunga area, Western Rift Valley of Africa. Journal of African Earth Sciences 58(5), 829-832.

Mavrogenes, J.A., O'Neill, H.St.C., 1999. The relative effects of pressure, temperature and oxygen fugacity on the solubility of sulfide of sulfide in magic magmas. Geochimica et Cosmochimica. Acta 63 (7/8), 1173-1180.

Metrich, N., Allard, P., Spilliaert, N., Andronico, D., Burton, M., 2004. 2001 flank eruption of the alkali- and volatile-rich primitive basalt responsible for Mount Etna's evolution in the last three decades. Earth and Planetary Science Letters 228, 1-17.

Metrich, N., Clocchiatti, R., 1996. Sulfur abundance and its speciation in oxidized alkaline melts. Geochimica et Cosmochimica. Acta 60 (21), 4151-4160.

Metrich, N., P.J. Wallace, 2008. Volatile Abundances in Basaltic Magmas and Their Degassing Paths Tracked by Melt Inclusions. Reviews in Mineralogy and Geochemistry 69 (1), 363-402, doi:10.2138/rmg.2008.69.10

Michael, P.J., Schilling, J.G., 1989. Chlorine in mid-ocean ridge magmas: Evidence for assimilation of seawater-influenced components. Geochimica et Cosmochimica Acta, 53, 3131-3143.

Mori, T., Notsu, K., Tohjima, Y., Wakita, H., Nuccio, M., Italiano, F., 1995. Remote detection of fumarolic gas chemistry at Volcano, Italy, using an FT-IT spectral radiometer. Earth and Planetary Science Letters 134(1-2), 219-224.

Nelson, D. L., Y. Chen, R. A. Kahn, D. J. Diner, D. Mazzoni, 2008. Example applications of the MISR INteractive eXplorer (MINX) software tool to wildfire smoke plume analyses. Proceedings of SPIE 7089, 708909.1-708909.11.

Newman, S., Lowenstern, J.B., 2002. VolatileCalc: a silicate melt-H_2O-CO_2 solution model written in Visual Basic for Excel. Computational Geosciences 28 (5), 597-604.

Nolet, G., Mueller, S., 1982. A model for the deep structure of the East African rift system from simultaneous inversion of teleseismic data. Tectonophysics 84(2-4), 151-178.

Nyblade, A.W., Robinson, S.W., 1994. The African Superswell. Geophysical Research Letters 21(9), 765-768.

Nyblade, A.W., Owens, T.J., Gurrola, H., Ritsema, J., Langston, C.A., 2000. Seismic evidence for a deep upper mantle thermal anomaly beneath east Africa. Geology 28(7), 599-602.

Nyblade, A.W., Brazier, R.A., 2002. Precambrian lithospheric controls on the development of the East African rift system. Geology 30(8), 755-758.

Oppenheimer, C., Francis, P., Burton, M., Maciejewski, A.J.H., Boardman, L., 1998. Remote measurement of volcanic gases by Fourier transform infrared spectroscopy. Applied Physics B: Lasers and Optics 67(4), 505-515.

Parfitt, E.A., Wilson, L., 1994. The 1983-86 Pu'u'O'o' eruption of Kilauea Volcano, Hawaii: a study of dike geometry and eruption mechanisms for a long-lived eruption. Journal of Volcanology and Geothermal Research 59, 179-205.

Parfitt, E.A., Wilson, L., 1999. A Plinian treatment of fallout from Hawaiian lava fountains. Journal of Volcanology and Geothermal Research 88, 67-75.

Patrick, M.R., Dehn, J., Papp, K.R., Lu, Z., Dean, K., Moxey, L., Izbekov, P., Gurtiz, R., 2003. The 1997 eruption of Okmok Volcano, Alaska: a synthesis of remotely sensed imagery. Journal of Volcanology and Geothermal Research 127, 87-105.

Platz, T., Foley, S.F., Andre, L., 2004. Low-pressure fractionation of the Nyiragongo volcanic rocks, Virunga Province, D.R. Congo. Journal of Volcanology and Geothermal Research 136, 269-295.

Poon, J., Fraser, C.S., 2005. Quality assessment of digital surface models generated from IKONOS imagery. The Photogrammetric Record 20 (110), 162-171.

Portnyagin, M., Almeev, R., Matveev, S., Holtz, F., 2008. Experimental evidence for rapid water exchange between melt inclusions in olivine and host magma. Earth and Planetary Science Letters 272, 541-552.

Pouclet, A., 1975. Activites du volcan Nyamuragira (Rift ouest de l'Afrique Centrale) evaluation des volumes de materiaux emis. Bulletin of Volcanology 39 (3), 466-478.

Pouclet, A., Villeneuve, M., 1972. L'eruption du Rugarama (mars-mai 1971) au volcan Nyamuragira (Rep. Zaire). Bulletin of Volcanology 36, 200-221.

Prata, A.J., Bernardo, C., 2007. Retrieval of volcanic SO_2 column abundance from Atmospheric Infrared Sounder data. Journal of Geophysical Research 112, D20204, doi:10.1029/1006JD007955.

Ray, R.G., 1960. Aerial Photographs in Geologic Interpretation and Mapping. Geological Survey Professional Paper 373, U.S. Government Print Office, Washington, pp. 230.

Robock, A., 1981. A latitudinally dependent volcanic dust veil index, and its effect on climate simulations. Journal of Volcanology and Geothermal Research 11, 67-80.

Rodriguez, E., Morris, C.S., Belz, J.E., Chapin, E.C., Martin, J.M., Daffer, W., Hensley, S., 2005. An assessment of the SRTM topographic products, Technical Report JPL D-31639, Jet Propulsion Laboratory, Pasadena, California.

Rodriguez, K.M., Weissel, J.K., Menke, W.H., 2001. Lava-flow textural trends using SAR: The Virunga Volcanic Chain, East Africa. Institute of Electrical and Electronics Engineers 5, 2421-2423, 10.1109/IGARSS.2001.978022

Roedder, E., 1979. Origin and significance of magmatic inclusions. Bulletin de Mineralogie 102, 487-510.

Roedder, E., 1984. Fluid Inclusions. Mineralogical Society of America, Washington, D.C., pp. 644.

Roeder, P.L., Emslie, R.F., 1970. Olivine-liquid equilibrium. Contributions of Minerology and Petrology 29 (4), 275-289, doi: 10.1007/BF00371276.

Rogers, N.W., James, D., Kelley, S.P., De Mulder, M., 1998. The Generation of Potassic Lavas from the Eastern Virunga Province, Rwanda. Journal of Petrology 29 (6), 1223-1247.

Rogers, N., Macdonald, R., Fitton J.G., George, R., Smith, M., Barreiroe, B., 2000. Two mantle plumes beneath the East African rift system: Sr, Nd and Pb isotope evidence from Kenya Rift basalts. Earth and Planetary Science Letters 176 (387-400).

Roggensack, K., 2001. Unraveling the 1974 eruption of Fuego volcano (Guatemala) with small crystals and their young melt inclusions. Geology 29, 911-914.

Rowe, M.C., Kent, A.J.R., Nielsen, R.L., 2007. Determination of sulfur speciation and oxidation state of olivine hosted melt inclusions. Chemical Geology 236, 303-322.

Rowland, S.K., Harris, A.J.L., Wooster, M.J., Amelung, F., Garbeil, H., Wilson, L., Mouginis-Mark, P.J., 2003. Volumetric characteristics of lava flows from interferometric radar and multispectral satellite data: the 1995 Fernandina and 1998 Cerro Azul eruptions in the western Galapagos. Bulletin of Volcanology 65, 311-330.

le Roux, P.J., Shirey, S.B., Hauri, E.H., Perfit, M.R., Bender, J.F., 2006. The effects of variable source, processes and contaminants on the composition of northern EPR MORB (8-10˚N and 12-14˚N): Evidence from volatiles (H_2O, CO_2, S) and halogens (F, Cl). Earth and Planetary Science Letters 251, 209-231.

Saal, A.E., Hauri, E.H., Langmuir, C.H., Perfit, M.R., 2002. Vapour undersaturation in primitive mid-ocean-ridge basalt and the volatile content of Earth's upper mantle. Nature 419, 451-455.

Sawyer, G.M., Carn, S.A., Tsanev, V.I., Oppenheimer, C., Burton, M., 2008. Investigation into magma degassing at Nyiragongo volcano, Democratic Republic of the Congo. Geochemistry, Geophysics, and Geosystems 9 (2), doi:10.1029/2007 GC001829.

Schmincke, H.U., Park, C., Harms, E., 1999. Evolution and environmental impacts of the eruption of Laacher See Volcano (Germany) 12,900 a BP. Quaternary International 61, 61-72.

Seager, S., Turner, E.L., Schafer, J., Ford, E.B., 2005. Vegetation's red edge: a possible spectroscopic biosignature of extraterrestrial plants. Astrobiology 5, 372-390.

Self, S., Rampino, M.R., Newton, M.S., Wolff, J.A., 1984. Volcanological study of the great Tambora eruption of 1815. Geology 12 (11), 659-663.

Self, S,, Thordarson, T., Keszthelyi, L., 1997. Emplacement of continental flood basalt lava flows. In: Mahoney, J.J., Coffin M.F. (Eds.), Large Igneous Provinces: Continental, Oceanic, and Planetary Flood Volcanism. American Geophysical Union, Washington D.C., Geophysical Monograph 100, pp. 381-410.

Sharma, K., Blake, S., Self, S., 2004. SO_2 emissions from basaltic eruptions, and the excess sulfur issue. Geophysical Research Letters, doi:10.1029/2004GL019688.

Shaw, H.R. Swanson D.A., 1970. Eruption and flow rates of flood basalts. In: Gilmour E.H., Stradling D. (Eds.) Proceedings, Second Columbia River Basalt Symposium. Eastern Washington State College Press, Cheney, pp. 271-299.

Shaw, A.M., Hauri, E.H., Fischer, T.P., Hilton, D.R., Kelley, K.A., 2008. Hydrogen isotopes in Mariana arc melt inclusions: Implications for subduction dehydration and the deep-Earth water cycle. Earth and Planetary Science Letters 275, 138-145.

Shaw, A.M., Behn, M.D., Humphris, S.E., Sohn, R.A., Gregg, P.M., 2010. Deep pooling of low degree melts and volatile fluxes at the 85°E segment of the Gakkel Ridge: Evidence from olivine-hosted melt inclusions and glasses. Earth and Planetary Science Letters 298, 311-322.

Shinohara, H., 2008. Excess degassing from volcanoes and its role on eruptive and intrusive activity. Reviews of Geophysics, doi:10.1029/2007RG000244.

Sisson, T.W., Layne, G.D., 1993. H_2O in basalt and basaltic andesite glass inclusions from four subduction-related volcanoes. Earth and Planetary Science Letters 117 (3-4), 619-635.

Smets, B., Wauthier, C., d'Oreye, N., 2001. A new map of the lava flow field of Nyamuragira (D.R. Congo) from satellite imagery. Journal of African Earth Sciences 58, 778-786.

Smithsonian Institution, 1971-2010. Nyamuragira, Center for Short-Lived Phenomena, Event Notification Report v. 31, no. 71 – Bulletin of the Global Volcanism Network v. 35, no. 8.

Smithsonian Institution, 1971-2011. Nyamuragira, Scientific Event Alert Network (SEAN) Bulletin v. 7, no. 1– Bulletin of the Global Volcanism Network v. 37, no. 03.

Smithsonian Institution, 1982. Nyamuragira, Scientific Event Alert Network (SEAN) Bulletin v. 7, no. 1.

Smithsonian Institution, 2006. Nyamuragira, Bulletin of the Global Volcanism Network v. 32, nos. 1-3.

Smithsonian Institution, 2010. Nyamuragira, Bulletin of the Global Volcanism Network v. 35, no. 8.

Sobolev, A.V., Clocchiatti, R., Dhamelincourt, P., 1983. Les variations de temperature, de la composition du magma et l'estimation de la pression partielle d'eau pendant la cristallisation de l'olivine dans les oceanites du Piton de la Fournaise (Reunion, eruption de 1966). Comptes Rendus de l'Academie des Sciences (Paris) 296, 275-280.

Spandler, C., O'Neill, H.St.C., Kamenetsky, V.S., 2007. Survival times of anomalous melt inclusions from element diffusion in olivine and chromite. Nature 447, 303-306.

Sparks, R.S.J., 1997. Causes and consequences of pressurization in lava dome eruptions. Earth and Planetary Science Letters 150, 177-189.

Spath, A., Le Roex, A.P., Opiyo-Akech, N., 2001. Plume-Lithosphere Interaction and the Origin of Continental Rift-related Alkaline Volcanism- the Chyulu Hills Volcanic Province, Southern Kenya. Journal of Petrology 42 *(*4), 765-787.

Spera, F.J., Bergman, S.C., 1980. Carbon Dioxide in Igneous Petrogenesis: I. Contributions to Mineralogy and Petrology 74, 55-66.

Spilliaert, N., Allard, P., Metrich, N., Sobolev, A.V., 2006. Melt inclusion record of the conditions of ascent, degassing, and extrusion of volatile-rich alkali basalt during the powerful 2002 flank eruption of Mount Etna (Italy). Journal of Geophysical Research 111 (B04203), doi:10.1029/2005JB003934.

Spinetti, C., Mazzarini, F., Casacchia, R., Colini, L., Neri, M., Behncke, B., Salvatori, R., Buongiorno, M.F., Pareschi, M.T., 2009. Spectral properties of volcanic materials from hyperspectral field and satellite data compared with LiDAR data at Mt. Etna. International Journal of Applied Earth Observation and Geoinformation 11, 142-155.

Spiro, P. A., Jacob, D. J., Logan, J. A., 1992. Global inventory of sulfur emissions with 1º ´ 1º resolution. Journal of Geophysical Research 97, 6023–6036.

Stothers, R.B., Wolff, J.A., Self, S., Rampino, M.R., 1986. Basaltic fissure eruptions, plume heights, and atmospheric aerosols. Geophysical Research Letters 13(8), 725-728.

Suh, C.E., Luhr, J.F., Njome, M.S., 2008. Olivine-hosted glass inclusions from Scoriae erupted in 1954-2000 at Mount Cameroon volcano, West Africa. Journal of Volcanology and Geothermal Research 169, 1-33.

Sutton, A.J., Elias, T., Gerlach, T.M., Stokes, J.B., 2001. Implications for eruptive processes as indicated by sulfur dioxide emissions from Kilauea Volcano, Hawaii, 1979-1997. Journal of Volcanology and Geothermal Research 108, 283-302.

Swanson, D.A., Duffield, W.A., Jackson, D.B., Peterson, D.W., 1979. Chronological narrative of the 1969-1971 Mauna Ulu eruption of Kilauea volcano, Hawaii. U.S. Geological Survey Professional Paper 1056, 1-55.

Tedesco, D., Vaselli, O., Papale, P., Carn, S.A., Voltaggio, M., Sawyer, G.M., Durieux,J., Kasereka, M., Tassi, F., 2007. January 2002 volcano-tectonic eruption of Nyiragongo volcano, Democratic Republic of Congo. Journal of Geophysical Research 112, B09202, doi:10.1029/2006JB004762.

Thonnard, R.LG., Denayer, M.E., Antun, P., 1965. Carte Volcanologique des Virunga (1/50000), Afrique Centrale, Feuille No. 1. Centre National de Volcanologie, Belgium.

Thordarson, T., Self, S., Miller, D. J., Larsen, G., Vilmundardóttir, E. G., 2003. Sulphur release from flood lava eruptions in the Veidivötn, Grímsvötn and Katla volcanic systems, Iceland. Geological Society, London, Special Publications 213, 103-121, doi: 10.1144/GSL.SP.2003.213.01.07

Trusdell, F.A., 1995. Lava Flow Hazards and Risk Assessment on Mauna Loa Volcano, Hawaii. In: Rhodes, J.M. and Lockwood, J.P. (Eds.), Mauna Loa Revealed: Structure, Composition, History, and Hazards. American Geophysical Union, Geophysical Monograph 92, Washington, D.C., pp. 315-336.

Ueki, S., 1983. Recent volcanism of Nyamuragira and Nyiragongo. In: Hamaguchi, H. (Ed.), Volcanoes Nyiragongo and Nyamuragira: Geophysical Aspects. The Faculty of Science, Tohoku University, Sendai, Japan, pp. 7-18.

Verhoogen, J., 1939. New data on volcanic gases: the 1938 eruption of Nyamlagira. American Journal of Science 237, 656-672.

Vergniolle, S., Jaupart, C., 1990. Dynamics of Degassing at Kilauea Volcano, Hawaii. Journal of Geophysical Research 95 (B3), 2793-2809.

Vigouroux, N., Wallace, P.J., Kent, A.J.R., 2008. Volatiles in High-K Magmas from the Western Trans-Mexican Volcanic Belt: Evidence for Fluid Fluxing and Extreme Enrichment of the Mantle Wedge by Subduction Processes. Journal of Petrology 49 (9), 1589-1618, doi:10.1093/petrology/egn039.

Vollmer, R., Norry, M.J., 1983. Possible origin of K-rich volcanic rocks from Virunga, East Africa, by metasomatism of continental crustal material: Pb, Nd and Sr isotopic evidence. Earth and Planetary Science Letters 64(3), 374-386.

Wadge, G., 1980. Output rate of magma from active central volcanoes. Nature 288, 253-255.

Wadge, G., 1981. The variation of magma discharge during basaltic eruptions. Journal of Volcanology and Geothermal Research 11, 139-168.

Wallace, P., Carmichael, S.E., 1992. Sulfur in basaltic magmas. Geochimica et Cosmochimica Acta 56, 1863-1974.

Wallace, P.J., Gerlach, T.M., 1994. Magmatic Vapor Source for Sulfur Dioxide Released During Volcanic Eruptions: Evidence from Mount Pinatubo. Science 265 (5171), 497-499.

Wallace, P., Anderson, A.T., 1998. Effects of eruption and lava drainback on the H_2O contents of basaltic magmas at Kilauea Volcano. Bulletin of Volcanology 59 (5), 327-344.

Wallace, P.J., Anderson, A.T., Davis, A.M., 1999. Gradients in H_2O, CO_2 and exsolved gas in a large-volume silicic magma system: interpreting the record preserved in melt inclusions from the Bishop Tuff. Journal of Geophysical Research 104, 20097-20122.

Wallace, P.J., 2001. Volcanic SO_2 emissions and the abundance and distribution of exsolved gas in magma bodies. Journal of Volcanology and Geothermal Research 108, 85-106.

Wallace, P.J., 2005. Volatiles in subduction zone magmas: concentrations and fluxes based on melt inclusion and volcanic gas data. Journal of Volcanology and Geothermal Research 140, 217-240.

Watchorn, F., Nichold, G., Bosence, D., 1998.Tift-related sedimentation and stratigraphy, southern Yemen (Gulf of Aden). In: B. Purser, D. Bosence (Eds.), Sedimentation and Tectonics of Rift Basins, Chapman and Hall, London, pp.165–189.

Waters, C.L., Bryce, J.G., Furman, T., 2004. Magmatic Processes Beneath the East African Rift System (EARS): Insights From Melt Inclusions in Lavas of Turkana, Kenya, poster presented at Spring Meeting, AGU, Abstract V43B-05, Montreal, Canada.

Weeraratne, D.S., Forsyth, D.W., Fisher, K.M., Nyblade, A.A., 2003.Evidence for an upper mantle plume beneath the Tanzanian Craton from Rayleigh wave tomography Journal of Geophysical Research 108, doi.org/10.1029/2002JB00227.

Wiart, P.A.M., Oppenheimer, C., Francis, P., 2000. Eruptive history of Dubbi volcano, northeast Afar (Eritrea), revealed by optical and SAR image interpretation. International Journal of Remote Sensing 21, 911-936.

Wilson, L., 1980. Relationships between pressure, volatile content and eject velocity. Journal of Volcanology and Geothermal Research 8, 287-313.

Wilson, L., Head, J.W., 1981. Ascent and Eruption of Basaltic Magma on the Earth and Moon. Journal of Geophysical Research 86 (B4), 2971-3001.

Winker, D.M., Pelon, J.R., McCormick, M.P., 2003. The CALIPSO mission: spaceborne lidar for observation of aerosols and clouds. Proceedings of SPIE, 4893, doi.org/10.1117/12.466539.

Witter, J.B., Kress, V.C., Newhall, C.G., 2005. Volcan Popocatepetl, Mexico. Petrology, Magma Mixing, and Immediate Sources of Volatiles for the 1994-Present Eruption. Journal of Petrology 46 (11), 2337-2366.

Wolfenden, E., Ebinger, C., Yirgu, G., Deino, A., Ayalew, D., 2004.Evolution of the northern Main Ethiopian rift: Birth of a triple junction. Earth and Planetary Science Letters 224, 213–228.

Wright, R., Pilger, E., 2008. Radiant flux from Earth's subaerially erupting volcanoes. International Journal of Remote Sensing 29(22), 6443-6466.

Yang, K., Krotkov, N. A., Krueger, A. J., Carn, S. A., Bhartia, P. K., Levelt, P. F., 2007. Retrieval of large volcanic SO_2 columns from the Aura Ozone Monitoring Instrument: Comparison and limitations. Journal of Geophysical Research, doi:10.1029/2007JD008825.

Yang, K., Krotkov, N.A., Krueger, A.J., Carn, S.A., Bhartia, P.K., Levelt, P.F., 2009. Improving retrieval of volcanic sulfur dioxide from backscattered UV satellite observations. Geophysical Research Letters 36, L03102, doi:10.1029/2008 GL036036.

Yang, K., Liu, X., Krotkov, N.A., Krueger, A.J., and Carn, S.A., 2010a. Estimating the Altitude of Volcanic Sulfur Dioxide Plumes from Space Borne Hyper-spectral UV Measurements . Geophysical Research Letters 36, L10803, doi:10.1029/2009 GL038025.

Yang, K., Liu, X., Bhartia, P.K., Krotkov, N.A., Carn, S.A., Hughes, E., Krueger, A.J., Spurr, R., Trahan, S., 2010b. Direct Retrieval of Sulfur Dioxide Amount and Altitude from Spaceborne Hyper-spectral UV Measurements: Theory and Application. Journal of Geophysical Research, Okmok-Kasatochi Special Issue 115, D00L09, doi:10.1029/ 2010JD013982.

Zana, N., 1983. Seismological Study of the 1980 Nyamuragira Eruption. In: Hamaguchi, H. (Ed.), Volcanoes Nyiragongo and Nyamuragira: Geophysical Aspects. The Faculty of Science, Tohoku University, Sendai, Japan, pp. 29-33.

Zebker, H. A. , Rosen, P. A. , Goldstein, R. M., Gabriel, A., Werner, C. L., 1994. On the derivation of coseismic displacement fields using differential radar interferometry: The Landers earthquake. Journal of Geophysical Research 99 (B10), 19,617-19,634.

CHAPTER 7: APPENDICES

Appendices are located on the included CD. The following is a list detailing the Appendices by chapter.

Chapter 2

Appendix A. Factor loadings for Landsat images used to map Nyamuragira lava flows (1967-2004). Those factor loadings displaying <6 PCs indicates either low spectral resolution scenes (e.g., 1974) or corrupted bands (e.g., 2003). The dark black outlines indicate the PCs chosen for unsupervised classification and the dark shaded cells represent the bands from the original imagery that contributed most to each PC. The PC combination used to map the individual flows are listed next to the flow year; those lightly shaded cells represent a deviation from PC 1-3.

Appendix B. This flowchart describes, step-by-step, the processing routine we used to map Nyamuragira lava flows. We used ERDAS Imagine image processing software and ESRI ArcGIS software in our study, but these instructions can be translated to other image processing and mapping programs.

Chapter 3

Appendix C. Nyamuragira whole rock major and trace elements.

Appendix D. Melt inclusion corrected major element and volatile compositions**.**

Appendix E. Uncorrected Melt Inclusion Major Elements and Volatiles

Chapter 4

Appendix F. Through estimating Nyamuragira volcanic cloud heights with HYSPLIT, MLS, and MISR, we were able to calculate more accurate SO_2 column amounts.